Measurement and Analysis of Intracardiac Blood Flow and Vortex Ring Formation

Töger, Johannes

2014

– CENTRUM SCIENTIARUM MATHEMATICARUM –

Measurement and analysis of intracardiac blood flow and vortex ring formation

JOHANNES TÖGER

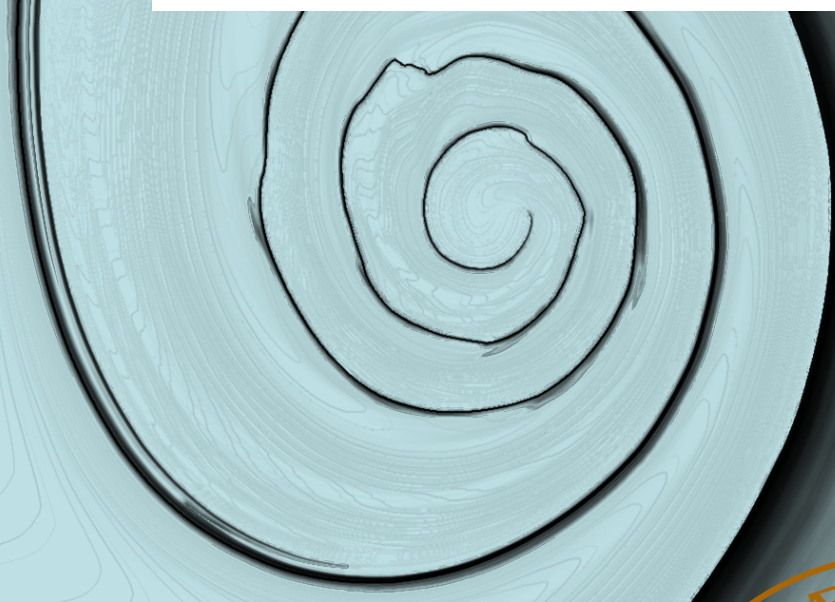

Lund University
Faculty of Engineering
Centre for Mathematical Sciences
Numerical Analysis

MEASUREMENT AND ANALYSIS OF INTRACARDIAC BLOOD FLOW AND VORTEX RING FORMATION

JOHANNES TÖGER

LUND UNIVERSITY

Faculty of Engineering
Centre for Mathematical Sciences
Numerical Analysis

Numerical Analysis
Centre for Mathematical Sciences
Lund University
Box 118
SE-221 00 Lund
Sweden

http://www.maths.lth.se/

Doctoral Theses in Mathematical Sciences 2014:5
ISSN 1404-0034

ISBN 978-91-7623-072-5 (print), 978-91-7623-073-2 (pdf)
LUTFNA-1007-2014

johannes.toger@gmail.com

Printed in Sweden by Media-Tryck, Lund University, Lund 2014

You never count your money
when you are sitting at the table
there will be time enough for counting
when the dealing is done

Kenny Rogers – The Gambler
1978

योगस्थः कुरु कर्माणि सङ्गं त्यक्त्वा धनंजय |
सिद्ध्यसिद्ध्योः समो भूत्वा समत्वं योग उच्यते

yogasthaḥ kuru karmāṇi
saṅgaṃ tyaktvā dhanaṃjaya
siddhi-asiddhyoḥ samo bhūtvā
samatvaṃ yoga ucyate

Perform your actions firm in yoga,
abandoning attachment, O Dhanamjaya,
with indifference to success or failure!
This state of equanimity is called Yoga.

Bhagavad Gita, chapter 2, verse 48
2nd century BCE

Contents

List of papers . . . iii
Author's contributions . . . iv
Abstract . . . v
Populärvetenskaplig sammanfattning – Summary in Swedish . . . vii
Abbreviations and symbols . . . ix

1 Background **1**
1.1 The human heart . . . 1
1.2 Magnetic resonance imaging . . . 7
1.3 Laser methods for measurement and visualization of flow . . . 10
1.4 Flow visualization . . . 13
1.5 Vortex ring formation . . . 15

2 Aims **21**

3 Methods **23**
3.1 Magnetic resonance imaging . . . 23
3.2 Study population and imaging protocols . . . 24
3.3 Vortex ring flow phantom . . . 25
3.4 Data analysis . . . 30

4 Computational methods **37**
4.1 Coordinate systems . . . 37
4.2 Velocity interpolation . . . 40
4.3 Particle tracing . . . 40
4.4 Lagrangian Coherent Structures . . . 41
4.5 Volume Tracking . . . 43

5 Results and Discussion **47**
5.1 Accuracy and validation . . . 47
5.2 In vivo vortex ring formation . . . 60

5.3 Visualization 66
5.4 Future work 73

6 Conclusions **75**

Bibliography 77

Acknowledgments **87**
Funding 88

Papers I-V

List of papers

This thesis is based on the research presented in the following papers. My contribution to each is described on the following page.

I. Carlsson M, *Töger J*, Kanski M, Markenroth Bloch K, Ståhlberg F, Heiberg E, Arheden H: **Quantification and visualization of cardiovascular 4D velocity mapping accelerated with parallel imaging or k-t BLAST: head to head comparison and validation at 1.5 T and 3 T.** *Journal of Cardiovascular Magnetic Resonance 2011,* ***13****:55*

II. *Töger J*, Bidhult S, Revstedt J, Carlsson M, Arheden H, Heiberg E: **Independent validation of 4D flow magnetic resonance flow velocities and vortex ring parameters against particle imaging velocimetry and planar laser-induced flourescence.** *Manuscript.*

III. *Töger J*, Carlsson M, Söderlind G, Arheden H, Heiberg E: **Volume Tracking: A new method for quantitative assessment and visualization of intracardiac blood flow from three-dimensional, time-resolved, three-component magnetic resonance velocity mapping.** *BMC Medical Imaging* 2011, **11**:10.

IV. *Töger J*, Kanski M, Carlsson M, Kovács SJ, Söderlind G, Arheden H, Heiberg E: **Vortex ring formation in the left ventricle of the heart: Analysis by 4D flow MRI and Lagrangian Coherent Structures.** *Annals of Biomedical Engineering* 2012, 40(12):2652-62.

V. *Töger J*, Kanski M, Kovács SJ, Borgquist R, Carlsson M, Söderlind G, Arheden H, Heiberg E: **Diastolic vortex ring mixing of atrial and ventricular blood: comparison of healthy and failing hearts.** *Manuscript.*

Author's contributions

This section describes my contributions to each of the papers.

I. I participated in data collection, developed major parts of the software for data post-processing and analysis, performed all technical aspects of the particle tracing analysis, and wrote a minor part of the manuscript.

II. I designed the study, led design of the flow phantom and pump, performed all experiments with help from the other authors, performed data analysis, drafted the manuscript and integrated feedback from other authors.

III. I developed the details of the method and implemented it in software, drafted the manuscript, analyzed data and integrated feedback from the other authors. Furthermore, I participated in the data collection.

IV. I helped conceive of and design the study, developed software for analysis of Lagrangian Coherent Structures in Magnetic Resonance flow data, performed computations and data analysis, drafted the manuscript and integrated feedback from the other authors.

V. I conceived of and designed the study, developed software for data analysis, performed data analysis, drafted the manuscript and merged feedback from the other authors.

Abstract

Increased understanding of the pumping mechanics of the heart are of great importance to develop diagnostics, treatment and prognostics for cardiovascular diseases. Blood flow in the heart is connected to its anatomy and function, and may therefore be a sensitive marker of cardiac health and disease.

Therefore, the aim of this thesis is to develop and validate methods for quantification and visualization of intracardiac blood flow measurements using 4D phase contrast magnetic resonance velocity mapping (4D PC-MR). The thesis, which is based on five papers, aims to 1) validate *measurement accuracy*, 2) investigate *vortex ring formation* in the left ventricle (LV), and 3) evaluate and improve *visualization* of flow.

For aim 1), 4D PC-MR stroke volume (SV) measurements in the aorta and main pulmonary artery were validated against 2D PC-MR at 1.5T and 3T, using two different 4D PC-MR sequences, one accelerated using SENSE and the other using k-t BLAST (Paper I). SENSE measurements showed good accuracy and measurements at 3T compared favorably to 1.5T. The k-t BLAST measurements showed a too high bias to be used for SV quantification.

Furthermore, a phantom setup for validation of 4D PC-MR against independent measurements by particle imaging velocimetry (PIV) and planar laser-induced floures-cence (PLIF) was developed and constructed (Paper II). The developed flow phantom showed excellent stability ($R^2 = 0.96$, bias -0.06 ± 0.70 cm/s), making it suitable for validation of 4D PC-MR measurements. Validation of 4D PC-MR velocities against PIV show good agreement for mean velocities, but 4D PC-MR underestimates peak velocities by 8-25%. Vortex ring volume (VV) measurements with 4D PC-MR showed good agreement with PLIF. However, vortex ring mixing ratio (MXR) showed poor agreement. Due to possible differences between the phantom setup and in vivo vortex ring formation, further studies are needed to determine if MXR can be measured under in vivo flow conditions.

For aim 2), a new method for quantification of vortex ring formation in the left ventricle using Lagrangian Coherent Structures was developed and implemented in software (Paper IV). Vortex ring volume was quantified in 15 healthy volunteers and 15 patients with heart failure. The vortex ring occupied $51 \pm 7\%$ of the LV blood volume in healthy volunteers, but only $26 \pm 5\%$ in the patients ($p < 0.001$). This suggests that a larger

volume of blood is static in the LV of the patients, with an associated increase in the risk of thrombus formation (Papers IV and V).

The vortex ring mixing ratio (MXR), defined as the amount of blood pulled into the vortex ring due to its rotation divided by the total volume of the vortex ring, was also quantified in healthy volunteers and heart failure patients (Paper V). MXR was higher in the patients compared to the volunteers ($33 \pm 7\%$ vs $19 \pm 7\%$, $p < 0.001$).

For aim 3), a new method for visualization of 4D PC-MR blood flow measurements was developed and implemented in software. The new method, called Volume Tracking (Paper III), allows visualization of the motion of a blood volume through the heart. Volume Tracking gives incremental information about the blood flow compared to earlier used methods, e.g. by revealing a complex blood flow pattern in the right ventricle (RV) when compared to the LV.

Additionally, the quality of particle tracing visualizations in 4D PC-MR accelerated using SENSE or k-t BLAST was evaluated (Paper I). No difference could be measured, showing that the higher acceleration, and therefore shorter scan duration, in k-t BLAST measurements can be used when the main goal is to visualize, and not quantify, blood flow.

Populärvetenskaplig sammanfattning

Ökad förståelse för hjärtats pumpfunktion är av stort intresse för att kunna förbättra diagnostik, behandling och prognoser för hjärtsjuka patienter. Blodflöde i hjärtat är direkt kopplat till hjärtats form och rörelse och kan därför vara en viktig markör för hjärtats funktion. Därför var målet med denna avhandling att utveckla och förbättra mätningar av blodflöde med hjälp av magnetisk resonanstomografi (MR, eller magnetkamera) i hjärtat.

Speciellt behandlas tredimensionella, tidsupplösta flödesmätningar, även kallat 4D-flöde. Avhandlingen behandlar tre områden: mätningarnas *noggrannhet*, *virvelbildning* och *visualisering*.

Mätningarnas noggrannhet jämfördes med så kallat 2D-flöde, som ger en mer begränsad, men exaktare mätning. Resultaten visar att starkare magnetfält ger bättre flödesmätningar än ett svagare magnetfält. En snabbare variant på 4D-flödessekvensen ger inte tillräckligt bra mätningar för kliniskt utvärdering av hjärtats funktion, medan en något längre bildinsamling ger fullgod kvalitet. Dessutom utvecklades en ny uppställning för att validera 4D-flödesmätningar jämfört med mer exakta lasermetoder. Med hjälp av den nya uppställningen visas att 4D-flöde visar rätt hastighet i medel, men att topphastigheter underskattas med 8-25%. Vidare visades att 4D-flöde kan mäta volymen på virvlar i blodflödet, men att det fortfarande är svårt att mäta hur blodet blandar sig i virveln.

En ny metod för att mäta virvelbildning under hjärtats fyllnadsfas, kallad Lagrangian Coherent Structures, utvecklades. Mätningar av virvelbildning under hjärtats fyllnadsfas utfördes i friska frivilliga och patienter med hjärtsvikt. I friska personer fyllde virveln ut c:a 50% av blodvolymen, men bara 20% hos patienterna. Detta kan betyda att blodet blandar sig mindre effektivt hos patienterna, vilket kan leda till en ökad risk för blodproppar.

Slutligen undersöktes visualisering av blodflöde, det vill säga hur flödesmätningarna kan presenteras i bildform för tolkning av läkare och forskare. En ny metod, Volume Tracking, utvecklades för att följa hur blodvolymer rör sig genom hjärtat. Dessutom jämfördes visualiseringar med tidigare standardmetoder mellan två olika snabba

4D-flödessekvenser. Ingen skillnad i kvaliteten på visualiseringarna kunde mätas, vilket betyder att den snabbare sekvensen kan användas om målet med undersökningen enbart är att visualisera flödet och därmed ge en kortare undersökning för patienten.

Abbreviations

2ch, 3ch, 4ch	2-chamber, 3-chamber and 4-chamber CMR view of the heart
2D PC-MR	Through-plane 2D phase contrast magnetic resonance velocity mapping.
4D PC-MR	Three-dimensional, time-resolved, three-directional phase contrast magnetic resonance velocity mapping. 4D = 3D + time.
AV plane	Atrioventricular plane
CMR	Cardiovascular magnetic resonance
DCM	Dilated cardiomyopathy
DV	Diastatic volume (volume of LV at diastasis, Figure 1.3, page 6)
ECG	Electrocardiogram
EDV	End-diastolic volume (Figure 1.3, page 6)
EF	Ejection fraction – EF = SV/EDV
ESV	End-systolic volume (Figure 1.3, page 6)
EWV	E-wave volume (early rapid filling, Figure 1.3, page 6)
FTLE	Finite-time Lyapunov Exponent $\sigma^{t}_{t_0}(\mathbf{x})$
LA	Left atrium (Figure 1.1, page 3)
LCS	Lagrangian Coherent Structures
LPS	The patient-oriented coordinate system (Figure 4.1, page 39)
LV	Left ventricle (Figure 1.1, page 3)
MR	Magnetic resonance, used as synonym for MRI
MRI	Magnetic resonance imaging
MXR	Vortex ring mixing ratio
PIV	Particle imaging velocimetry (Section 1.3.1, page 10)
PLIF	Planar laser-induced flourescence (Section 1.3.2, page 11)
RA	Right atrium (Figure 1.1, page 3)
RV	Right ventricle (Figure 1.1, page 3)
SV	Stroke volume (1.3, page 6)
THV	Total heart volume
TE	Echo time (MRI)
TR	Repetition time (MRI)
VENC	Velocity encoding parameter (phase contrast MRI)
VFR	Vortex formation ratio – vortex formation time (VFT) or stroke ratio (L/D)
VV	Vortex-ring volume

Symbols and notation

Scalars are typeset in italics (t, σ, ...) and vectors in regular bold characters ($\mathbf{L}$, $\mathbf{x}$, $\mathbf{n}$, ...). The vector-valued flow map ϕ and the auxiliary function ψ are the exceptions, to better follow notation in previous publications.

$\mathbf{L}$	The unit vector from the patients' right to left
$\mathbf{P}$	The unit vector from the patients' front to back (posterior)
$\mathbf{S}$	The unit vector from the patients' feet to head (superior)
$\mathbf{x}$	Position in LPS coordinates, $\mathbf{x} = (x_1, x_2, x_3)$
$\mathbf{y}$	Position in image-based coordinates, $\mathbf{y} = (y_1, y_2, y_3)$
$\mathbf{I}$	Position expressed as pixel indices, $\mathbf{I} = (i, j, k)$
n	Timeframe index
t	Physical time, counted from the start of the ECG R-wave
$\mathbf{v}(\mathbf{x}, t)$	Fluid velocity in LPS coordinates, relative to the (stationary) subject
$\phi_{t_0}^{t}(\mathbf{x})$	The flow map, mapping a particle's position at time t_0 to its position at time t
$\sigma_{t_0}^{t}(\mathbf{x})$	Finite-time Lyapunov Exponent (FTLE)
$\psi(\mathbf{x}, t)$	Auxiliary function in Volume Tracking, $\psi(\mathbf{x}, t) = \phi_{t}^{t_0}(\mathbf{x})$
∇	Spatial gradient
∂_t	Time derivative

Chapter 1

Background

The function of the human heart is to transport a sufficient amount of blood to sustain the body's metabolism. Exercise increases the body's metabolic requirements, which leads to a rapid, up to fivefold increase in cardiac output. Furthermore, the heart must function continuously over an individual's lifetime. The inability of the heart to deliver the required amount of blood at normal filling pressures is called heart failure, and is a major cause of death, reduced quality of life and healthcare costs. [1–3]

The flow of blood through the heart is closely linked to the anatomy and function of the muscle and valves of the heart, and changes in the heart influence the flow patterns. [4–8] Although the flow of blood through the heart is a central aspect of cardiac pumping, it is not yet completely understood. Therefore, detailed measurement and analysis of blood flow in the heart has the potential to increase our understanding of cardiac pumping in health and disease. [9]

1.1 The human heart

Figure 1.1 shows a schematic drawing of the human heart. The heart can be divided into a left and a right side, each with an atrium and a ventricle, making for a total of four chambers: left atrium (LA), left ventricle (LV), right atrium (RA) and right ventricle (LV). The lowest part of the heart, pointing forwards and to the left in the body, is called the apex. The opposite side of the heart, pointing towards the head, is called the base.

On the left side, the LA and LV are separated by the mitral valve. The aortic valve separates the LV from the aorta. The right side of the heart is constructed in a similar manner, with the tricuspid valve separating the RA and RV, and the pulmonary valve separating the RA from the pulmonary artery. The valves are one-way to ensure an effective blood flow. All valves are situated in the atrio-ventricular plane (AV plane), a fibrous structure separating the atria from the ventricles. Due to the higher resistance in

the systemic circulation compared to the pulmonary circulation, the LV must generate a higher pressure than the RV. Therefore, the heart muscle, or myocardium, is thicker in the LV compared to the RV.

Venous blood, low on oxygen and a high on carbon dioxide after passing through the body, flows through the superior and inferior vena cava into the RA, and then into the RV through the tricuspid valve. The RV then pumps the blood through the pulmonary artery into the lungs, where the red blood cells are oxygenated and excess carbon dioxide is ventilated into the atmosphere. The blood then returns to the LA through the pulmonary veins. Finally, the blood flows into the LV and is then pumped into the aorta to supply the body with oxygenated blood.

1.1.1 Cardiac pumping

At rest, the frequency of the heart is approximately 70 beats per minute (bpm), ejecting 70 ml per beat, i.e. 5 liters per minute. The motion of the heart can be divided into two phases based on the activity of the ventricles. The contraction or ejection phase is called *systole* and the relaxing or filling phase is called *diastole*, as illustrated in Figure 1.2.[10,11] Note that the cardiac cycle is completed with a near-constant total heart volume, with reciprocal filling and emptying between atria and ventricles.[12–15] Systole and diastole are separated by short periods of time, called the isovolumic relaxation period and isovolumic contraction period, where all valves are closed and the volumes of ventricles are constant.[10,11]

The top panel of Figure 1.3 shows a schematic illustration of the volume of the LV during one heartbeat. The volume retained in the LV after the ejection phase is called the end-systolic volume (ESV) and volume of the LV after the filling phase is called the end-diastolic volume (EDV). The difference between EDV and ESV is called the stroke volume (SV), and is the volume of blood ejected from the LV in healthy conditions. Furthermore, the ejection fraction (EF) is the fraction of EDV ejected in each heart beat, and computed as $\mathrm{EF} = \mathrm{SV}/\mathrm{EDV}$.

During systole, the myocardium of the LV and RV contract and blood is pumped into the aorta and pulmonary artery respectively. The majority of the stroke volume is due to the movement of the AV plane towards the apex, while the rest of the stroke volume is due to the inward movement and thickening of the myocardium during contraction.[12–14] The movement of the AV plane towards the apex during systole means that the volume of the atria increases, aspirating blood from the caval and pulmonary veins.[15]

During diastole, the AV plane returns towards the base of the heart (cf. Figures 1.1 and 1.2), and blood flows from the atria into the ventricles. Diastole can be further divided into the *rapid filling phase*, a stationary period called *diastasis*, and the *atrial contraction*, illustrated in the bottom panel of Figure 1.3.[11,16] In healthy conditions, the rapid filling phase is caused by the recoil of elastic structures in the extracellular space and elastic elements within the myocardial cells themselves.[17–19] This gives rise to a rapid

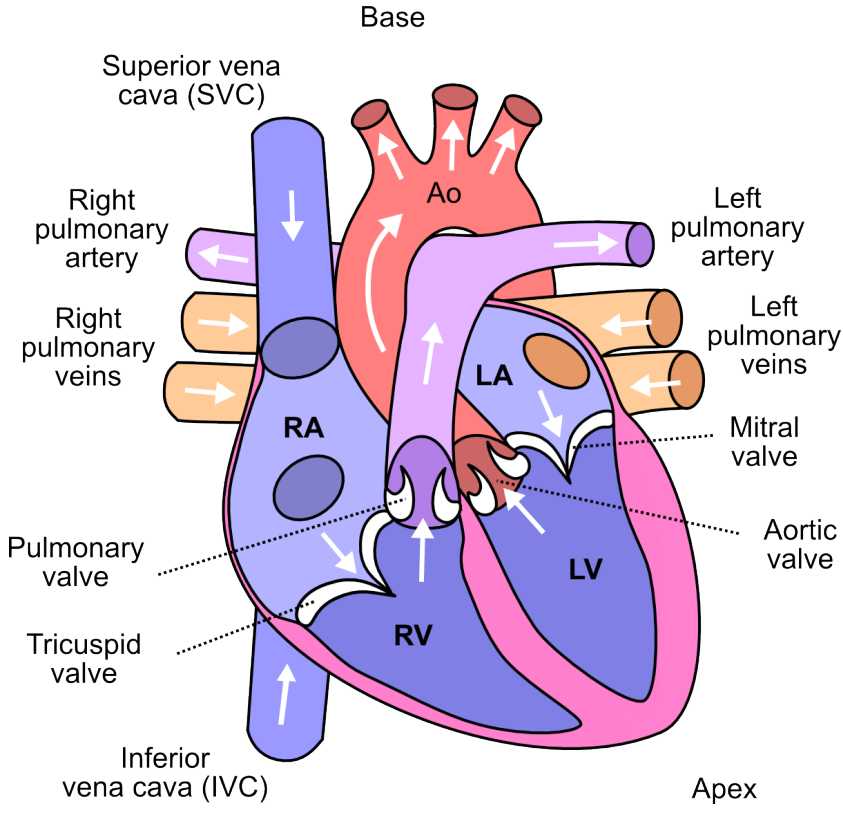

Figure 1.1 – Schematic drawing of a healthy human heart. White arrows indicate the flow of blood under normal conditions.
LV = left ventricle, LA = left atrium, RV = right ventricle, RA = right atrium, Ao = aorta.

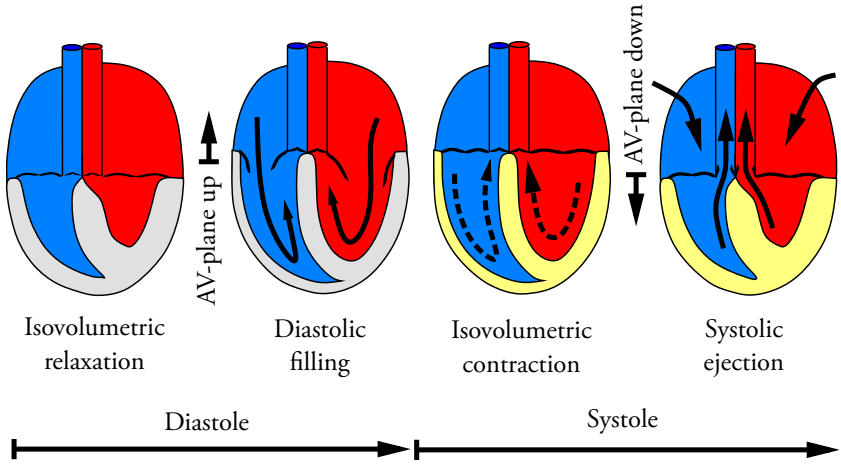

Figure 1.2 – Schematic illustration of the phases of the cardiac cycle. Contraction of the ventricular myocardium is indicated in yellow.

Figure from Jonson B, Wollmer P (Eds): *Klinisk Fysiolgi*. Stockholm: Liber, 3nd edition 2011.[32] Modified and used with permission.

flow from the atria into the ventricles. In the left ventricle, early diastolic recoil creates a suction effect, aspirating blood into the left ventricle.[20–23] After the rapid filling phase, the atria contract, giving rise to a second wave of flow from the atria into the ventricles, called the A-wave.[10,11]

The three phases of diastole can be clearly separated at low heart rates. As heart rate increases, the diastatic interval becomes shorter, and at about 80 bpm, the diastatic phase disappears. At even higher heart rates, the E-wave and A-wave merge into a single diastolic filling phase.[16]

The systolic contraction and diastolic recoil and relaxation can be viewed as a mechanical oscillation around an equilibrium point, the volume at diastasis[24–27] (diastatic volume, DV, see Figure 1.3), although this view has recently been debated.[28–31]

1.1.2 Heart failure

Heart failure is a collection of symptoms connected to an inability of the heart to pump a sufficient volume of blood to meet the needs of the body at normal filling pressures.[33] Heart failure is the end stage of most major cardiac diseases, e.g. ischemic heart disease, diseases of the myocardium and valve dysfunction. Heart failure is strongly associated with a reduced quality of life and increased mortality, and the prognosis for more advanced stages is poor.[3]

Heart failure is commonly divided into *systolic* and *diastolic* heart failure. Systolic heart failure is characterized by an inability of the left ventricle to contract and eject a sufficient amount of blood. Diastolic heart failure, on the other hand, is due to an inability of the ventricles to refill. Furthermore, the term *congestive heart failure* is commonly used to signify a state where the left ventricle cannot maintain a sufficient blood flow at a low filling pressure, giving a high pressure in the pulmonary circulation, which leads to a filtration of fluid into the lungs (pulmonary edema).[10]

Heart failure is commonly preceded by a myocardial infarction (heart attack), where part of the heart muscle is injured due to insufficient blood supply (ischemia). After the infarction, the left ventricle is weakened and may dilate to a very large volume in a process called cardiac remodelling. This may result in a state called dilated cardiomyopathy (DCM) or ischemic dilated cardiomyopathy and systolic heart failure.

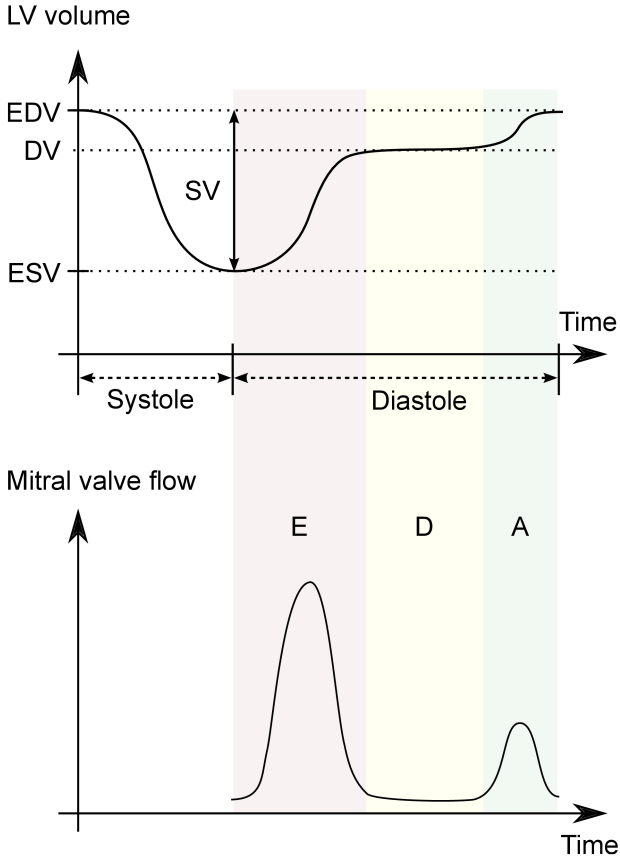

Figure 1.3 – Top: Schematic volume-time curve of the LV at a low heart rate in a healthy person. EDV = end-diastolic volume, ESV = end-systolic volume, DV = diastatic volume, SV = stroke volume.
Bottom: Schematic flow over the mitral valve, i.e. from the left atrium into the left ventricle at a low heart rate in a healthy person. E = E-wave (red), D = diastasis (yellow), A = A-wave (green).

1.2 Magnetic resonance imaging

1.2.1 Basic principles

Magnetic resonance imaging (MRI) is a non-invasive, non-ionizing imaging technique which uses the magnetic properties of the hydrogen nuclei naturally occuring in any tissue containing water in the body to generate images. MRI is well suited for imaging soft tissue, such as the heart, and can also be used to measure velocities.

Although MR is often described in terms of quantum mechanics, a classical description is sufficient for almost all purposes, as described by Hanson.[34] Each hydrogen nucleus (proton) present in the body, mainly bound in water, possesses angular momentum or *spin*, resulting in a magnetic moment. Therefore, each proton behaves as a miniature magnet with a south and north pole. The main magnet in a typical clinical MRI scanner is a helium-cooled superconducting electromagnet, providing magnetic fields ($\mathbf{B}_0$) with magnitudes such as $B_0 = 1.5\,\mathrm{T}$ (Tesla) or 3T over the whole body. The hydrogen nuclei align along $\mathbf{B}_0$, resulting in a net magnetization vector $\mathbf{M}_0$ of the tissue. However, the protons do not align exactly along $\mathbf{B}_0$. The spin axis of each proton *precesses* around $\mathbf{B}_0$ at the Larmor frequency f_0, given by $f_0 = \gamma B_0$, where $\gamma = 42.6\,\mathrm{MHz/T}$ is the gyromagnetic ratio for hydrogen.

An MRI scanner also has gradient coils, which can apply a gradient in the magnetic field in all three spatial dimensions independently. This gives rise to a spatially varying magnetic field, and therefore different resonant frequencies in different parts of the image. This can be used to manipulate the frequency and phase of the precessing magnetization, enabling spatial localization and different contrasts.

Furthermore, a radiofrequency (RF) transmitter is used to transmit RF signals close to the Larmor frequency to manipulate $\mathbf{M}_0$. As long as the net magnetization $\mathbf{M}_0$ is aligned with the main magnetic field $\mathbf{B}_0$, it is impossible to measure it. Therefore, an RF pulse is used to flip $\mathbf{M}_0$ into the transverse plane of $\mathbf{B}_0$. When the magnetization has been flipped into the transverse plane, it continues to precess around $\mathbf{B}_0$ and produces a signal that can be measured by a receiver coil. The receiver coil is usually placed directly on the patient close to the area of interest to maximize the signal to noise ratio.

1.2.2 Cardiovascular magnetic resonance

Magnetic resonance imaging can be applied to the heart, and is then called cardiovascular magnetic resonance (CMR). Figure 1.4 shows example CMR images using cine balanced steady-state free precession (Cine bSSFP) images of the heart in a healthy volunteer, including the common short-axis and long-axis views.[35]

To synchronize the MRI image acquisition to the motion of the heart, an electrocardiogram (ECG) is acquired during the whole image acquisition. Using the ECG trigger, images can be acquired over the whole heartbeat to produce moving images, usually called *cine* images. This is commonly performed by acquiring data from several heartbeats and retrospectively combining it into a single cine loop. Furthermore, respiratory

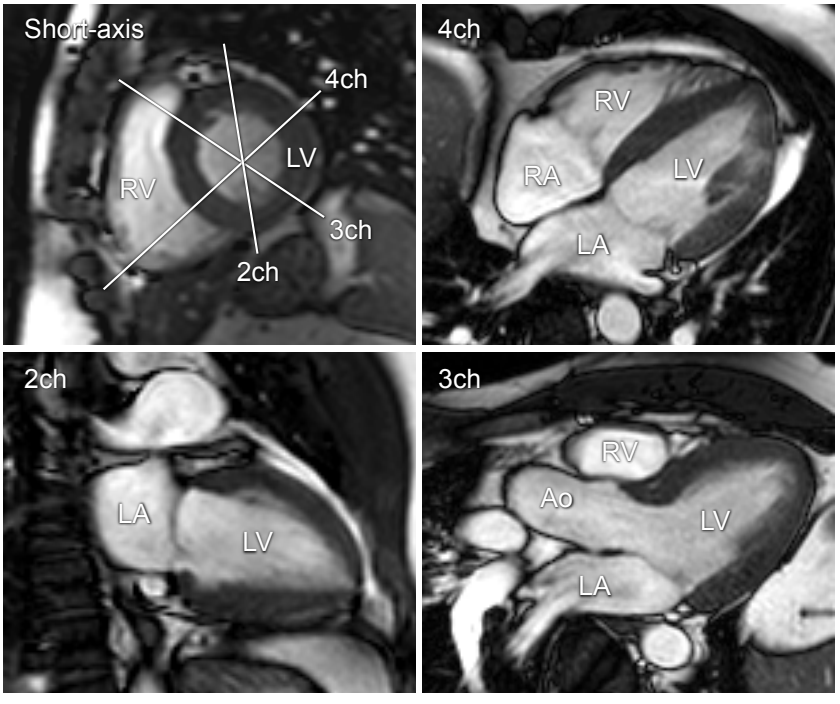

Figure 1.4 – Typical magnetic resonance images of the heart in a healthy volunteer, including the standard short-axis (SA) view and the three long-axis views, called 2-chamber, 3-chamber and 4-chamber (2ch, 3ch and 4ch).[35]

motion is often compensated for either by breathholding for short MRI sequences, or by using a separate acquisiton monitoring the position of the diaphragm, called respiratory navigator, for longer sequences.

1.2.3 Phase contrast velocity measurements

In addition to producing images of anatomical structures, MRI can measure velocities, including blood flow in the heart.[36,37] This is achieved by applying *bipolar gradients* during the MR scanning. For a stationary proton, the first half of the bipolar gradient induces a phase shift in the precession. The second half of the bipolar gradient is equal but in the opposite direction, which gives it an equal but opposite phase shift, resulting in a net phase shift of zero. However, for a non-stationary proton, the phase shifts do not cancel, and the resulting phase shift can be shown to be proportional to the local velocity.[36]

In practice, deviations from an ideal experiment such as inhomogeneous gradients

and B_0 field give a net phase accumulation in the signal even in the situation of zero flow. Therefore, two scans are performed in sequence, with different velocity encoding gradients, e.g. one scan with the gradient on and the other with the gradient switched off, or two scans with velocity encoding gradients of different polarity.[38] In terms of the difference in the first gradient moment in the flow encoding direction between the two scans (ΔM_1), the induced phase shift ϕ_v for a velocity v can be shown to be

$$\phi_v = \gamma \Delta M_1 v, \tag{1.1}$$

where γ is the gyromagnetic ratio for hydrogen. Since the phase shift is limited to the range $(-\pi, \pi)$, there is a maximal velocity that can be encoded without aliasing between one phase value and several velocities. This maximal velocity is usually called the velocity encoding (*VENC*). The noise σ_v in the velocity map can be shown to be proportional to VENC,[39] as

$$\sigma_v \propto \frac{\text{VENC}}{\text{SNR}_m}, \tag{1.2}$$

where SNR_m is the signal-to-noise ratio in the MR magnitude image. Therefore, the VENC must be set high enough to avoid velocity aliasing, but low enough to obtain acceptable noise levels in slow flow.

Velocity encoding can be applied in one direction and in one image plane to measure the volumetric flow through a blood vessel of interest, usually called 2D flow or 2D PC-MR. By collecting data in a three-dimensional volume, and applying the velocity encoding gradients in three directions sequentially, a three-dimensional, three-directional and time-resolved flow measurement can be performed.[39,40] This is usually called 4D PC-MR, 4D PC-MRI or 4D flow.[41,42]

The simplest way to encode three velocity directions is by acquiring one scan without velocity encoding for the baseline phase offset, and then three additional scans, each with one velocity gradient orthogonal to the other two scans. The resulting sequence is called a four-point referenced scan.[43] Four scans with different combinations of encoding gradients can also be used, in a method called four-point balanced or Hadamard encoding.[39,44] The balanced encoding gives a potential 50-60% increase in signal-to-noise ratio at the expense of more complicated velocity aliasing behavior. Additional scans with multiple VENCs can be used to correct aliasing errors, at the cost of prolonged scan time, e.g. five-point[45] or nine-point[46] encoding. The theoretical dependence of the noise in 4D PC-MR on the VENC parameter has been verified experimentally.[47]

The main strength of 4D PC-MR acquisitions is the comprehensive coverage of the three-dimensionality and time-dependence of intracardiac blood flow. The main limitations of the technique are limited temporal resolution (about 50 ms), limited spatial resolution (2-3 mm), and long scan times (25-35 minutes). Due to the long scan time, a single 4D PC-MR acquisition uses data from several hundred heartbeats. This means that a 4D PC-MR acquisition shows large-scale flow features present in the majority of heart beats, and small-scale uncorrelated fluctuations will not be visible.[9]

1.2.4 Phase contrast accuracy and validation

The accuracy and precision of 2D PC-MR flow measurements has been extensively validated against planimetric CMR stroke volume measurements,[48–51] timer and beaker,[49,52,53] doppler ultrasound,[50] cardiac catheterization[54,55] and radionuclide angiography.[52]

However, 2D PC-MR sequences have displayed some issues with phase background errors, i.e. a small, but clinically important offset in velocities which varies slightly over the measurement area and over time.[56–58] Background errors due to Maxwell effects when multiple gradients are used simultaneously can be theoretically predicted and are therefore compensated in the MR scanner software.[59] Further phase background may be caused by eddy currents induced by gradient switching and inhomogeneities in the main magnetic field or gradients. Background correction using a separate background scan[60] or a polynomial fitting algorithm to stationary tissue[61,62] may be necessary, especially for quantitative flow measurements.

Validations of 4D PC-MR have been performed by using 2D PC-MR as the reference standard at 1.5T.[63–65] These studies are limited to quantifying the mean flow over time in one fixed location. Furthermore, these studies do not consider the effect of velocity errors on particle tracing, a common method for visualization and quantification of 4D PC-MR,[66–68] which accumulates errors along computed particle paths in the full region of interest. Data at 3T, where a higher signal-to-noise ratio promises better accuracy and precision compared to 1.5T, was lacking when work on this thesis was started.

Independent velocity measurement techniques have also been used to validate 4D PC-MR. Elkins et al.[69] used particle imaging velocimetry (PIV) in a turbulent, but non-pulsatile flow, i.e. the effects of temporal variation in the flow could not be determined. Knobloch et al.[70] used particle tracking velocimetry (PTV) to validate 4D PC-MR measurements of velocity and turbulence in a pulsatile, compliant silicone model of a human aorta. However, due to differences in the phantom setup for PTV and 4D PC-MR, agreement could only be determined up to a *post hoc* correction factor. Furthermore, Nilsson et al. used a phantom consisting of a cylinder rotating at a fixed velocity to validate 4D PC-MR.[71] While this setup gives a well-defined velocity field for validation purposes, the model includes only small spatial gradients in velocity and no temporal gradients, and sufficient stability in the rotation speed was not acheived in this first study.

1.3 Laser methods for measurement and visualization of flow

1.3.1 Particle imaging velocimetry

Particle imaging velocimetry (PIV) is a laser method for measuring the velocity of a fluid.[72,73] The basic principle of PIV is to add tracer particles to the flow, illuminate them using a laser, and take images of the laser light that is reflected in the particles. For

optimal results, the particles should be small enough to not alter the flow conditions, and have a density similar to the fluid being studied, e.g. hollow glass spheres with density $990\,\mathrm{kg/m^3}$ and diameter $10\,\mu\mathrm{m}$ for use in water at room temperature. Under these conditions, the velocity of the particles will be a good indicator of the fluid velocity.

To image the particles, a special lens assembly is used to create a laser sheet, i.e. a narrow laser beam is widened in one direction to illumine a two-dimensional plane of interest in the experiment. A camera is mounted perpendicular to the laser sheet, which can then take images of the light reflected in the particles.

To obtain velocity measurements, two images are taken with a fixed time delay Δt. Figure 1.5 shows how velocity fields are computed from a pair of images using cross-correlation in smaller interrogation areas. Peaks in the cross-correlation correspond to the shift between the two exposures, which allows computation of a velocity vector based on the shift between the exposures in the interrogation area, the time delay and the pixel spacing.

Error sources in PIV measurements include flow through the measurement plane, camera calibration and perspective errors, too large or too small pixel shift between the two images, and errors in cross-correlation peak detection.

1.3.2 Planar laser-induced flourescence

Planar laser-induced flourescence (PLIF) is a laser method for visualization of fluid motion.[74] The experimental setup with laser and camera is very similar to PIV, indeed similar enough that techniques exist to perform both PIV and PLIF simultaneously.[75,76] For PLIF, a flourescent dye is added to the fluid under study. The dye is chosen so that it absorbs the incoming laser light and has an emission peak at a longer wavelength. The light reaching the camera will then consist of reflected laser light (usually 532 nm) and flourescent light at longer wavelengths, e.g. with an emission peak around 555 nm for the commonly used dye Rhodamine 6G (Rhodamine 590).[77] By filtering out the laser light, images of the flourescent light in the laser sheet can be acquired. Areas with a high dye content will then appear bright, and areas with a low dye content will appear dark, enabling visualization of flow, or concentration measurements after calibration.

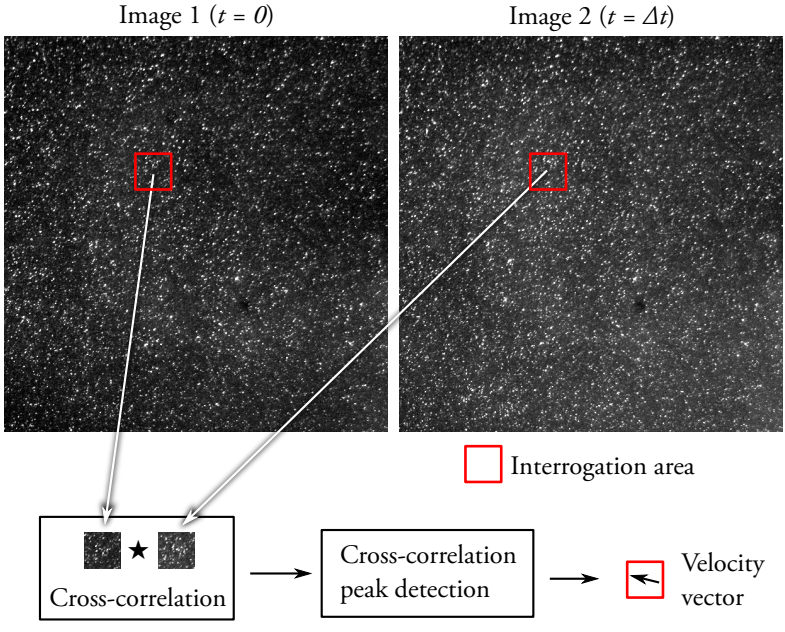

Figure 1.5 – Principle of particle imaging velocimetry (PIV). First, two images with a small time delay are taken of particles in the flow (white dots). The images are then divided into smaller interrogation areas, typically 32x32 pixels in size (red squares). Cross-correlation is then used to find the pixel shift between the two images in the interrogation area. The pixel size, pixel shift and the time delay between images can then be used to compute the velocity vector in each interrogation area.

1.4 Flow visualization

To study 4D blood flow in the heart, the resulting data must first be *visualized*, i.e. shown as an image to enable researchers to gain an intuitive understanding of the flow and form hypotheses that can later be tested. Since 4D PC-MR data is three-dimensional, time-resolved and contains information about flow in all three directions, no single visualization can be used.[78] Therefore, different visualization methods have been developed, each displaying a different aspect of the flow. Furthermore, user studies on two-dimensional and three-dimensional stationary velocity fields have shown that the choice of visualization method influences the impression of the flow,[79,80] an effect which can only be expected to be increased for three-dimensional, time-resolved flows.

1.4.1 Types of flow visualization

Flow visualization methods can be classified into three categories: direct, integral and feature-based.[81]

Direct methods use little or no processing of the data. Examples include color-coding of a plane through the flow by velocity or displaying velocity vectors. Direct visualizations are straightforward to use and require almost no computational effort, but may not show all aspects of the flow. Direct visualizations have been applied to 4D PC-MR data, e.g. using vector plots.[82]

Feature-based methods aim to extract interesting objects from the flow. Feature-based methods can be complex and computationally expensive, but may give large amounts of information about the flow. Vortex core extraction is a feature-based visualization method previously applied to 4D PC-MR blood flow.[83]

Integral or *geometric* methods use velocity data to compute the motion of virtual particles in the fluid.[84] This class of methods is also called *Lagrangian*.[85] Particle tracing is an integral method that is commonly used to visualize 4D PC-MR flow data, where virtual particles are seeded in the flow and integrated along the velocity field to show the motion of the fluid.[66,78] Particle tracing has the main advantage that it gives an intuitive presentation of the flow. Its main drawback is that the position, timing and density of the emitted particle is up to the user. Therefore, the resulting visualization is highly user-dependent.

1.4.2 Lagrangian coherent structures

Lagrangian Coherent Structures (LCS) is a recently introduced method that can be used to simplify analysis of measured flow data by separating the flow into regions of dynamically different behavior. In terms of the classification of visualization methods in Section 1.4.1, LCS is an integral/geometric or feature-based method. LCS have previously been used successfully in a diverse set of applications, including blood flow computations[86,87] and measurements[88] and ocean surface pollution.[89]

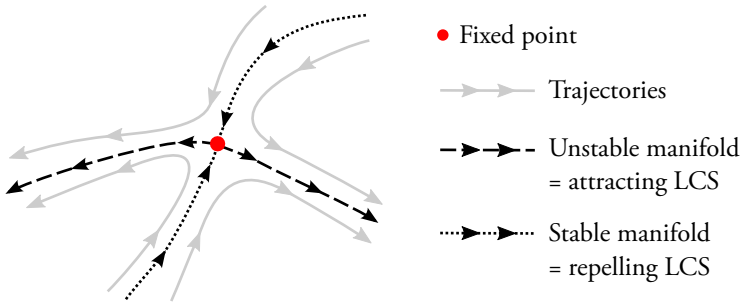

Figure 1.6 – Illustration of the Center Manifold Theorem (stable and unstable manifolds) and Lagrangian Coherent Structures (LCS). In a time-independent flow, a fixed point (red) admits a stable manifold (dotted black line) and unstable manifold (dashed black line). The stable manifold consists of trajectories that converge to the fixed point, and the unstable manifold consists of trajectories that diverge from the fixed point. Stable and unstable manifolds form separators that can be used to better understand the flow. Stable and unstable manifolds correspond to repelling and attracting LCS respectively. However, LCS can also be used in time-dependent flows.

To introduce LCS, we first consider time-independent flow, where the velocity $\mathbf{v} = \mathbf{v}(\mathbf{x})$ depends only on the position $\mathbf{x}$. The Center Manifold Theorem, illustrated in Figure 1.6 states that *stable and unstable manifolds* can be connected to fixed points of the flow, i.e. points $\mathbf{x}$ where $\mathbf{v}(\mathbf{x}) = 0$. The manifolds determine the overall structure of the flow and act as separators, making them a powerful tool for analysis of time-independent systems.

The Center Manifold Theorem requires a steady flow with one or several fixed points, making it unsuitable for analysis of blood flow in the heart. Haller and Yuan [90,91] instead considered divergence and convergence of trajectories as interesting in their own right, even without a fixed point. Divergence and convergence of trajectories over a finite time interval $[t_0, t_1]$ are measured using the *finite-time Lyapunov exponent* (FTLE) $\sigma_{t_0}^{t_1}(\mathbf{x})$, defined as

$$\sigma_{t_0}^{t_1}(\mathbf{x}) = \frac{1}{|t_1 - t_0|} \log \left\| \frac{d\phi_{t_0}^{t_1}(\mathbf{x})}{d\mathbf{x}} \right\|_2 . \tag{1.3}$$

The vector-valued function ϕ is called the *flow map*, and maps the position of a particle located at the position $\mathbf{x}$ at time t_0 to its position at time t_1. The Jacobian $d\phi/d\mathbf{x}$ measures the spatial rate of change of the flow map. Therefore, if the Jacobian of ϕ is large (measured in operator 2-norm), a small perturbation in $\mathbf{x}$ gives a large difference in

the particle end positons, which means that particles close to $\mathbf{x}$ have diverged (if $t_1 > t_0$) or converged (if $t_1 < t_0$). In three dimensions, *repelling* LCS are defined as surfaces of high forward-time FTLE ($t_1 > t_0$), i.e. surfaces where particles on either side will diverge. Similarly, *attracting* LCS are defined as surfaces of high backward-time FTLE ($t_1 < t_0$), i.e. surfaces where particles on either side will converge.

Since the introduction of LCS by Haller and Yuan,[90,91] theory and applications have evolved rapidly. Shadden et al. showed that LCS, as defined from FTLE ridges, act as flow separators in the sense that the flow over an FTLE ridge is negligible when $|t_1 - t_0|$ is large and the FTLE ridge rotates at a speed comparable to the local Eulerian velocity field.[92] Olcay et al. determined the sensitivity of LCS identification with respect to noise and temporal and spatial resolution.[93] Furthermore, several other divergence measures have been developed, such as the Finite-Size Lyapunov Exponent (FSLE) and FTLE maximum.[94]

1.5 Vortex ring formation

The formation of a rotating fluid mass, called a *vortex ring*, has been observed in the left ventricle during early rapid filling, both using in vitro models of the heart[95,96] and in vivo.[83] Vortex ring formation has been suggested as a mechanism for optimal transport of blood from the left atrium to the left ventricle,[97] and has been investigated as a potential marker of diastolic function of the left ventricle.[98–100]

Vortex rings have been extensively investigated both theoretically and in in laboratory models, Comprehensive reviews of theory and experiments have been written by Shariff and Leonard[101] and Lim and Nickels.[102]

Vortex ring formation is connected to a characteristic LCS pattern, as shown in Figure 1.7. Therefore, it has been suggested that LCS can be used to define the boundary of the vortex ring.[103–105]

1.5.1 Vortex formation time or vortex formation ratio

The formation of vortex rings has been extensively studied using in vitro models. In the most simple case, a piston is used to push a bolus of fluid at the speed U through a circular nozzle with diameter D, as shown in Figure 1.8. The piston travels a total length L in each pulse. In this setup, vortex formation can be characterized by two dimensionless quantities: the Reynolds number $\mathrm{Re} = UD/\nu$, where ν is the kinematic viscosity of the fluid, and the the *stroke ratio* L/D.

The stroke ratio L/D is also referred to as *vortex formation time*, denoted VFT or T^*. The rationale for the term "time" can be seen by rewriting the stroke ratio as

$$\frac{L}{D} = \frac{UT}{D} = T\frac{U}{D} \overset{\text{def.}}{=} T^*, \tag{1.4}$$

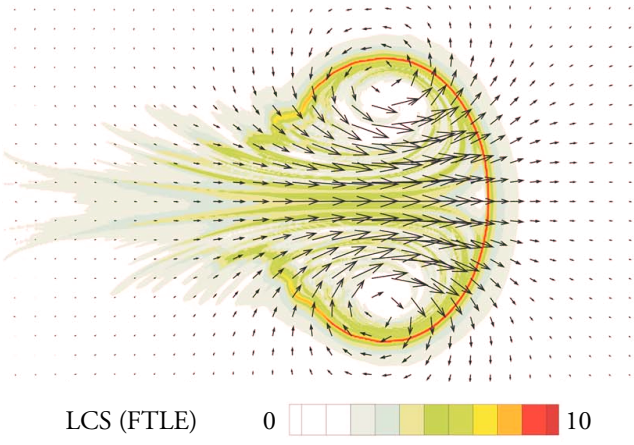

Figure 1.7 – Lagrangian Coherent Structures (LCS) in a vortex ring in water, generated with the equipment in Figure 1.8. The vortex ring, which is assumed to be symmetric along the line of propagation, moves from left to right. Black arrows show flow velocity direction and magnitude. The red line shows an LCS indicating the leading edge of the vortex. The volume of the vortex ring can be defined as the volume inside the red LCS boundary. LCS are defined as lines with high values of the Finite-Time Lyapunov Exponent (FTLE), computed from the flow data.

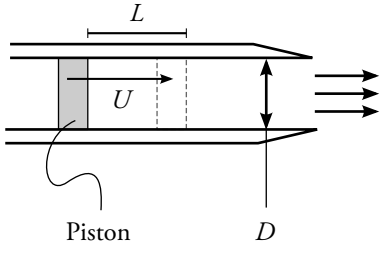

Figure 1.8 – Experimental apparatus for generation of vortex rings used in previous studies. [97,106–109] A piston pushes a volume of fluid into an ambient water volume through a circular nozzle with diameter D. The piston velocity is U and the stroke length is L.

where T is the time required for ejection. This suggests that L/D can be interpreted as a nondimensional time scale for vortex ring formation. Furthermore, the ratio L/D can be interpreted as a non-dimensional measure of the total amount of circulation produced by the boundary layer on the inner nozzle wall during vortex ring formation. [110]

However, to avoid confusion between the physical time period required for generation of vortex rings and the formation number, the term vortex formation time will be avoided and stroke ratio, formation number or *vortex formation ratio* (VFR) will be used in this thesis.

1.5.2 Optimal vortex formation

Gharib, Rambod and Shariff[97] showed that a stroke ratio $L/D \lessapprox 4$ results in a single vortex ring, and that an $L/D \gtrapprox 4$ leads to a vortex ring followed by a trailing jet, as shown in Figure 1.9. This limiting stroke ratio is also called the *formation number*, denoted $(L/D)^*$ or T^*_{lim}. The existence of T^*_{lim} can be explained by the inability of the vortex ring to increase its circulation beyond a certain limit. [97,111,112]

The formation number has been shown to lie in the interval $3.5 < T^*_{\text{lim}} < 4.5$ for a wide range of Reynolds numbers, piston velocity programs and nozzle geometries. [97,113–116] The formation number T^*_{lim} depends slightly on the piston velocity as a function of time[97] and the exit geometry. For instance, a slowly increasing piston velocity gives $T^*_{\text{lim}} \approx 4.5$, and ejecting the fluid from an orifice in the wall of the fluid container instead of using a pipe gives $T^*_{\text{lim}} \approx 3.6$. [97,113,114]

Exceptions to the stability of the formation number include time-varying nozzle diameters, which can increase the formation number as far as $T^*_{\text{lim}} \approx 8$, and numerically generated exit velocity profiles, which can give $T^*_{\text{lim}} \approx 1$. [113,117] For very low Reynolds numbers ($150 < \text{Re} < 260$), the formation number has been shown to be slightly increased to the range 4-6. [118] Furthermore, a background co-flow reduces the formation number, [107] while a counter-flow may increase it. [119]

The formation number sets a limit to the amount of fluid that can be ejected through a nozzle of a certain diameter without generating a turbulent jet. This led Gharib, Rambod and Shariff to hypothesize that the formation number leads to an optimized method for fluid transport in the left ventricle:

> *The mere existence of the formation number is intriguing since it hints at the possibility that nature uses this time scale for some evolutionary incentives such as optimum ejection of blood from the left atrium to the heart's left ventricle* [...]
>
> Gharib M, Rambod E, Shariff K: A universal time scale for vortex ring formation. Journal of Fluid Mechanics 1998, 360:121–140. [97] Reproduced with permission.

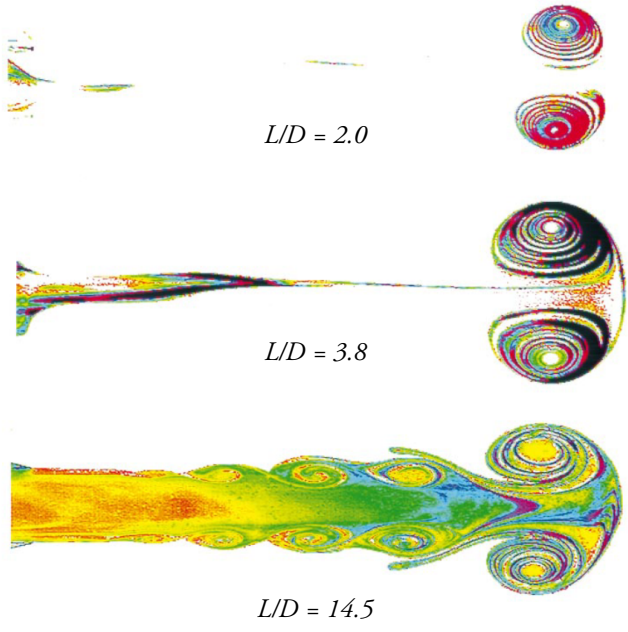

Figure 1.9 – Visualization of vortex rings generated by Gharib, Rambod and Shariff[97] using the apparatus shown in Figure 1.8, for different stroke ratios L/D. For $L/D \lessapprox 4$, a single vortex ring forms. When $L/D \gtrapprox 4$, the vortex ring is followed by a trailing jet.

Source: Figure 3 from Gharib, M., E. Rambod, and K. Shariff. A universal time scale for vortex ring formation. J. Fluid Mech. 360:121–140, 1998.[97] Copyright 1998, Cambridge University Press. Reprinted with permission from copyright holder and author.

1.5.3 Vortex ring mixing

Rotation of the fluid during vortex ring formation leads to convective entrainment of ambient fluid[104,120], illustrated in Figure 1.10. Consequently, both ejected fluid from inside the cylinder and ambient fluid pulled from the vicinity of the nozzle is included in the final vortex ring. The ratio between ejected fluid volume and total volume of the vortex ring is called the *entrainment fraction*.

Müller and Didden[108] used previously published data[106,109,110] to compute the entrainment fraction for L/D between 0.5 and 3.3. For $L/D < 1$, the entrainment fraction was constant around 40%. For $L/D > 1$, entrainment fraction decreased with increasing L/D. Müller and Didden then extrapolated the data to even higher L/D and predicted that the entrainment fraction reaches 0% at $L/D \approx 3.7$. This further reinforces that $L/D \approx 4$ is the upper limit for the formation of a single vortex ring, after which a trailing jet emerges. Later experiments confirmed these findings for L/D between 0.5 and 2.0.[104]

The entrainment fraction also depends on the temporal velocity profile during the formation of the vortex ring,[104] and increases over the life of the vortex ring due to diffusive entrainment.[105,121,122]

1.5.4 Vortex ring formation in the heart

Early studies on vortex ring formation in the left ventricle of the heart were performed using in vitro models.[95,96,123] The vortex ring was later observed in vivo using magnetic resonance velocity mapping and vortex core detection algorithms.[83] Vortex ring formation seen in doppler echocardiography has been described as an abnormal flow pattern in patients examined after myocardial infarction in the acute setting.[124]

After observing the existence and stability of the formation number for vortex rings generated in water tanks, Gharib et al. hypothesized that vortex ring formation may be optimal for the heart in the sense that it transfers the largest possible amount of blood from the left atrium to the left ventricle without forming a turbulent jet (see Section 1.5.2).[97] In other words, a connection between vortex ring formation and left ventricular diastolic function was postulated.

This hypothesis has been investigated using doppler echocardiography.[98–100,125] However, these studies did not visualize the vortex ring directly. Instead, they computed an analog to the vortex formation ratio (VFR or stroke ratio L/D) using available echocardiographic measures such as end-diastolic volume (EDV) and ejection fraction (EF). However, implicit assumptions on the formation process and symmetry of the vortex ring, which may influence the formation number as discussed in Section 1.5.2, were not investigated.

This limitation nonwithstanding, interesting connections between vortex ring formation and cardiac pumping physiology have been found, e.g. lowered VFR in diastolic dysfunction[99] and Alzheimers disease[125] compared to healthy volunteers and a connec-

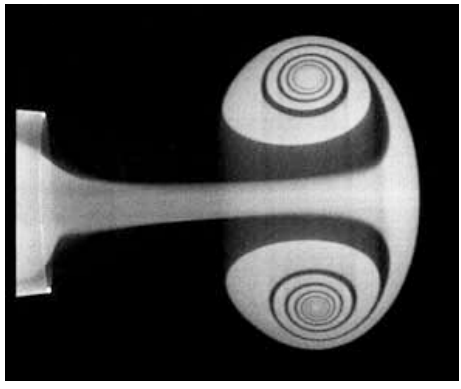

Figure 1.10 – Fluid entrainment during vortex formation, here shown for $L/D = 2.0$[104] visualized using planar laser-induce flourescence (PLIF). After formation, the vortex ring consists of both ejected fluid from inside the cylinder (grey) and ambient fluid (black) pulled into the vortex ring from the vincinity of the nozzle.

Source: Figure 3 in Olcay, A. B., and P. S. Krueger. Measurement of ambient fluid entrainment during laminar vortex ring formation. Exp. Fluids 44:235–247, 2008.[104] Copyright 2008, Springer Verlag. Reprinted with permission from copyright holder and author.

tion between VFR and LV afterload in a pig model.[126] Furthermore, Ghosh and Kovács established a connection between VFR and mechanical parameters such as load, relaxation and stiffness of the LV.[127] Stewart et al. later challenged the connection between diastolic function and vortex ring formation[128] using advanced postprocessing of color M-mode echocardiographic data.[129]

Chapter 2

Aims

The overall aim of this thesis was to develop and evaluate methods for quantification and visualization of blood flow in the human heart measured using 4D phase contrast magnetic resonance imaging (4D PC-MR).

Specific aims concerning accuracy and validation of the techniques, in vivo vortex ring formation, and visualization are stated below.

Accuracy and validation

- Validate stroke volume (SV) measurements in 4D PC-MR, accelerated using SENSE or k-t BLAST, at 1.5T and 3T with 2D PC-MR as the reference standard. – *Paper I*
- Present and characterize a phantom setup for validation of 4D PC-MR velocity measurements against particle imaging velocimetry (PIV) and planar laser-induced flourescence (PLIF). – *Paper II*
- Validate velocity measurements using 4D PC-MR against PIV, and validate quantitative measurements of vortex ring formation using 4D PC-MR against PLIF. – *Paper II*

In vivo vortex ring formation

- Develop a method for computation of Lagrangian Coherent Structures (LCS) for analysis of vortex ring formation and measurement of vortex ring volume (VV) during rapid filling of the LV. – *Paper IV*

- Develop and present a method based on LCS and Volume Tracking (Paper III) to quantify the mixing ratio (MXR) in the vortex ring during rapid filling of the LV. – *Paper V*
- Characterize VV and MXR in healthy volunteers and patients with congestive heart failure. – *Papers IV and V*

Visualization

- Investigate if the visually assessed quality of intracardiac particle tracing visualizations in 4D PC-MR differs between acceleration by SENSE and k-t BLAST. – *Paper I*
- Develop and present Volume Tracking, a new method for visualization of blood flow in the human heart measured by 4D PC-MR, and to investigate if Volume Tracking complements particle tracing and provides incremental information. – *Paper III*

Chapter 3

Methods

3.1 Magnetic resonance imaging

All cardiovascular magnetic resonance (CMR) imaging was performed on Philips Achieva 1.5T or 3T magnetic resonance imaging scanners (Philips Medical Systems, Best, the Netherlands).

Functional cine images were acquired using a balanced steady-state free precession (b-SSFP) sequence in the 2-chamber, 3-chamber, 4-chamber and short-axis views. All anatomical images were acquired during end-expiration and were retrospectively triggered to the R-R interval of the ECG. Typical imaging parameters were: slice thickness 8 mm, no slice gap, in-plane resolution 1.25 x 1.25 mm^2, TE 1.7 ms, TR 3.5 ms, flip angle 60° (1.5T) or 40° (3T).

Three-dimensional, time-resolved, three-component velocity mapping (4D PC-MR) was acquired using a turbo field echo (TFE) sequence[130] with retrospective cardiac cycle triggering using the ECG signal and respiratory gating using a navigator beam. Furthermore, a segmentation factor of 2 and SENSE (SENSitivity Encoding) parallel imaging factor of 2 were used. Typical imaging parameters were TE 3.7 ms, TR 6.3 ms, flip angle 8°. The number of time phases acquired was dependent on heart rate and set to the maximum with a preserved segmentation factor of 2. The spatial resolution was $3 \times 3 \times 3$ mm with a typical matrix size of $80 \times 80 \times 40$ voxels (acquired and reconstructed). The acquired temporal resolution varied between 50-55 ms, resulting in 14-22 phases acquired per heart beat. The acquired data was retrospectively reconstructed to 40 time phases.

In Paper I, an accelerated 4D PC-MR sequence based on k-t BLAST[131,132] (broad-use linear speed-up technique) was also used. A TFE sequence was used with prospective ECG-triggering and a k-t BLAST speedup factor of 5. The net k-t BLAST acceleration factor was 4.1-4.5 (5-fold acceleration with 11 lines of training data in both the ky and kz directions). Typical imaging parameters were: TE/TR 3.7/7.6 ms, flip angle 8°, 15 time

phases acquired and voxel size $3 \times 3 \times 3$ mm^3. The regularization matrix was calculated from the training data, and no additional terms were added. A segmentation factor of 2 was possible in subjects with heart rate below 70 bpm. The temporal resolution varied from 45-60 ms.

For both 4D PC-MR sequences, concomitant gradient effects were compensated by the CMR scanner. Phase unwrapping and first-order phase background correction was performed using a custom plug-in to Segment, a freely available software for cardiovascular image analysis.[133]

Quantitative 2D PC-MR was acquired during free breathing with a non-segmented PC-FFE sequence with retrospective ECG-triggering and no respiratory navigor. Typical imaging parameters were: TE/TR 6.1/9.3 ms, flip angle 15°, 35 time phases and voxel size $1.2 \times 1.2 \times 6$ mm^3.

3.2 Study population and imaging protocols

All studies on human subjects (Papers I and III–V) in this thesis were approved by the Regional Ethical Review Board in Lund, Sweden. Written informed consent was obtained from all subjects.

The imaging protocol for all subjects consisted of 2D PC-MR in the aorta and pulmonary trunk, and 4D PC-MR covering the whole heart, accelerated using SENSE. Furthermore, functional cine images in the short-axis and 2-chamber, 3-chamber and 4-chamber views were acquired.

Paper I

In this study, 13 healthy volunteers were included, of which 9 were male and 4 female The mean age of the subjects was 32 ± 12 years. All volunteers had no history of cardiovascular disease, normal ECG and blood pressure, and an experienced observer verified normal cardiac anatomy and valve function in the CMR images. A 5-channel and 6-channel cardiac coil was used in the 1.5T and 3T experiments respectively. In addition to the 4D PC-MR scan accelerated using SENSE, a separate scan accelerated using k-t BLAST was also performed. The imaging protocol was repeated on 1.5T and 3T on the same day in a random order.

Paper II

Paper II was a phantom-only study, and therefore no human subjects were included. The phantom setup and imaging protocol are described in Section 3.3.

Paper III

In Paper III, 8 healthy volunteers were scanned at 3T (age 35 ± 15 years, 5 male, 3 female). All subjects had normal blood pressure, normal ECG and no history of cardio-

vascular disease. An experienced observer verified normal anatomy, myocardial function and valve function in all healthy volunteers. Furthermore, one patient with dilated ischemic cardiomyopathy due to an anterior infarction, resulting in an ejection fraction of 15%, was included (age 74, male). Functional images and 4D PC-MR using SENSE were acquired at 3T as described in Section 3.1.

Paper IV

In Paper IV, 9 healthy volunteers were included, with mean age 30 ± 9 years (6 male, 3 female). Furthermore, 4 patients with dilated ischemic cardiomyopathy were included (age 65 ± 11 years, 3 male, 1 female).

Paper V

In Paper V, 15 healthy volunteers and 15 patients with congestive heart failure were included. Of the 15 healthy volunteers, 9 were the same as in Paper IV. Out of the 15 patients, 4 were the same as in Paper IV, and 11 additional patients were recruited from a project evaluating cardiac resynchronization therapy (CRT). In these patients, the 4D PC-MR data were acquired without respiratory gating to reduce scan time. Left bundle branch block (LBBB) and prolonged QRS interval in the ECG according to AHA/ACCF/HRS criteria[134] was present in 13 patients (87%) and 5 (33%) were hypertensive (systolic blood pressure $\geq$ 140 mmHg).

3.3 Vortex ring flow phantom

3.3.1 Phantom equipment

For Paper II, a vortex ring generator and a pulsatile pump were designed and built, as shown in Figure 3.1.

The vortex ring generator, shown in cross-section in Figure 3.1a and in 3D in Figure 3.1b, consisted of two parts; a flow rectifier and a water tank. The flow rectifier serves to reduce variations and turbulence in the flow caused by the pump and/or turns in the tubes leading up to the experiment. The flow rectifier accomplishes this by reducing the velocity of the flow through an increased cross-sectional area, and two sections of 2 mm honeycomb to reduce remaining eddies. Finally, a convergent section reduces the cross-sectional area, leading to a nozzle with 25mm inner diameter protruding into the water tank.

The pulsatile pump, shown schematically in Figure 3.1c, was constructed using an integrated linear actuator consisting of a Cool Muscle 2 CM2-56B20X servo motor and an RD-55-T ballscrew (Myostat, Newmarket, ON, Canada). The linear motion of the actuator was coupled to a Festo ADN-32-150-APA pneumatic cylinder (Festo AB, Malmö, Sweden). The end plate of the cylinder was opened and connected to a plastic chamber, separated into two compartments by a rubber membrane, which serves to separate the

flowing water from the pumping mechanism, thereby reducing abrasion in the cylinder. The cylinder side of the membrane chamber was filled with water for all experiments. On the flow side of the membrane chamber, low-resistance check valves (Socla 290P 3/4", Pipeline Controls, Paisley, UK) were connected to enable a filling/emptying pump cycle.

To enable co-registration of MR and PIV/PLIF measurements, a 10 mm thick plastic plate with 3 mm holes spaced 10 mm apart was placed in the tank close to the nozzle, as shown in Figure 3.2. The flow connection between the pump and tank consisted of a 50 mm plastic hose. The large diameter was chosen to minimize acceleration and deceleration pressures in the experiments.

3.3.2 Magnetic resonance imaging

The magnetic resonance (MR) experiment was set up according to Figure 3.3a. In the MR scanner, the tank was positioned with the area around the nozzle close to the isocenter of the magnet for optimal image quality. The pump was placed inside the MR room just outside the 2 mT magnetic field line for safety reasons.

The servo motor in the pump was programmed to emit a timing signal, active during the forward stroke of the pump, which powered a light-emitting diode (LED) connected to the pulseoximetry trigger system of the MR scanner.

The 4D PC-MR flow sequence was kept as similar as possible to the one used for human subjects as described in Section 3.1. Data was acquired in a $64 \times 62 \times 40$ matrix with a resolution of $3 \times 3 \times 3$ mm, and reconstructed to a $80 \times 80 \times 40$ matrix with a resolution of $2.4 \times 2.4 \times 3$ mm. Furthere sequence parameters were: flip angle 8°, TR/TE 6.3/3.7 ms, VENC 100 cm/s, temporal resolution 51 ms, SENSE=2 and segmentation factor = 2. The velocity encoding was performed using a four-point balanced (Hadamard) scheme.

3.3.3 Laser imaging

The particle imaging velocimetry (PIV) and planar laser-induced flourescence (PLIF) measurements were set up according to Figure 3.3b. PIV was performed using a LaVision (Göttingen, Germany) 10 Hz PIV system consisting of a Continuum Systems MiniLite dual-pulse 532 nm Nd:YAG laser with 5 ns pulses, a programmable timing unit (PTU), a Flow Master 3S camera with an optical 532 nm bandpass filter, and a computer with the acquisition and post-processing software Davis 7.2.

A lens assembly was used to focus the laser light into a 1 mm thick vertical laser sheet in the centerline of the water tank. Hollow glass spheres with a diameter of 10 μm and density 990 kg/m^3 were used as marker particles. The image field of view was 115×92 mm. The laser and camera were operated in double-frame mode with 1.5 ms between the two frames. The servo motor trigger signal, marking the start of each pump cycle, was connected to the PTU. The system was setup to acquire one double-frame image

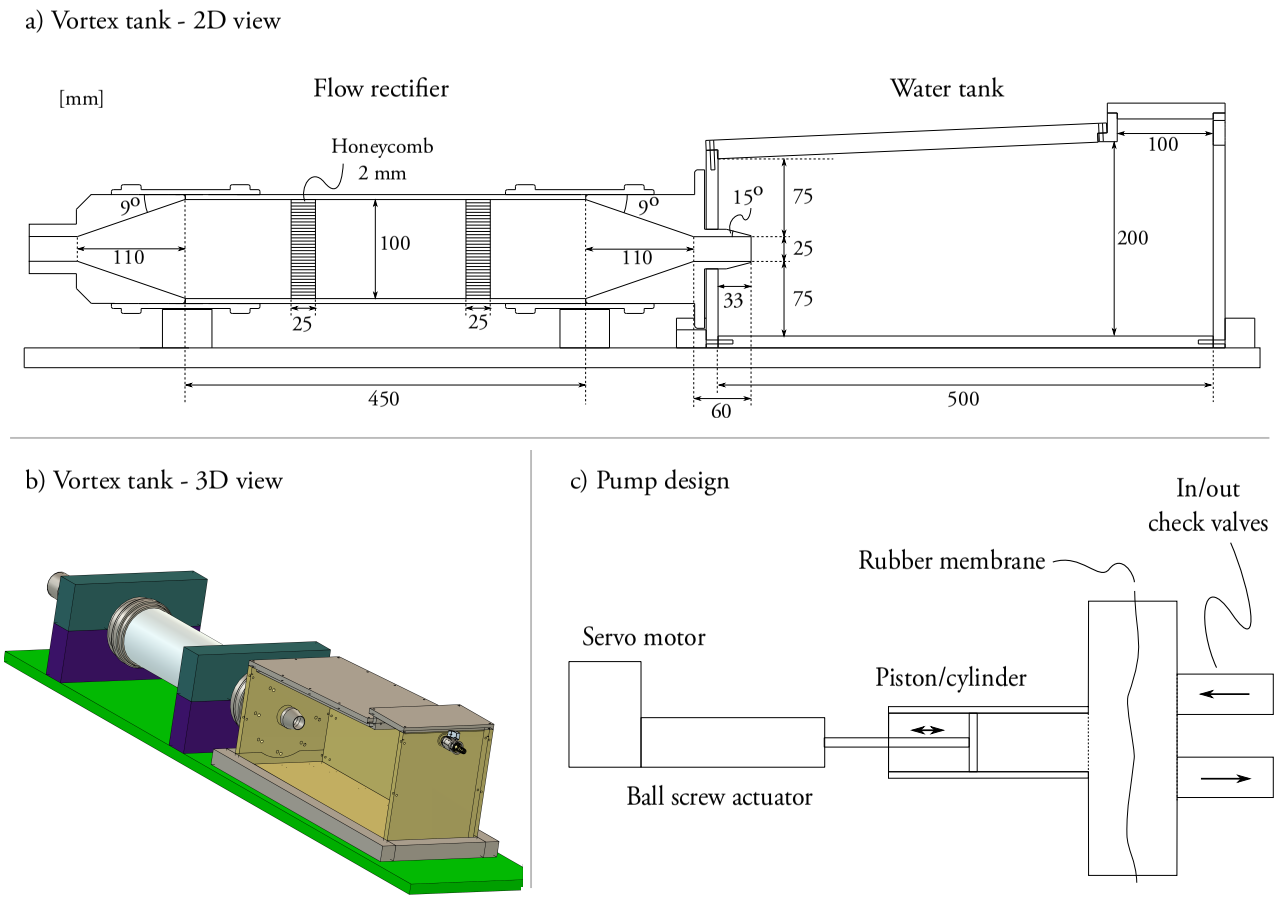

Figure 3.1 – Vortex ring flow phantom designed, developed and used in Paper II. Panel a): 2D cross-section of the flow rectifier and water tank. Panel b): 3D view of the flow rectifier and water tank. Panel c): Schematic view of the custom-built pump.

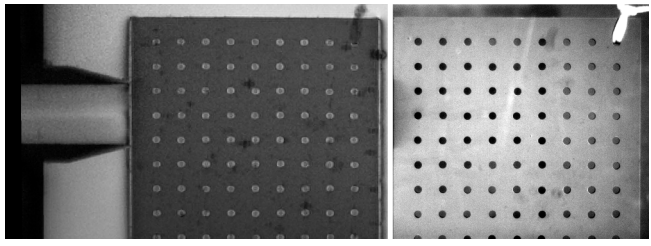

Figure 3.2 – MR (left) and PIV/PLIF camera (right) images of the plastic plate used for co-registration of images. The holes were 3 mm in diameter and spaced 10 mm apart.

Program	VFR, L/D	Volume (ml)	Reynolds number, Re
A	1.0	12.3	5200
B	1.5	18.4	6800
C	2.0	24.5	7700
D	2.5	30.7	8200
E	3.0	36.8	8900

Table 3.1 – Parameters in the vortex tank experiments. VFR = Vortex formation ratio, also called stroke ratio L/D and vortex formation time (VFT). The volume column shows the theoretical volume obtained from the programmed stroke length of the pump.

per pulse, with varying time delay from the trigger signal to image acquisition. Images were acquired for trigger delays between 0 and 600 ms with 10 ms spacing, with 10 double-frame images for each trigger delay.

The raw double-frame images were post-processed using DaVis 7.2 using multi-pass cross-correlation, with a first pass using 64 × 64-pixel interrogation windows, and two subsequent passes using 32 × 32-pixel windows and 50% overlap. A 3 × 3 pixel smoothing filter was applied to the resulting velocity field, and velocity vectors with a magnitude larger than 1 m/s were rejected. The spatial resolution of the final velocity field was 1.45 × 1.45 mm. The mean velocity of the 10 acquisitions for each trigger delay was used for further analysis.

For planar laser-induced flourescence (PLIF) measurements, the same laser and camera setup was used as in the PIV measurements. The flourescent dye Rhodamine 590[74] (Exciton Inc., OH, USA) was added to the water in the tank, while keeping the inflowing water free from the dye. A filter blocking the reflected and transmitted 532 nm laser light was fitted to the camera, giving images of only the flourescent light from the dye. Therefore, bright areas consist of ambient water already in the tank before vortex ring formation, and dark areas consist of inflowing, clean water.

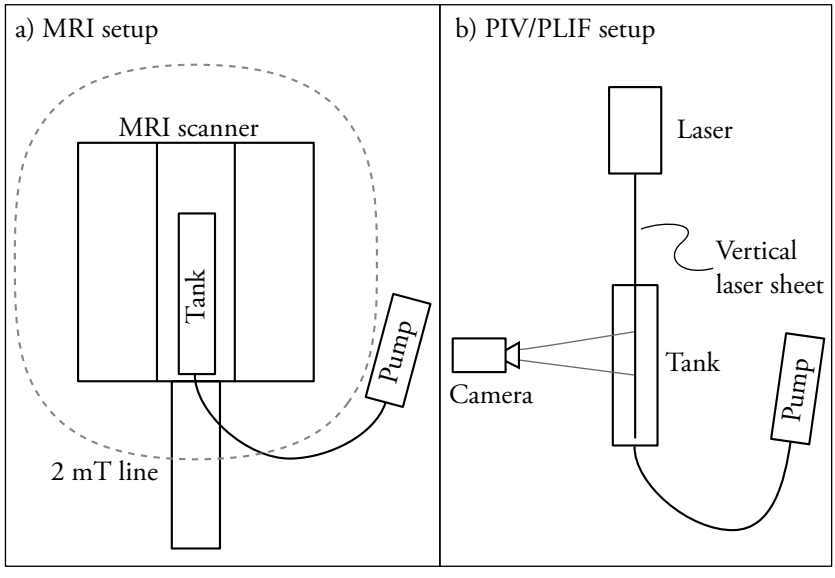

Figure 3.3 – Experimental setup for vortex tank experiments, viewed from above. a) MR setup. b) PIV/PLIF setup.

3.4 Data analysis

This section provides an overview of the analysis of data performed in Papers I–V. Further details are provided in each paper. Details on the computational methods are provided in Chapter 4. Data analysis was mainly performed using custom plug-ins to Segment,[133] a freely available software for cardiovascular image analysis based on Matlab (The Mathworks, USA).

3.4.1 Validation of 4D PC-MR stroke volumes against 2D PC-MR

In Paper I, the 4D PC-MR data was reformatted to the scan planes of conventional 2D PC-MR measurements of stroke volume in the aorta and the main pulmonary artery. Manual delineations of the vessel lumen were performed in the 2D PC-MR datasets and transferred to the reconstructed planes. The instantaneous flow rate for each timeframe was calculated as the surface integral of the through-plane velocity in the delineation for both 2D and 4D PC-MR, and the total SV was computed as the time integral of the resulting flow rate over the cardiac cycle.

3.4.2 Stability assessment of vortex ring flow phantom

To investigate the stability of the vortex ring flow phantom setup (Paper II), velocity fields were measured using particle imaging velocimetry (PIV) on two consecutive days. The tank was emptied of water and repositioned on the supporting table, and the camera and laser were repositioned and recalibrated between the two days. The measured velocities were then compared on a pixel-by-pixel basis.

Correlation between PIV velocities on the two days was assessed using linear regression, and agreement was quantified using Bland-Altman analysis of the pixel-wise differences, with the mean of the two measurements as the reference value.[135] Furthermore, the peak velocity magnitudes in the measurement plane at $t = 400$ ms, i.e. just after the cessation of nozzle flow and vortex ring formation, were compared between the two days.

3.4.3 Validation of 4D PC-MR velocities against PIV

In Paper II, velocity fields measured using particle imaging velocimetry (PIV) in the centerline of the vortex ring phantom were semi-automatically co-registered with the centerline of the tank in the 4D PC-MR measurements using images of the registration plate (Figure 3.2). The 4D PC-MR velocity data was then reconstructed to the same pixel grid as the PIV velocities using linear interpolation in space and time. Finally, velocities were compared on a pixel-to-pixel basis. Correlation between 4D PC-MR and PIV velocities was assessed using linear regression, and agreement was quantified using Bland-Altman analysis of the pixel-wise differences, with the PIV velocities as the gold standard.[135] Furthermore, the peak velocity magnitudes in the measurement plane at

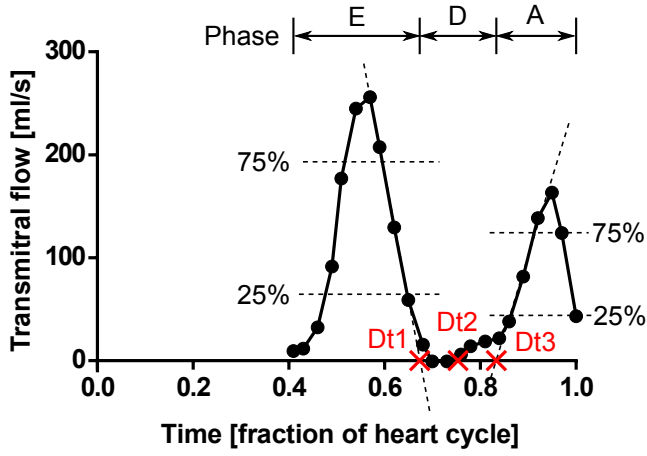

Figure 3.4 – Determination of the time phases of diastole used in Papers III–V. Flow in a plane in the LA close to the mitral valve was reconstructed from the 4D PC-MR data, and used to identify the early rapid filling (E), diastasis (D) and (A) phases, and the time points Dt1, Dt2 and Dt3.

$t = 400$ ms, i.e. at the end of nozzle flow and vortex ring formation, were compared between 4D PC-MR and PIV.

3.4.4 Definition of cardiac time phases

Flow and functional cine MRI images were used in Papers III–V to identify different phases of the cardiac cycle as follows. First, flow in a plane in the LA close to the mitral valve was reconstructed from the 4D PC-MR data. Thereafter, the early rapid filling (E-wave) and atrial contraction (A-wave) flow peaks were identified visually. The 25% and 75% levels of the maximum flow for each peak were then computed, and a straight line through these points were extrapolated to find the end of early rapid filling (Dt1) and the start of atrial contraction (Dt3), as illustrated in Figure 3.4. Dt2 was defined as the mean of Dt1 and Dt3.

3.4.5 Vortex ring volume and mixing ratio: 4D PC-MR

In Papers II, IV and V, the vortex ring volume (VV) and mixing ratio (MXR) were quantified from 4D PC-MR data as follows (illustrated in Figure 3.5):

1. First, Lagrangian Coherent Structures were computed in the image planes of interest, using the numerical methods described in Chapter 4 and Paper IV.

The flow map was computed from the end of rapid filling (Dt1, Dt2 or Dt3, cf. Figure 3.4) backwards in time to the end of systole.

  - In the phantom experiments in Paper II, LCS were computed in a vertical plane in the centerline of the water tank, along the flow direction (long-axis). Furthermore, LCS were computed in slices perpendicular to the flow direction (short-axis) and spaced 1.5 mm apart.
  - In the in vivo studies in Papers IV and V, LCS were computed in 2-chamber, 3-chamber and 4-chamber long-axis views. Short-axis LCS images were also computed, spaced 4 mm apart.

2. LCS indicative of vortex ring formation were manually delineated in the long-axis views. The long-axis delineations were then used as guides for delineations in the short-axis views.

3. The vortex ring volume (VV) was defined as the volume inside the LCS delineations, summed over all slices.

4. The boundary between the left atrium and left ventricle, i.e. the atrioventricular plane, was manually defined as a plane parallel to the short-axis slices. In the phantom experiments, the boundary was determined by the nozzle exit plane.

5. For each pixel inside the vortex ring delineation in the short-axis slices, one particle was traced from the end of rapid filling backwards in time to the end of systole.

6. Each pixel was classified according to its origin:

  - VV_{inflow}: Pixels of fluid originating on the basal side of the AV plane (or inside the nozzle in the phantom experiments).
  - $VV_{mix\text{-}in}$: Pixels of fluid originating on the apical side of the AV plane (or in front of the nozzle), i.e. fluid that was already in the ventricle (or water tank) and has been mixed into the vortex ring.

7. The mixing ratio (MXR) was then defined as $MXR = VV_{mix\text{-}in}/VV$.

3.4.6 Vortex volume and mixing ratio: PLIF

In Paper II, planar laser-induced flourescence (PLIF) imaging was used as the reference standard for vortex ring volume (VV) and mixing ratio (MXR) quantification, as illustrated in Figure 3.6. Manual delineation were used to find VV (Figure 3.6B). Automatic histogram-based thresholding was used to classify pixels inside the delination as inflowing

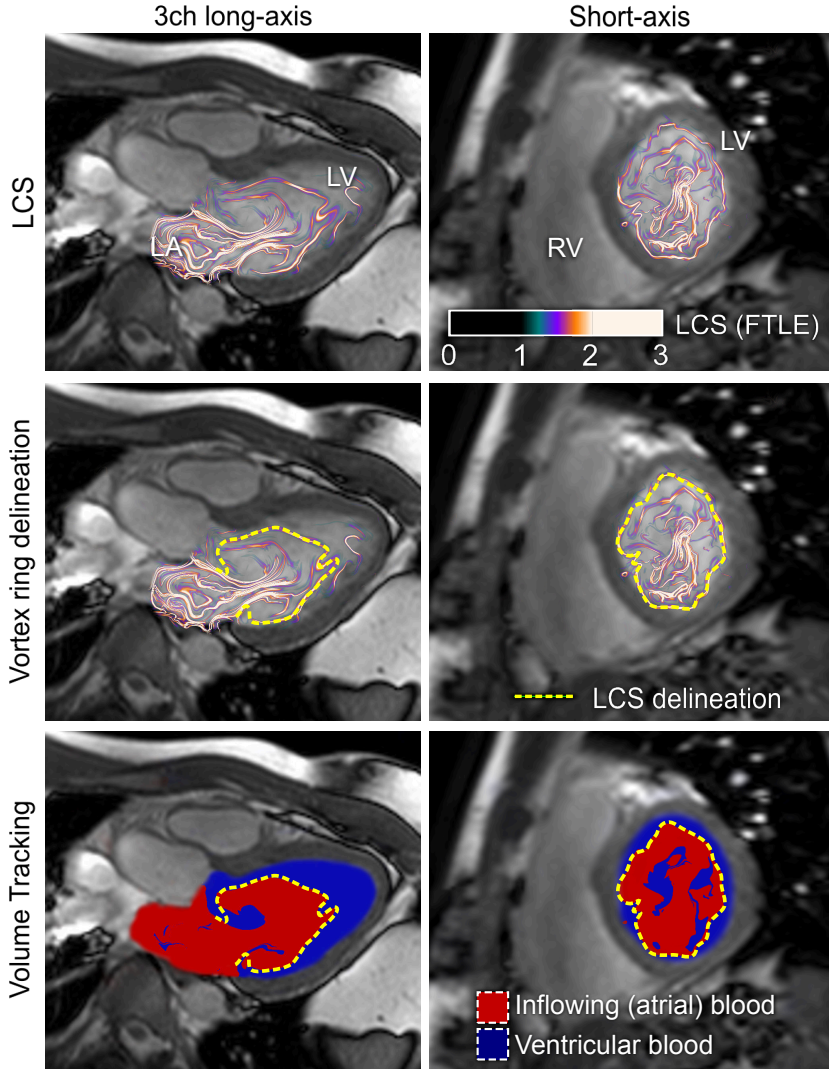

Figure 3.5 – Quantification of vortex ring volume (VV) and mixing ratio (MXR) during early rapid filling of the LV in a healthy volunteer, using Lagrangian Coherent Structures (LCS) and Volume Tracking in 4D PC-MR data. See Section 3.4.5 for details.

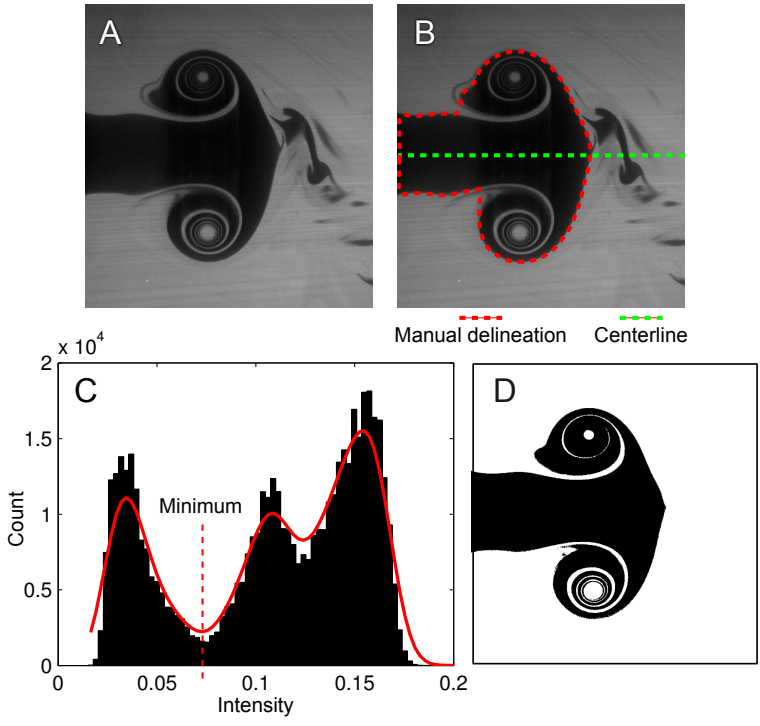

Figure 3.6 – Method for quantification of vortex ring volume (VV) and mixing ratio (MXR) using planar laser-induced flourescence (PLIF) in the vortex ring flow phantom. Panel A: PLIF image. Panel B: Manual delineation of vortex ring contour. Panel C: Histogram-based thresholding of the PLIF image. Panel D: Final classification of inflowing and surrounding water.

or mixed-in. In line with a previous PLIF study on vortex rings,[104] rotational symmetry around the centerline of the flow was assumed, and each pixel contributed a volume

$$V_p = \pi r_p \Delta x \Delta y, \tag{3.1}$$

where Δx and Δy are the pixel spacings in the x and y directions, and r_p is the vertical distance between the pixel center and the vortex ring centerline.

3.4.7 Quality assessment of flow visualizations

In Paper I, the impact of acceleration of 4D PC-MR sequences using SENSE and k-t BLAST on visualization of intracardiac blood flow was assessed as follows. First, particles were emitted in all four chambers of the heart, and particles were released every 10 ms

over the cardiac cycle. One observer, blinded to the acceleration method used, graded the quality of the visualizations based on the amount of particles leaving the blood pool. The following scale was used: 0 – ideal, i.e. all particles behave in a physiological manner, 1 – few particles leaving the blood pool, 2 – moderate amount of particles leaving the blood pool, 3 – large amount of particles leaving the blood pool, indicating poor data quality. The grading was performed for the emitter in each chamber separately, and the mean score was computed for each subject.

3.4.8 Volume Tracking

As further described in Paper III, Volume Tracking enables the researcher to study how a three-dimensional volume moves and deforms in a flow field. This extends particle tracing, which is the most commonly used method for visualization of 4D PC-MR data, from using particles to three-dimensional volumes. Furthermore, the need to choose the density or number of released particles is eliminated. Details on the numerical methods are given in 4 and Paper III.

In Paper III, a spherical volume of blood was selected in the left atrium of each subject and tracked from the end of systole through diastole, thereby visualizing the filling of the LV. The LV blood pool was divided into 21 segments based on the American Heart Association's (AHA) 17-segment model of the LV myocardium,[136] according to Figure 3.7. Segments covered by more than 25% inflowing blood (assessed visually) were considered as inflowing blood. Volume Tracking visualizations were produced, and thereafter two observers performed the classficiation independently.

To investigate the accuracy of the obtained visualizations, a comparison with particle tracing was performed as follows. A Volume Tracking visualization of blood flowing into the LV during diastole was generated. Simultaneously, particles for particle tracing were released in the left atrium. Since the Volume Tracking visualization is designed to display the boundary between inflowing blood and blood that was already in the LV, no particles seeded on one side of the plane should cross the plane at any time. Therefore, the amount of particles that reside on the correct side of the Volume Tracking plane is a suitable indicator of the quality of the Volume Tracking visualization.

3.4.9 Statistical methods

Group values are given as mean $\pm$ standard deviation (SD). Relationships between variables were analyzed using linear regression and Pearson's R^2. Agreement between measurement methods was evaluated using Bland-Altman analysis. In Paper I, differences in peak flows between 2D and 4D PC-MR were analyzed using a paired non-parametric two-tailed test (Wilcoxon). Differences between patients and healthy volunteers (Papers IV and V) were analyzed using a signed rank test (Mann-Whitney U). Statistical significance was defined as a p-value less than 0.05. In Paper III, Cohen's kappa value was used to quantify interobserver agreement for LV inflow analysis.

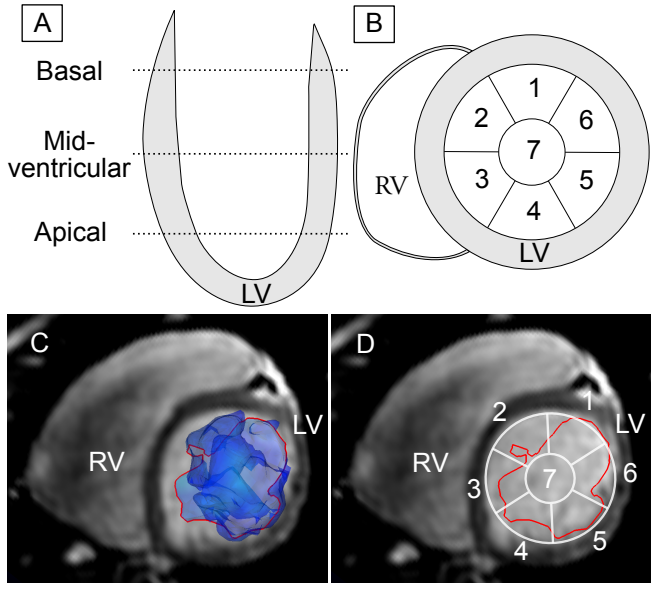

Figure 3.7 – Classification of LV inflow from Paper III. Panel A: Division of the LV into apical, mid-ventricular and basal parts. Panel B: Division of each part into 7 segments, with segment 1-6 along the endocardium adjusted from the AHA standard[136] and segment 7 in the center of the lumen. Panel C: a mid-ventricular short-axis slice and Volume Tracking surface (blue) in a healthy volunteer. The intersection of the Volume Tracking surface with the slice is shown as a red line. Panel D: intersection in red and the segment model from panel B in white.

Chapter 4

Computational methods

4.1 Coordinate systems

During a magnetic resonance imaging (MRI) examination, velocity and function images are taken in different views with respect to each other (see Figure 1.4 on page 8). Therefore, two different coordinate systems must be considered: the global patient-oriented coordinate system, called *LPS* for reasons explained below, and image-oriented coordinate systems which are specific to each image. The LPS and image-based coordinate systems are illustrated in Figure 4.1. Both coordinate systems are Cartesian and orthonormal.

The patient-oriented coordinate system is defined in the DICOM standard.[137] The basis vectors **L**, **P** and **S** are defined from the viewpoint of the patient. **L** (left) is the unit vector pointing towards the left side of the patient, **P** (posterior) is the unit vector pointing towards the back of the patient, and **S** (superior) is the unit vector pointing towards the head of the patient. This provides a global right-handed orthonormal coordinate system in three-dimensional space, which will be called the *LPS coordinate system*. Coordinates of a point with respect to the LPS coordinate system will be denoted $\mathbf{x} = (x_1, x_2, x_3)^T$ and are called *LPS coordinates*, measured in meters from the global origin.

The location and orientation of each image is specified by the *image position* and the *image orientation*. The image position is defined as the center of the pixel in the upper left corner of the image and given in LPS coordinates, denoted **O**. The image orientation is given as two orthogonal unit vectors in LPS coordinates, $\mathbf{d}_1$ and $\mathbf{d}_2$. The vector $\mathbf{d}_1$ points along the rows of the image matrix and $\mathbf{d}_2$ points along the columns of the image matrix. In the case of volumetric image data, such as the 4D PC-MRI velocity data in this thesis, a third direction $\mathbf{d}_3$ is used, orthogonal to $\mathbf{v}_1$ and $\mathbf{v}_2$, i.e. $\mathbf{d}_3 = \mathbf{d}_1 \times \mathbf{d}_2$, where $\times$ is the cross product. Define the *direction matrix* **D** as the matrix with $\mathbf{d}_1$, $\mathbf{d}_2$ and $\mathbf{d}_3$ as column vectors,

Name	Basis vectors	Coordinates
LPS	$\mathbf{L}, \mathbf{P}, \mathbf{S}$	$\mathbf{x} = (x_1, x_2, x_3)^T$
Image-based	$\mathbf{d}_1, \mathbf{d}_2, \mathbf{d}_3$	$\mathbf{y} = (y_1, y_2, y_3)^T$
Pixel indices	$\mathbf{d}_1, \mathbf{d}_2, \mathbf{d}_3$	$\mathbf{I} = (i, j, k)^T$

Table 4.1 – Summary of spatial coordinate systems used, also illustrated in Figure 4.1 and described in Section 4.1.

$$\mathbf{D} = (\mathbf{d}_1\ \mathbf{d}_2\ \mathbf{d}_3)\,. \tag{4.1}$$

The image-based coordinate system is defined by the image position $\mathbf{O}$ and the vectors $\mathbf{d}_1$, $\mathbf{d}_2$ and $\mathbf{d}_3$. Image-based coordinates are denoted $\mathbf{y} = (y_1, y_2, y_3)$ and are measured in meters from the image position $\mathbf{O}$. Therefore, the relationship between the LPS coordinates $\mathbf{x}$ and image-based coordinates $\mathbf{y}$ for a point in space can be written

$$\mathbf{x} = \mathbf{O} + \mathbf{D}\mathbf{y}. \tag{4.2}$$

Pixels in each image are specified using their indices i, j, k and n for the row, column, slice and timestep indices respectively. Let $\mathbf{I} = (i, j, k)^T$ be the column vector of spatial indices. The first row, column, slice and timestep all have index 0. The pixel spacings in the i, j, and k directions are Δi, Δj and Δk respectively, and the timestep is Δt. For convenience, the pixel spacing matrix $\underline{\Delta}$ is defined as

$$\underline{\Delta} = \begin{pmatrix} \Delta i & 0 & 0 \\ 0 & \Delta j & 0 \\ 0 & 0 & \Delta k \end{pmatrix}. \tag{4.3}$$

The image-based coordinates $\mathbf{y}$ of a pixel with indices $\mathbf{I}$ can then be written

$$\mathbf{y} = \underline{\Delta}\mathbf{I}. \tag{4.4}$$

For the velocity interpolation in the following section, the relationship between LPS coordinates $\mathbf{x}$ and pixel indices $\mathbf{I}$ is needed. Combining Equations 4.2 and 4.4, the formula

$$\mathbf{x} = \mathbf{O} + \mathbf{D}\underline{\Delta}\mathbf{I} \tag{4.5}$$

is obtained, or equivalently

$$\mathbf{I} = (\mathbf{D}\underline{\Delta})^{-1}(\mathbf{x} - \mathbf{O})\,. \tag{4.6}$$

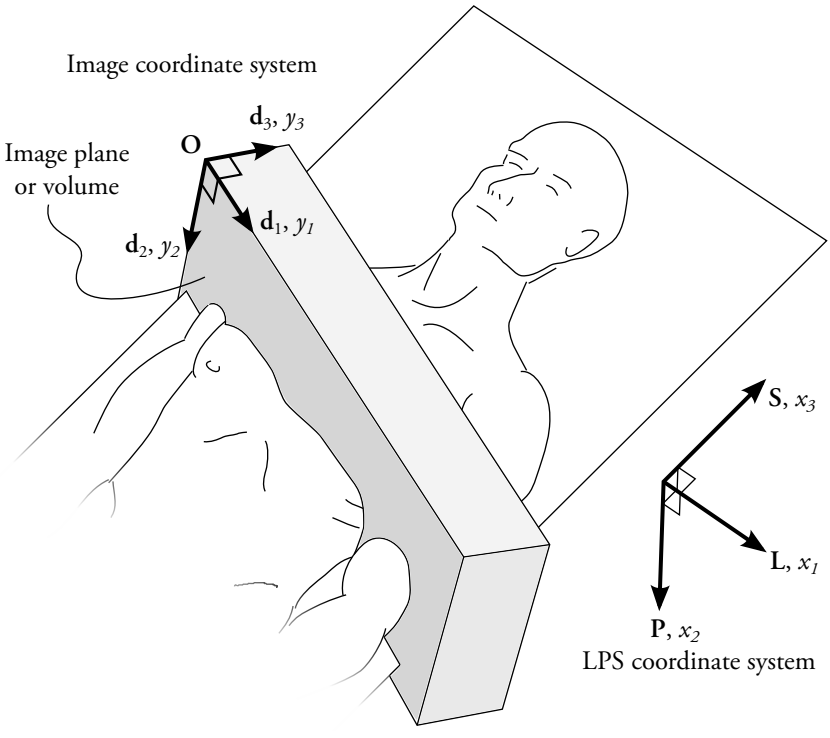

Figure 4.1 – The patient-centered LPS coordinate system and the image-local coordinate system. The **L**, **P** and **S** vectors in the LPS system are aligned with the right-left, front-back (posterior) and feet-head (superior) directions of the patient, and the image coordinate system is aligned with the row ($\mathbf{d_1}$), column ($\mathbf{d_2}$) and through-plane ($\mathbf{d_3}$) directions of the image. See also Table 4.1 for summary. Image by Per Arvidsson.

4.2 Velocity interpolation

In the following section, we will need to evaluate the velocity $\mathbf{v}$ in a position $\mathbf{x}$ that falls between pixel centers and MRI timesteps. In these cases, interpolation in time and space is used, implemented as follows.

The pixel indices i, j and k of the point $\mathbf{x}$ are computed using Equation 4.6. Interpolation weights are then calculated as

$$\begin{aligned} w_i &= i - \lfloor i \rfloor \\ w_j &= j - \lfloor j \rfloor \\ w_k &= k - \lfloor k \rfloor, \end{aligned} \tag{4.7}$$

where $\lfloor i \rfloor$ is the nearest integer smaller than or equal to i. To simplify the following, let $\lfloor i \rfloor = \lfloor j \rfloor = \lfloor k \rfloor = 0$ without loss of generality. Let V^n_{ijk} be the velocity in the voxel i, j, k at timestep n. The interpolated value V^n_{interp} at an MRI timestep n can then be calculated as

$$\begin{aligned} V^n_{\text{interp}} = &V^n_{000}(1-w_i)(1-w_j)(1-w_k) \\ &+ V^n_{001}(1-w_i)(1-w_j)w_k \\ &+ V^n_{010}(1-w_i)w_j(1-w_k) \\ &+ V^n_{011}(1-w_i)w_j w_k \\ &+ V^n_{100}w_i(1-w_j)(1-w_k) \\ &+ V^n_{101}(1-w_i)w_j(1-w_k) \\ &+ V^n_{110}w_i w_j(1-w_k) \\ &+ V^n_{111}w_i w_j w_k. \end{aligned} \tag{4.8}$$

Interpolation was performed for each of the three velocity components separately. In cases where the position $\mathbf{x}$ was outside the image volume, the interpolated velocity was set to zero. Furthermore, linear interpolation between timesteps was used.

4.3 Particle tracing

Particle tracing is a procedure to extract Lagrangian data, i.e. the movement of the fluid, from velocities measured on an Eulerian grid.

First, suppose that the position of a massless particle in the flowing fluid is described by the function $\mathbf{p}(t)$, i.e. the particle is located at the coordinates $\mathbf{p}(t)$ at time t. Then assume that during a small time interval of length Δt immediately following t, the particle moves with the fluid, i.e. with the same velocity as the surrounding fluid. For a small enough Δt, we can write

$$\mathbf{p}(t+\Delta t) \approx \mathbf{p}(t) + \mathbf{v}(\mathbf{p}(t),t)\Delta t, \tag{4.9}$$

or equivalently

$$\frac{\mathbf{p}(t+\Delta t) - \mathbf{p}(t)}{\Delta t} \approx \mathbf{v}(\mathbf{p}(t),t). \tag{4.10}$$

Taking the limit as $\Delta t \to 0$, the ordinary differential equation (ODE)

$$\frac{d}{dt}\mathbf{p}(t) = \mathbf{v}(\mathbf{p}(t),t) \tag{4.11}$$

is obtained. Equation 4.11 has a unique solution if a particle position $\mathbf{p}_0$ is specified at some time t_0, i.e. $\mathbf{p}(t_0) = \mathbf{p}_0$. A solution of Equation 4.11 together with a starting position and time $(\mathbf{p}_0, t_0)$ is called a *trajectory* and is denoted $\mathbf{p}(t)$ or $\mathbf{p}(\mathbf{p}_0, t_0; t)$.

To compute trajectories numerically, a fourth-order Runge-Kutta method was used. Let $\mathbf{p}_l$ be the computed position of the particle at the numerical solution timestep l. The next step $\mathbf{p}_{l+1}$ was computed using the formulas

$$\begin{aligned}
\mathbf{P}'_1 &= \mathbf{v}\left(\mathbf{p}, t\right) \\
\mathbf{P}'_2 &= \mathbf{v}\left(\mathbf{p} + \mathbf{P}'_1\delta t/2, t + \delta t/2\right) \\
\mathbf{P}'_3 &= \mathbf{v}\left(\mathbf{p} + \mathbf{P}'_2\delta t/2, t + \delta t/2\right) \\
\mathbf{P}'_4 &= \mathbf{v}\left(\mathbf{p} + \mathbf{P}'_3\delta t, t + \delta t\right) \\
\mathbf{p}_{l+1} &= \mathbf{p}_l + \frac{\delta t}{6}\left(\mathbf{P}'_1 + 2\mathbf{P}'_2 + 2\mathbf{P}'_3 + \mathbf{P}'_4\right)
\end{aligned} \tag{4.12}$$

All particle tracing computations were performed in the LPS coordinate system, using interpolation of the measured MRI velocities as described in the previous section.

In Papers II, IV and V, a constant time step was used, $\delta t = 5$ ms. In Paper III (Volume Tracking), where the built-in particle tracing engine in the visualization software package Ensight 8.2 (CEI, USA) was used. This particle tracing implementation uses linear interpolation in space and time and an adaptive time-step selection algorithm.

4.4 Lagrangian Coherent Structures

Lagrangian Coherent Structures are defined as surfaces (or lines when viewing a 2D slice of a 3D volume) of high Finite-Time Lyapunov Exponent (FTLE). The computation of the FTLE requires tracing of particles from a regular grid and then computing the Jacobian of the resulting map from particle start positions to end positions.

Although several defintions of the Finite-Time Lyapunov Exponent exist,[94] we base this work on the definition originally proposed by Haller and Yuan:[90,91]

$$\sigma_{t_0}^{t_1}(\mathbf{x}) = \frac{1}{|t_1 - t_0|} \log \left\| \frac{d\phi_{t_0}^{t_1}(\mathbf{x})}{d\mathbf{x}} \right\|_2, \tag{4.13}$$

where ϕ is the *flow map*, which maps a particle's position $\mathbf{x}$ at one time t_0 to its position at another time t_1:

$$\phi_{t_0}^{t_1}(\mathbf{x}) : \mathbf{x} \mapsto \mathbf{p}(\mathbf{x}, t_0; t_1), \tag{4.14}$$

In practice, Equation 4.13 is evaluated in the image-based coordinate system. Since the LPS coordinate system and image-based coordinate system differ only by a translation and rotation (Equation 4.2), the norm of the Jacobian of the flow map is the same in both coordinate systems.

To evaluate Equation 4.13 numerically from the 4D PC-MR velocity data, an MRI image plane of interest was first selected (e.g. a 3ch image of the heart). In this image plane, a regular grid of particles was defined aligned with the image plane, spaced $\delta = 0.8$ mm apart. The value of δ was chosen as a balance between computational cost and resolving details of the FTLE field. Furthermore, to be able to compute the gradient of ϕ with respect to the through-plane direction y_3, particles were also placed 0.8 mm on each side of the image plane, as shown in Figure 4.2. The coordinates $\mathbf{y}_{lmn}$ of the particles can be written

$$\mathbf{y}_{lmn} = \delta\,(l, m, n)^T, \tag{4.15}$$

with $l = 0..L-1$, $m = 0..M-1$, with L and M chosen to fill the chosen image plane with particles, and $n = -1, 0, 1$ to produce particles in the plane and on both sides of the plane.

The LPS coordinates $\mathbf{x}_{lmn}$ of the particle positions $\mathbf{y}_{lmn}$ where then computed using Equation 4.2. Each particle was then traced from time t_0 to t_1 in the 4D PC-MR velocity data according to Sections 4.2 and 4.3, yielding the particle end positions $\mathbf{p}(\mathbf{x}_{lmn}, t_0; t_1)$. These end positions were then converted from LPS coordinates back to the image-based coordinate system, giving the particle end position ϕ_{lmn} for each starting point $\mathbf{y}_{lmn}$.

The derivatives of the flow map were computed using centered finite differences as follows. Let ϕ^1, ϕ^2 and ϕ^3 be the y_1, y_2 and y_3 components of the flow map respectively. The derivatives of ϕ^k, $k = 1, 2, 3$ in each grid point $\mathbf{y}_{l,m,0}$ were then approximated as

$$\begin{aligned}
\frac{\partial \phi^k}{\partial y_1} &\approx \frac{\phi^k_{l+1,m,0} - \phi^k_{l-1,m,0}}{2\delta}, \\
\frac{\partial \phi^k}{\partial y_2} &\approx \frac{\phi^k_{l,m+1,0} - \phi^k_{l,m-1,0}}{2\delta}, \\
\frac{\partial \phi^k}{\partial y_3} &\approx \frac{\phi^k_{l,m,1} - \phi^k_{l,m,-1}}{2\delta}.
\end{aligned} \tag{4.16}$$

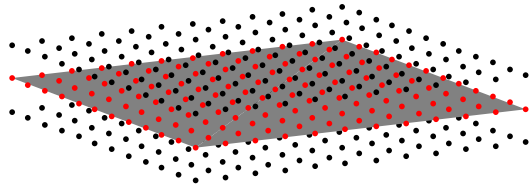

Figure 4.2 – Grid used for LCS computations. The MRI imaging plane of interest is shown in gray. An equisdistant grid of particles spaced $\delta = 0.8$ mm apart was placed in the imaging plane (red dots), and $\delta = 0.8$ mm on each side of the imaging plane (black dots).

These approximations are then used to form an approximate Jacobian matrix $\tilde{J}_{ij}^{lm}$ for each point (l, m) in the image with elements

$$\tilde{J}_{ij}^{lm} = \frac{\partial \phi^i}{\partial y_j}. \tag{4.17}$$

The numerically computed Finite-Time Lyapunov Exponent (FTLE) $\tilde{\sigma}^{lm}$ in the image point (l, m) is computed as

$$\tilde{\sigma}^{lm} = \frac{1}{K} \log \left\| \tilde{J}^{lm} \right\|_2 . \tag{4.18}$$

Note that compared to Equation 4.13, the normalization by $|t - t_0|$ is replaced by a normalization factor K. The normalization factor was computed for each image by constructing a histogram of FTLE values for pixels in the image and taking the 95$^{\text{th}}$ percentile.

4.5 Volume Tracking

Volume Tracking (Paper III) extends particle tracing, which displays the motion of discrete points as they move with a fluid, to displaying the motion of three-dimensional volumes.

4.5.1 Formulation

Assume that we want to track the movement of a volume described by the set of points V_0 at time t_0 over time to arrive at another time t. A volume V_0 inside the computational domain Ω at time t_0 is described by a volume function f:

$$V_0 = \{\mathbf{x} \in \Omega \mid f(\mathbf{x}) \leq C\} . \tag{4.19}$$

f	**Shape**	**Interpretation of** C
$\mathbf{n}^T\mathbf{x}$	plane with normal $\mathbf{n}$	plane position
$\sqrt{(\mathbf{x}-\mathbf{a})^T(\mathbf{x}-\mathbf{a})}$	sphere at $\mathbf{a}$	sphere radius
$\sqrt{(\mathbf{x}-\mathbf{a})^T\mathbf{A}(\mathbf{x}-\mathbf{a})}$	ellipsoid ($\mathbf{A}$ positive definite) at $\mathbf{a}$	size

Table 4.2 – Volume functions $f(\mathbf{x}) \leq C$ used for Volume Tracking, and the corresponding shape and interpretation of the constant C.

By using different functions f and varying C, volumes of different shapes and sizes can be used, as shown in Table 4.2.

Recall the definition of the flow map $\phi_{t_0}^{t_1}(\mathbf{x})$ as a function that maps the position $\mathbf{x}$ of a particle at time t_0 to its position at the time t_1. The tracked volume can then be written as

$$V(t) = \phi_{t_0}^{t_1}(V_0), \tag{4.20}$$

i.e. the volume at another time t_1 is defined as the image of V_0 under the flow map for the appropriate time interval. The evolution of the volume to time t_1 (Equation 4.20) can also be described using the volume function and flow map as

$$V(t) = \left\{\mathbf{x} \in \Omega \mid f\left(\phi_t^{t_0}(\mathbf{x})\right) \leq C\right\}, \tag{4.21}$$

i.e. the volume is defined by f at the time t_0 and the flow map is used to select points to display based on their coordinates at time t_0.

To compute the flow map ϕ for Volume Tracking, the auxiliary function ψ is introduced as

$$\psi(\mathbf{x}, t) = \phi_t^{t_0}(\mathbf{x}). \tag{4.22}$$

The function $\psi(\mathbf{x}, t)$ then describes where the particle at $\mathbf{x}$ at time t was at the time t_0. Therefore, the value of ψ is constant along particle paths (trajectories) in the flow, i.e. *the coordinates at $t = t_0$ are advected along the flow*. Decomposing $\psi = (\psi^x, \psi^y, \psi^z)$ into its cartesian components, the advection partial differential equations (PDE)

$$\begin{aligned} \partial_t \psi^x + \mathbf{v} \cdot \nabla \psi^x &= 0 \\ \partial_t \psi^y + \mathbf{v} \cdot \nabla \psi^y &= 0 \\ \partial_t \psi^z + \mathbf{v} \cdot \nabla \psi^z &= 0 \end{aligned} \tag{4.23}$$

hold for all $\mathbf{x} \in \Omega$, where $\mathbf{v}$ is the velocity field of the flow under study.

The initial conditions at $t = t_0$ are straightforward:

$$\begin{aligned}\psi^x(\mathbf{x}, t_0) &= x \\ \psi^y(\mathbf{x}, t_0) &= y \\ \psi^z(\mathbf{x}, t_0) &= z.\end{aligned} \tag{4.24}$$

Additionally, boundary conditions to Equation 4.23 are needed to ensure a unique solution, as particles that come into the domain must be assigned some origin. We choose to define that a particle coming from outside the domain originates at the boundary, i.e. to let

$$\begin{aligned}\psi^x(\mathbf{x}, t) &= x \\ \psi^y(\mathbf{x}, t) &= y \\ \psi^z(\mathbf{x}, t) &= z\end{aligned} \tag{4.25}$$

at the parts of the boundary $\partial\Omega$ where inflow occurs.

4.5.2 Numerical implementation

Equations 4.23–4.25 consist of three non-coupled advection partial differential equations (PDEs). A second-order finite volume scheme[138,139] is used, as provided in the freely available software package CLAWPACK 4.3.[140] The included advection module was used with full transverse propagation of increment and correction waves (method(3) = 22) and the monotonized centered (MC) limiter (mthlim = 4). Adaptive step-size control was turned on (method(1) = 1) with a target Courant-Friedrichs-Lewy (CFL) number of 0.95 (cflv(2) = 0.95).

When applying the numerical method to PC-MRI data, the domain was divided into cells identical to the measured voxels. The measured velocities represent voxel averages, but the numerical method described above requires the velocity evaluated at voxel interfaces. Therefore, the voxel interface velocity was taken as the average of the two adjacent voxel velocities. The measured velocities were supplied as variable coefficients in the advection solver.

Initial values (Equation 4.24) were set to the appropriate coordinate component at the cell center before the computation started. Boundary conditions (Equation 4.25) were enforced by using two extra cells (ghost cells) around the boundary (mbc = 2). Their values were set to their center coordinate at each timestep.

In Paper III, the described PDE method was used to compute the flow map, and Ensight (CEI, USA) was used to compute particle traces for comparison, generate isosurfaces from the flow maps and generate animations. In Paper V, the flow map was computed using the particle tracing methods described in Section 4.3.

Chapter 5

Results and Discussion

5.1 Accuracy and validation

5.1.1 Stroke volumes: 4D vs 2D PC-MR

The results of the validation of stroke volumes in 4D PC-MR compared to 2D PC-MR (Paper I) are presented in Figures 5.1 and 5.2 and summarized in Table 5.1. For the SENSE acquisitions, the bias for 4D PC-MR compared to 2D PC-MR was lower for 3T compared to 1.5T, although the difference was not significant ($p = 0.46$). Peak flow rates were underestimated by 4D PC-MR compared to 2D PC-MR, for both SENSE and k-t BLAST accelerations (Table 5.1). Acquisition time for k-t BLAST was shorter than for SENSE (10.8 ± 0.7 vs 22.5 ± 0.3 min).

Overall, our results are in line with previous studies comparing SV in 4D PC-MR to 2D PC-MR, at 1.5T,[141–143] and extend them with data at 3T. Westenberg et al. used a more advanced post-processing including retrospective valve tracking for accurate quantification of valvular regurgiation, and notably acheived higher accuracy using 4D compared to 2D PC-MR[144] and fair accuracy in patients with corrected Tetralogy of Fallot.[145]

The underestimation of SV and reduced peak flows seen in our k-t BLAST data are in line with previous results by Marshall,[146] who simulated the k-t BLAST undersampling and reconstruction process and found a temporal smoothing and underestimation of peak flows. Furthermore, Stadlbauer et al. investigated the use of k-t BLAST in aortic flows compared to ultrasound, and found that higher acceleration factors gave larger errors.[147]

In summary, 4D PC-MR accelerated using SENSE gives accurate SV measurements, especially at 3T. However, k-t BLAST with acceleration factor 5 gives too large bias to be useful for quantitative purposes.

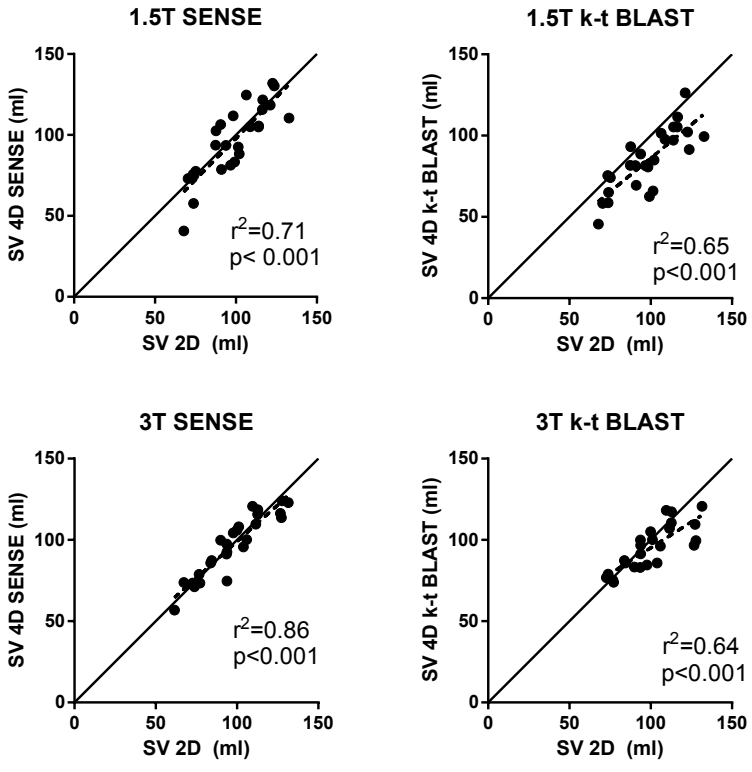

Figure 5.1 – Stroke volumes using 4D PC-MR accelerated by SENSE and k-t BLAST at 1.5T and 3T. See also Figure 5.2 for Bland-Altman plot. Image reprinted from published version of Paper I with permission.

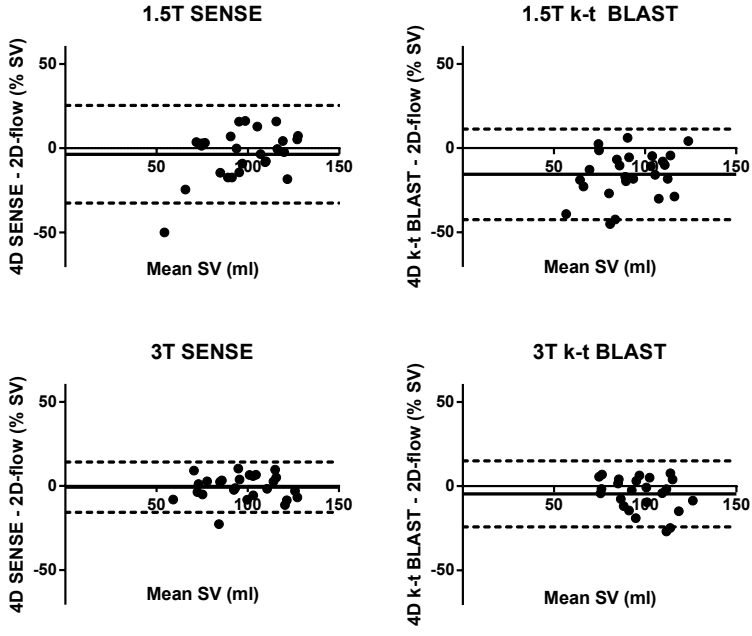

Figure 5.2 – Stroke volumes using 4D PC-MR accelerated by SENSE and k-t BLAST at 1.5T and 3T: Bland-Altman plots. See also Figure 5.1 for correlation plots and Table 5.1 for bias values. Image reused from published version of Paper I with permission.

Scanner	Sequence	R^2	SV bias	Peak flow (ml/s)
1.5T	2D PC-MR	-	-	439 ± 86
3T	2D PC-MR	-	-	448 ± 83
1.5T	4D SENSE=2	0.71	$-3.6 \pm 14.8\%$	$402 \pm 86^{**}$
3T	4D SENSE=2	0.86	$-0.7 \pm 7.6\%$	$421 \pm 75^{**}$
1.5T	4D k-t BLAST=5	0.65	$-15.6 \pm 13.7\%$	$353 \pm 77^{***}$
3T	4D k-t BLAST=5	0.64	$-4.6 \pm 10.0\%$	$389 \pm 68^{***}$

Table 5.1 – Stroke volumes and peak flows using 4D PC-MR accelerated by SENSE and k-t BLAST at 1.5T and 3T: Summary of results in Figures 5.1 and 5.2.
** and ***: $p < 0.01$ and $p < 0.001$ difference in peak flow compared to 2D PC-MR respectively.

5.1.2 Vortex ring phantom: stability

Measurements using PIV, PLIF and 4D PC-MR were feasible using all five proposed pump programs. Peak nozzle velocities ranged from 19 to 40 cm/s, with corresponding Reynolds numbers (Re) from 5200 to 8900.

For assessment of the stability and repeatability of the flow produced in the phantom setup, Figure 5.3 shows a detailed comparison of velocities measured on day 1 and day 2, for pump program E at $t = 400$ ms. Excellent agreement was found, e.g. $R^2 = 0.96$ and bias -0.06 ± 0.70 cm/s for the up/down direction. Figure 5.4, panels A-E, shows a summary of results from all five pump programs and at all timeframes between 0 and 600 ms. The difference in velocity shows low variation between pump program and timeframes, in both the up/down and left/right directions. Furthermore, Figure 5.4, panel F, shows a comparison of peak velocities in the measurement area at $t = 400$ ms for all five pump programs. Figure 5.5 shows the pump stroke volume measured using 2D PC-MR before and after each 4D PC-MR measurement. A strong correlation and a small bias was found ($R^2 = 1.00, -0.3 \pm 2.1$ %).

The results presented in Figures 5.3–5.5 show that the flow phantom produces a stable, well-defined flow field, both within a single experiment and between days. The proposed vortex ring setup can therefore be used for validation of 4D PC-MR measurements.

Accelerated 4D PC-MR sequences, e.g. using k-t BLAST and k-t SENSE[131] (Paper I), spiral readouts,[68] random undersampling,[148] and k-t PCA,[149] are of great interest to reduce scan times, and thereby enable a broader clinical use of 4D PC-MR. The proposed vortex ring flow phantom provides a suitable experiment for evaluating velocity errors, such as temporal and spatial smoothing, introduced by the acceleration.

Knobloch et al.[70] validated 4D PC-MR velocity and turbulence measurements against particle tracking velocimetry (PTV) and showed excellent agreement. However, due to differences between the MR and PTV setups, their evaluation required a *post hoc* correction factor applied to the PTV measurements. The presented vortex ring flow phantom can operate with the same tubing and positions in both the MR and PIV/PLIF settings, enabling a direct validation of velocity measurements.

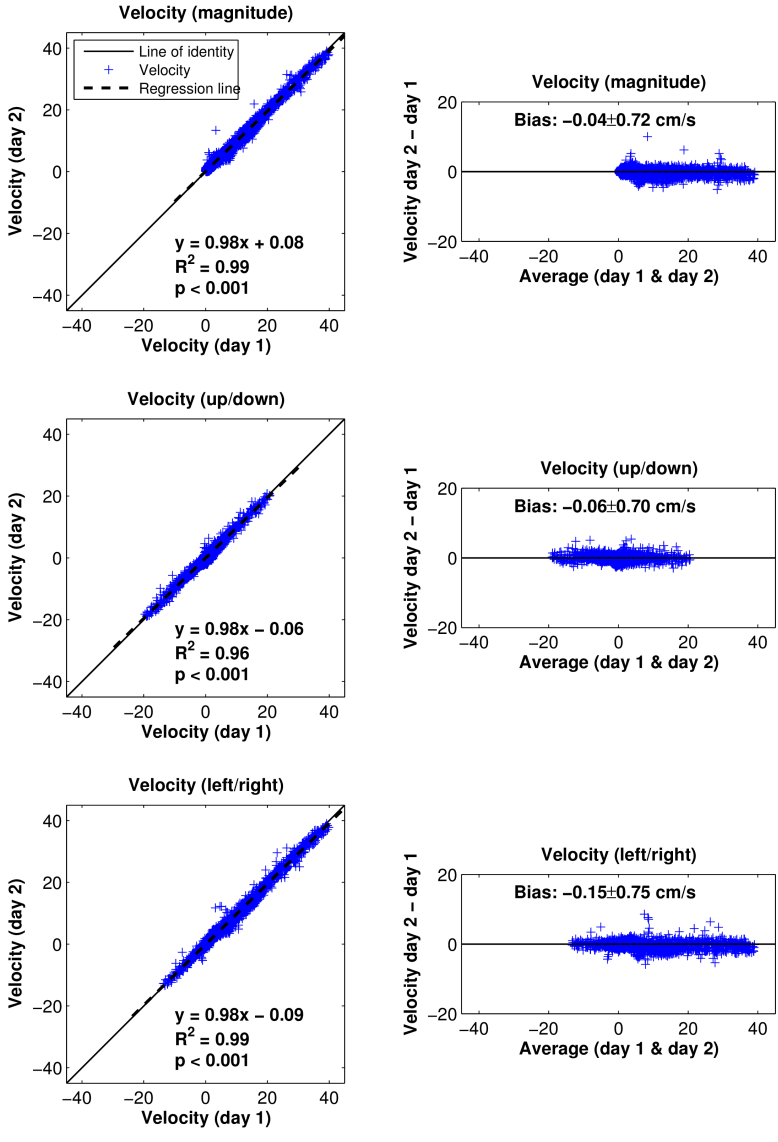

Figure 5.3 – Detailed comparison of PIV velocity measurements in the vortex ring flow phantom on two consecutive days, for velocity program E (VFR = 3.0) at $t = 400$ ms. Excellent agreement and a small bias was found.

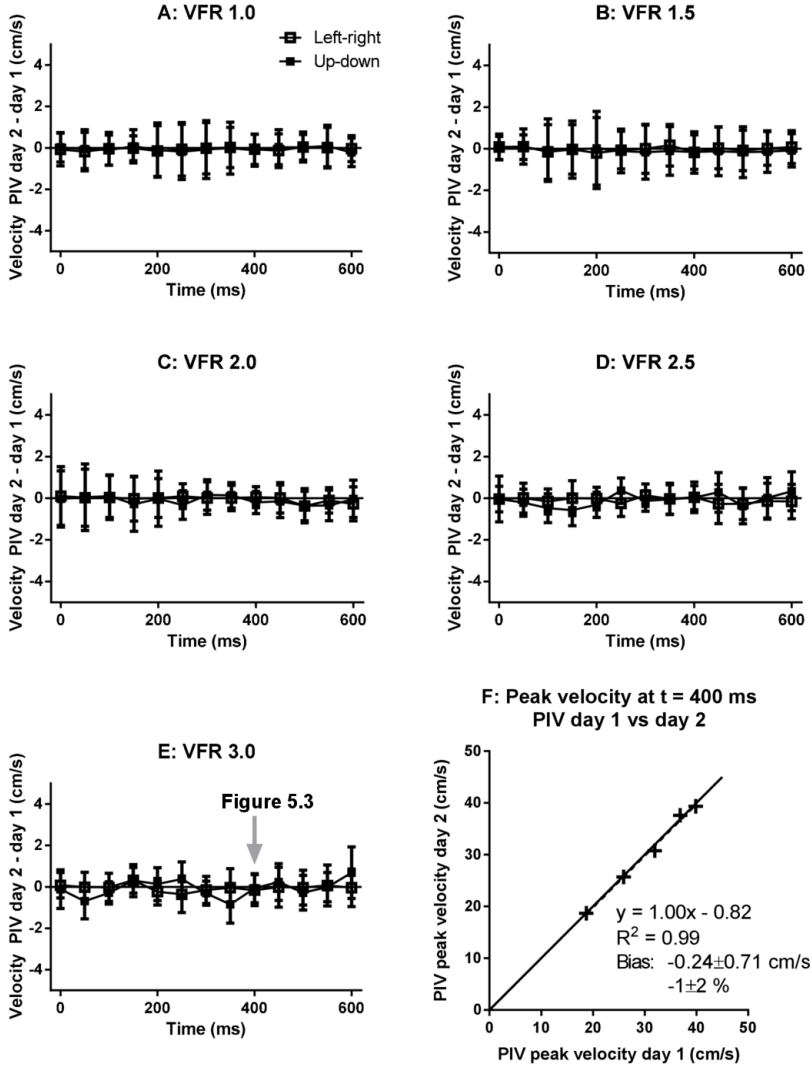

Figure 5.4 – Comparison of PIV velocity measurement in the vortex ring flow phantom on two consecutive days for all velocity programs (panels A-E) (pixel-wise mean±SD). A small variability was found. Panel F shows peak velocity in the measurement area at $t = 400$ ms. A strong correlation and low bias was found.

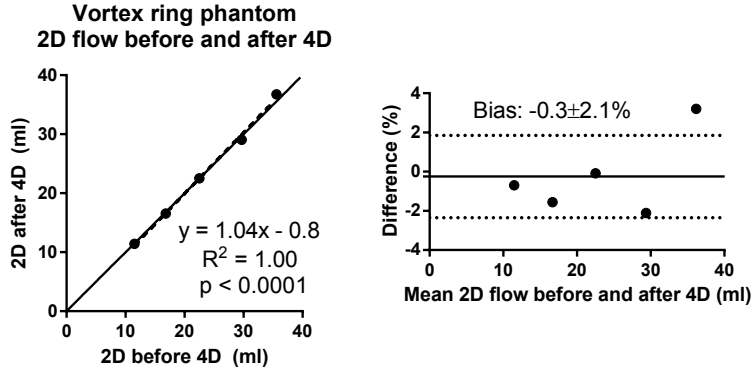

Figure 5.5 – Comparison of 2D PC-MR stroke volumes in the vortex ring flow phantom, before and after the 4D PC-MR measurements (Paper II). A strong correlation and small bias were found, reinforcing the stability of the flow phantom setup.

5.1.3 Vortex ring phantom: validation of 4D PC-MR velocities against PIV

A visual comparison of 4D PC-MR and PIV measurements in the vortex ring phantom is shown in Figure 5.6. Visually, the velocity measurements show a slightly lower peak velocity in the 4D PC-MR data compared to PIV.

Figure 5.7 shows a detailed, pixel-by-pixel comparison of velocities measured using 4D PC-MR and PIV for pump program E, at $t = 400$ ms. Overall, a strong correlation and small bias was found, e.g. $R^2 = 0.95$, bias 0.17 ± 2.31 cm/s for velocity magnitude (see Figure 5.7 for details). However, a trend towards underestimation of velocities in 4D PC-MR compared to PIV is seen for peak velocities.

Figure 5.8, panels A-E shows the comparison between 4D PC-MR and PIV velocities for all pump programs and all acquired time phases. A low bias and standard deviation was found, both for the up/down and left/right velocity components. Figure 5.8F shows a comparison of peak velocities at $t = 400$ ms for pump program E between 4D PC-MR and PIV. A strong correlation ($R^2 = 0.89$) and an underestimation in the range $8-25$ % was found (-14 ± 7 %).

In summary, good accuracy was found for 4D PC-MR velocity measurements compared to PIV, although with an underestimation of peak velocities. The underestimation of peak velocities is in line with previous results that 4D PC-MR underestimates peak flow rates compared to ultrasound[150] and 2D PC-MR (Paper I and Section 5.1.1).

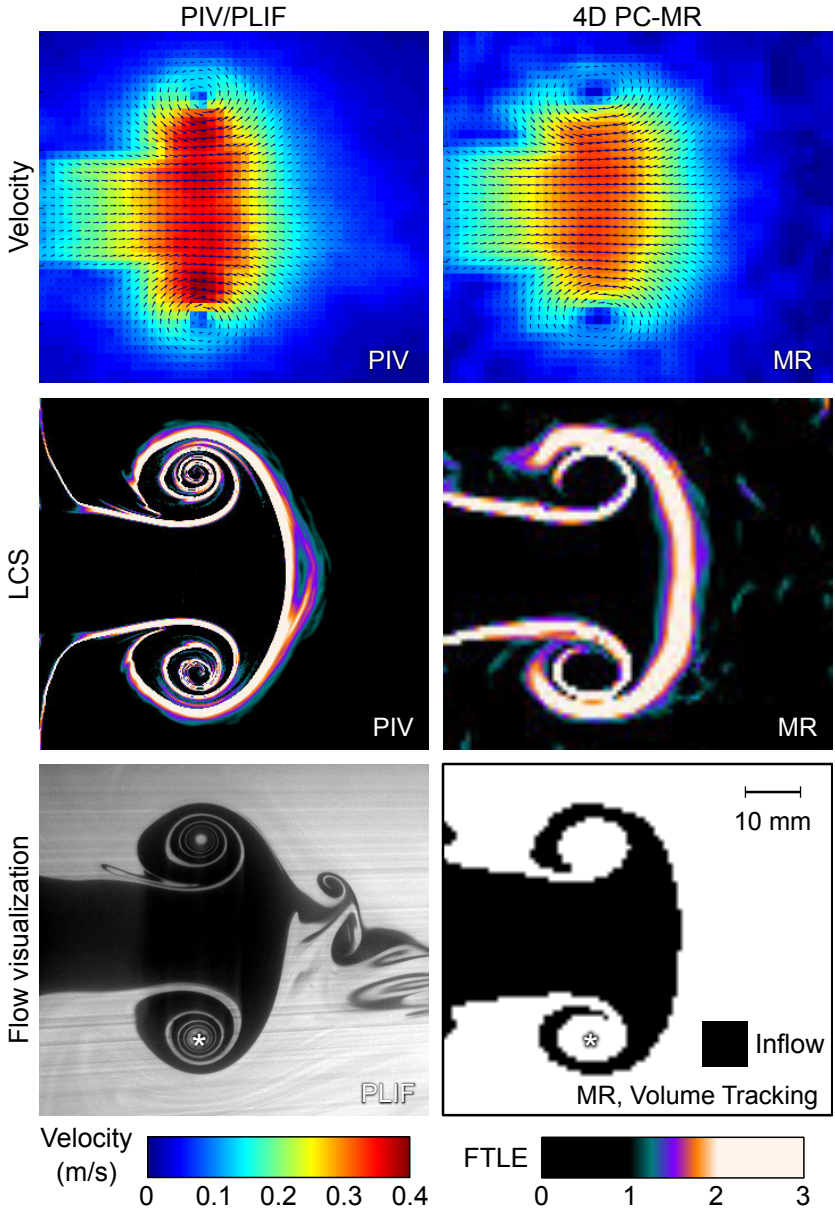

Figure 5.6 – Visual presentation PIV and PLIF (left) and 4D PC-MR (right) measurements for velocity program D ($VFR = 2.5$) at $t = 400$ ms. The asterisk (*) denotes the vortex ring core, where a distinct 'winding' is seen in the PLIF image, but not in the 4D PC-MR Volume Tracking visualization.

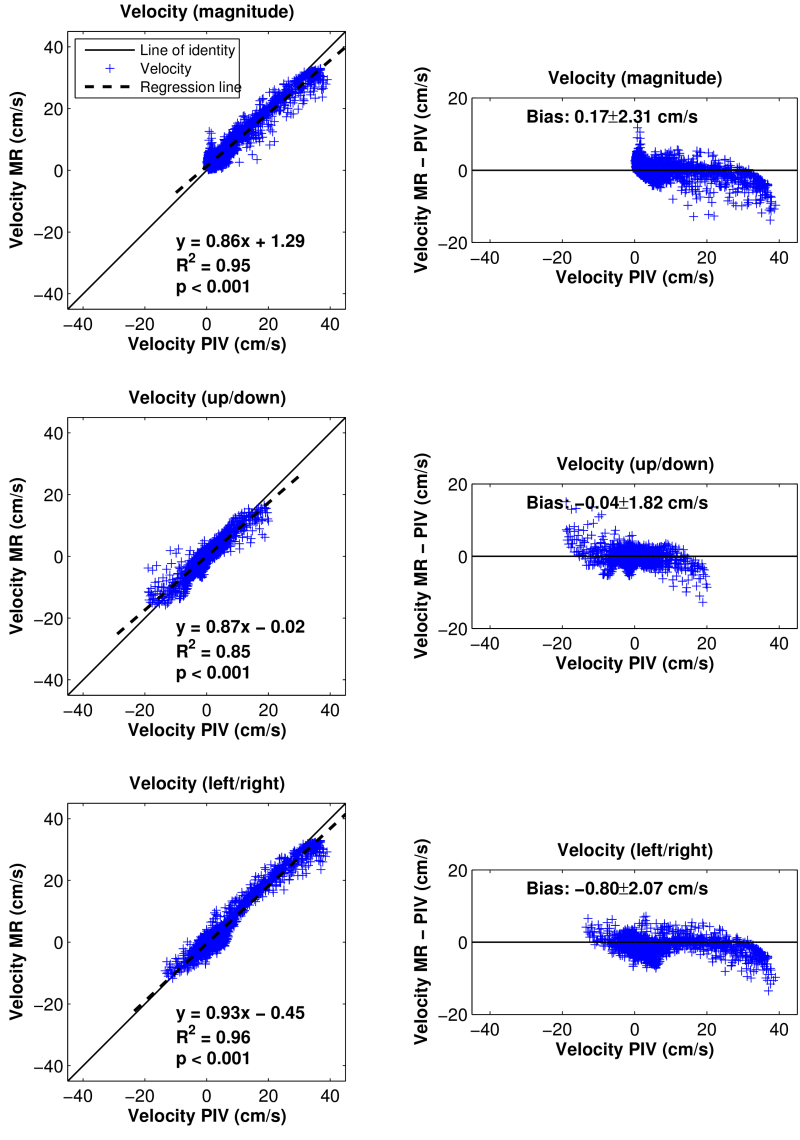

Figure 5.7 – Validation of 4D PC-MR velocities against PIV. Details for velocity program E (VFR = 3.0) at $t = 400$ ms are shown. Good agreement was found, but peak velocities were underestimated using 4D PC-MR (see also Figure 5.8, panel F).

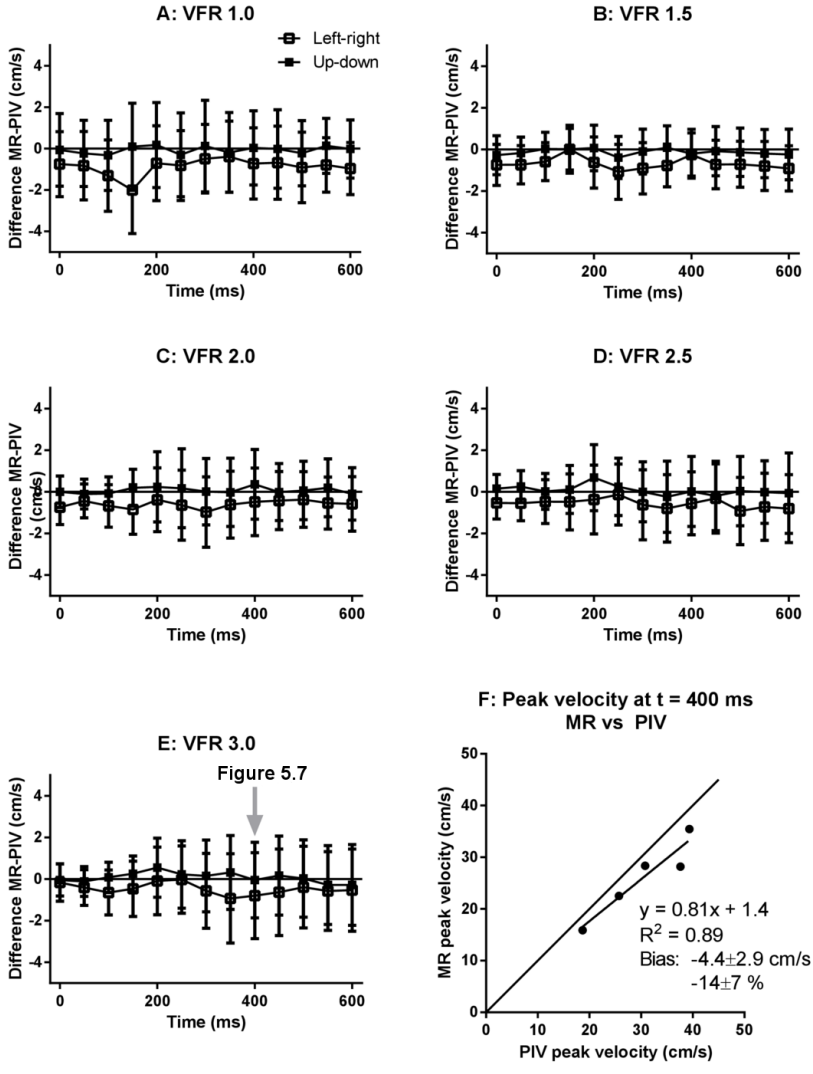

Figure 5.8 – Validation of 4D PC-MR velocities against PIV. Panels A-E: difference in pixel-wise velocity for velocity programs A-E vs time. Details for program E at $t = 400$ ms are shown in Figure 5.7. Panel F: Comparison of peak velocities in the PIV measurement area at $t = 400$ ms. 4D PC-MR underestimates peak velocities compared to PIV.

5.1.4 Validation of quantitative vortex ring parameters

Figure 5.6 shows a visual comparison of 4D PC-MR and PLIF measurements of vortex ring formation. Figure 5.9 shows quantitative results of the comparison of quantitative vortex ring parameters (vortex ring volume, VV and mixing ratio, MXR) between 4D PC-MR and planar laser-induced flourescence (PLIF) in the phantom setup.

For VV, the top row of Figure 5.9 shows a strong correlation ($R^2 = 0.99$) and low bias (2.4 ± 1.5 ml), although a small overestimation is present in 4D PC-MR compared to PLIF. For MXR, the bottom row of Figure 5.9 shows a strong *negative* correlation ($R^2 = 0.82$) between 4D PC-MR, and PLIF, and a large bias (8 ± 21 %).

Changing the temporal and spatial resolution of the computations for Lagrangian Coherent Structures and Volume Tracking (using particle tracing) from 5 ms and 0.8 mm to 1 ms and 0.2 mm gave a minor difference in VV, VV_{inflow} and $VV_{mix\text{-}in}$ (41.66, 27.14 and 14.52 ml vs 41.67, 27.53 and 14.14 ml respectively, evaluated in program E at $t =$ 400 ms).

The strong correlation and low bias found for VV further reinforces and validates the in vivo measurements of vortex ring volume in Papers IV and V. The small overestimation may be due to differences in trigger timing and manual delineations between 4D PC-MR and PLIF, and the assumption of axisymmetry used in analysis of PLIF images.

The poor accuracy in MXR for 4D PC-MR compared to PLIF may have several causes. The small difference shown in VV, VV_{inflow} and $VV_{mix\text{-}in}$ when increasing temoporal and spatial resolution in LCS and Volume Tracking computations suggests that the poor agreement is not due to computational issues. Comparing the flow visualizations with PLIF and 4D PC-MR (Figure 5.6, bottom row), the PLIF image displays a 'winding' of the vortex ring core which is not seen in the 4D PC-MR Volume Tracking image.

Figure 5.10 show PLIF and MR flow visualizations for all pump programs. Programs C,D and E display a similar pattern, with a lesser winding in MR compared to PLIF, leading to an overestimation of MXR using MR. In programs A and B, the PLIF and MR images look qualitatively similar, but the MR images show a smaller amount of mixed-in fluid, leading to an underestimation of MXR.

Further error sources that may contribute to the discrepancy include spatial and temporal resolution of the 4D PC-MR sequence and post-processing steps such as background phase correction, threshold selection and manual delineations. Furthermore, a potential mismatch in fluid dynamic parameters, such as the Reynolds number and relation between nozzle velocity and vortex ring core rotation, may provide a more complex flow field in the phantom setup compared to in vivo. Further work is needed to identify and alleviate error sources.

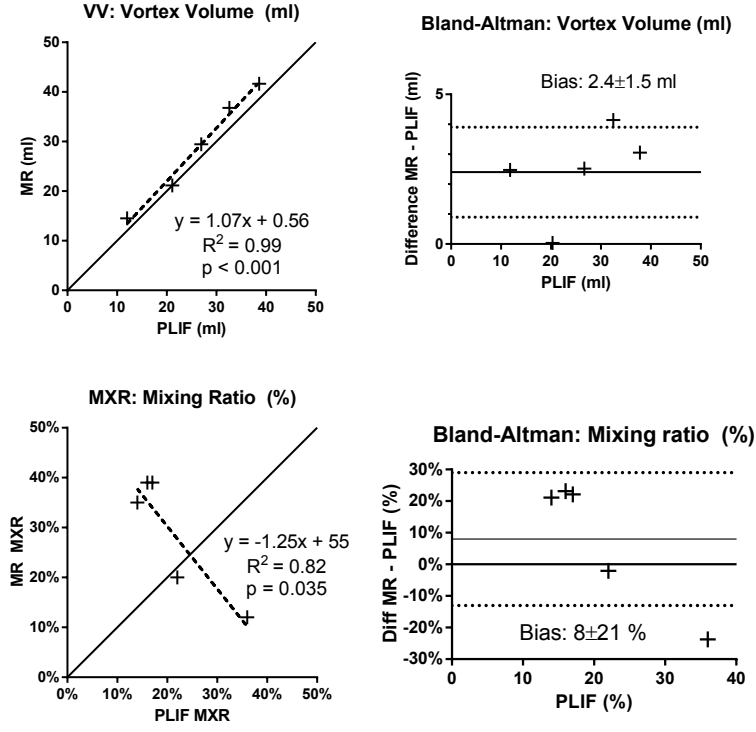

Figure 5.9 – Validation of 4D PC-MR measurement of vortex ring volume (VV) and mixing ratio (MXR) against planar laser-induced flourescence (PLIF). Good agreement was found for VV, but not for MXR.

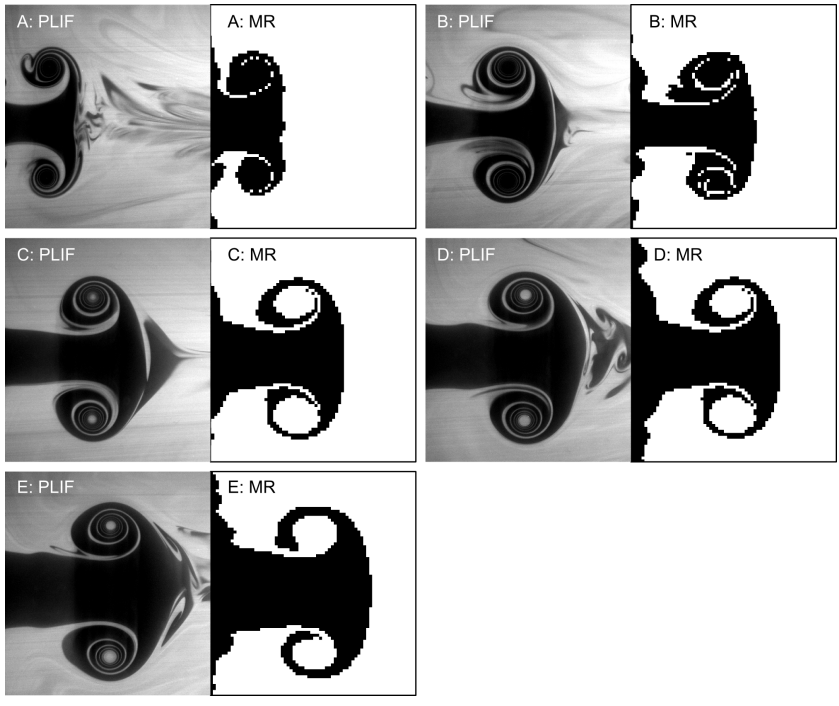

Figure 5.10 – Mixing visualizations using PLIF and 4D PC-MR for all five velocity programs (A-E) at $t = 400$ ms. For velocity programs A and B, 4D PC-MR underestimates the mixed-in volume compared to PLIF. In contrast, an overestimation of the mixed-in volume is seen for programs C-E.

5.2 In vivo vortex ring formation

5.2.1 Visual observations

The developed method for computation of Lagrangian Coherent Structures (LCS) allow generation of LCS images in any CMR viewplane and for any time point in the cardiac cycle (Paper IV). Figure 5.11 shows a visualization of vortex ring formation using Lagrangian Coherent Structures (LCS) during rapid filling of the LV in a healthy volunteer. LCS indicative of vortex ring formation appeared in the 3ch and 2ch views in this volunteer, but not in the 4ch view. The LCS pattern occupies a majority of the volume of the LV. Figure 5.12 shows a similar visualization in a patient with dilated cardiomyopathy (DCM). As in the healthy volunteer, LCS indicative of vortex ring formation appeared in the 3ch and 2ch views, but not in the 4ch view.

Table 5.2 summarizes the views in which vortex ring LCS were visible in all subjects in Paper IV. Vortex ring LCS were observed in the 3ch view in all subjects, but were less common in the 2ch and 4ch views. In both the healthy volunteers and the patients, the vortex ring LCS show more complexity and asymmetry compared to experiments in water tanks (Figure 5.6),[103–105] and adapt to the endocardium and papillary muscles (cf asterisks in Figures 5.11 and 5.12).

The more complex and asymmetric appearance of the vortex rings in vivo compared to water tank experiments is likely a consequence of the asymmetry of the mitral valve and of the heart as a whole.[9] The vortex ring originates from the left atrium leaflets of the mitral valve, whose asymmetry is likely a major cause for the asymmetry of the vortex ring. This is consistent with theory and experiments which show that the vorticity of the vortex ring is generated on the inside surface of the nozzle generating the vortex ring.[110] Furthermore, the asymmetry of the mitral valve may explain the consistent presence of vortex ring LCS in the 3ch view, which is planned in a position orthogonal to the mitral valve leaflets.[35,151]

The additional complexity of the in vivo vortex rings compared to water tank experiments is likely due to the proximity of the vortex ring to the endocardium and papillary muscles. In contrast, previous experiments on vortex rings were performed in water tanks with little or no influence from the tank boundaries. These differences may be important when comparing idealized experiments in water tanks and in vivo flow measurements.

5.2.2 Quantitative results

Figure 5.13 shows the vortex ring volume (VV) and VV in relation to the LV volume at diastasis (VV/DV) and patients with heart failure and dilated LV (Papers IV and V). VV did not differ between the healthy volunteers and the patients ($p = 0.92$), but VV/DV was significantly different (51 ± 7 % vs 26 ± 5 %, $p < 0.0001$).

Figure 5.14 shows results of analysis of mixing ratio (MXR) and the fraction of the end-systolic volume (ESV) pulled into the vortex ring during rapid filling ($VV_{\text{mix-in}}/ESV$).

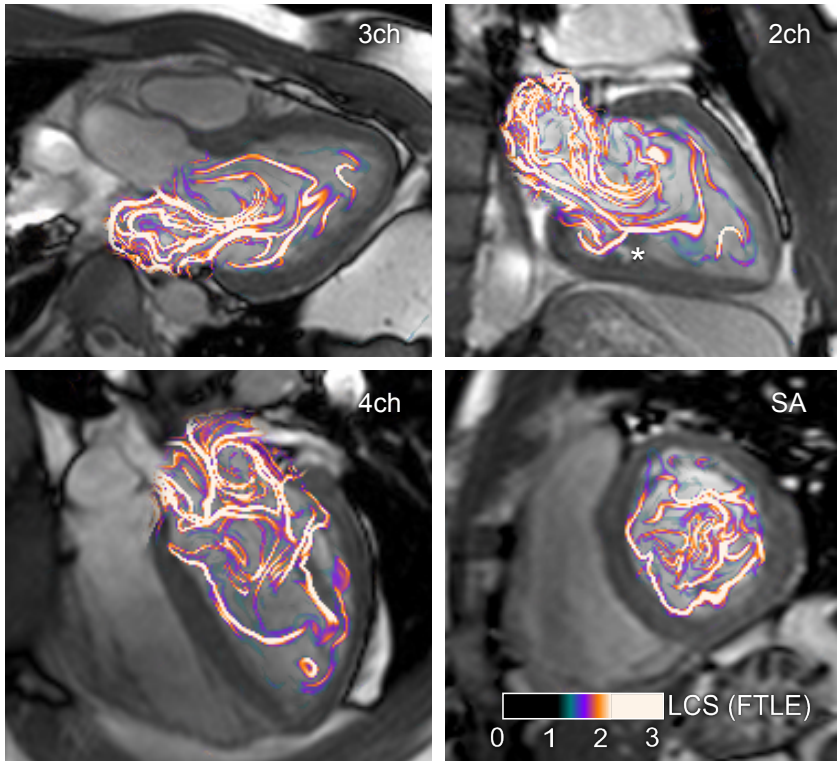

Figure 5.11 – Lagrangian Coherent Structures (LCS) during rapid filling of the left ventricle in a selected healthy volunteer (Paper IV). In this volunteer, LCS indicative of vortex ring formation appeared in the 3ch and 2ch views, but not in the 4ch view. The asterisk (*) in the 2ch image shows adaptation of the LCS to the papillary muscles.

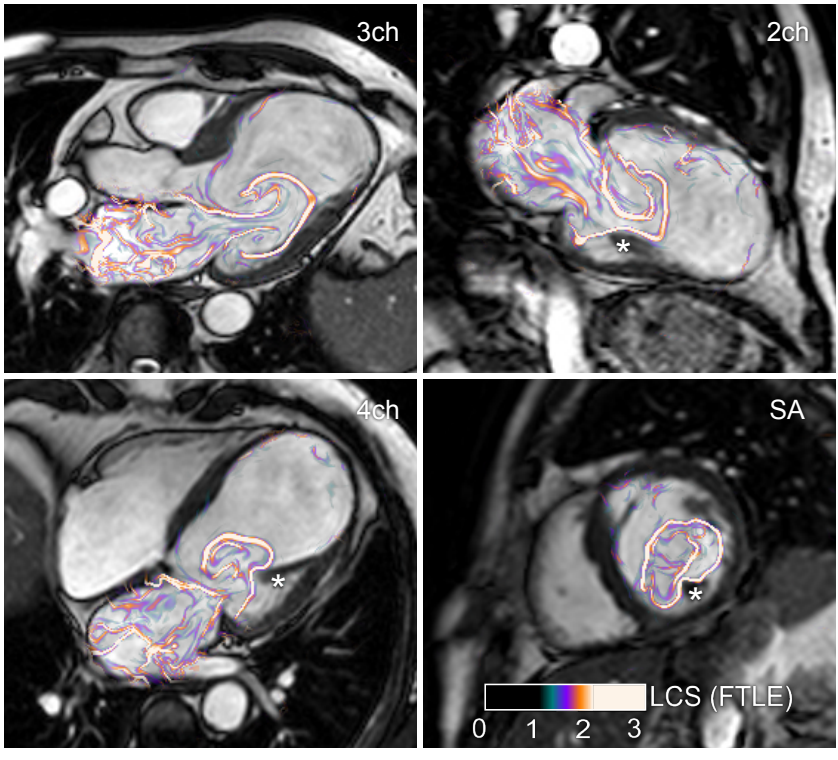

Figure 5.12 – Lagrangian Coherent Structures (LCS) during rapid filling of the left ventricle in a selected patient (Paper IV). In this patient, LCS indicative of vortex ring formation appeared in the 3ch and 2ch views, but not in the 4ch view. The asterisks (*) in the 2ch, 4ch and short-axis (SA) views show adaptation of the LCS to papillary muscles.

Subject	2ch	3ch	4ch
1	n/a	x	x
2	x	x	
3	x	x	
4	x	x	
5	x	x	
6		x	
7	x	x	
8		x	
9		x	
P1	x	x	
P2		x	x
P3	x	x	
P4		x	
Total:	7/13	13/13	2/13
	54%	100%	15%

Table 5.2 – Visual assessment of vortex ring LCS in different viewplanes (Paper IV). Each 'x' in the table indicates that LCS indicating vortex ring formation was seen in the corresponding subject and viewplane. Subjects 1-9: Healthy volunteers, P1-P4: Patients with dilated left ventricles.
n/a = not available.

Group	n	VV (ml)	MXR (%)	$VV_{mix\text{-}in}/ESV$ (%)
Interobserver, healthy volunteers	15	1 ± 7	-1 ± 6	-1 ± 7
Interobserver, patients	15	2 ± 9	0 ± 1	1 ± 1
Interstudy, healthy volunteers	6	-2 ± 11	-3 ± 10	-3 ± 10

Table 5.3 – Interobserver (with respect to LCS delineations) and interstudy variability (1.5T and 3T scans on the same day) for the quantitative measures used in Paper IV and Paper V.

MXR was lower in healthy volunteers compared to patients (19 ± 7 % vs 33 ± 7 %, $p < 0.001$), while $VV_{mix\text{-}in}/ESV$ was higher in healthy volunteers compared to patients (22 ± 11 % vs 11 ± 5 %, $p < 0.0001$).

Interobserver and interstudy variability for VV, MXR and $VV_{mix\text{-}in}/ESV$ are given in Table 5.3. Fair variability with a low mean bias was found for all three measures.

In the healthy volunteers, the vortex ring occupies approximately half of the LV blood volume and the vortex ring is located close to the endocardium. This reveals that a large part of the LV blood volume is involved in vortex ring formation. In contrast, the vortex ring accounted for only 21% of the LV blood volume in the patients. The motion of blood and mixing in the vortex ring may contribute to reducing the likelihood of thrombus formation. A higher risk of thrombus formation has been observed in patients with low EF,[152] which may be connected to flow conditions with a small vortex ring in relation to the LV volume.

5.2.3 Phantom results

Figure 5.15 shows a graph of MXR measured using PLIF vs vortex formation ratio (VFR, stroke ratio L/D) in the phantom experiments (Paper II), together with results from previous studies.[104,108] The present phantom results show a decreasing MXR with increasing VFR, which is in line with previous studies. However, the exact MXR values differ somewhat, both between the previous studies themselves and between the previous studies and our results, which may be due to differences in inflow velocity profiles and other flow conditions.[104]

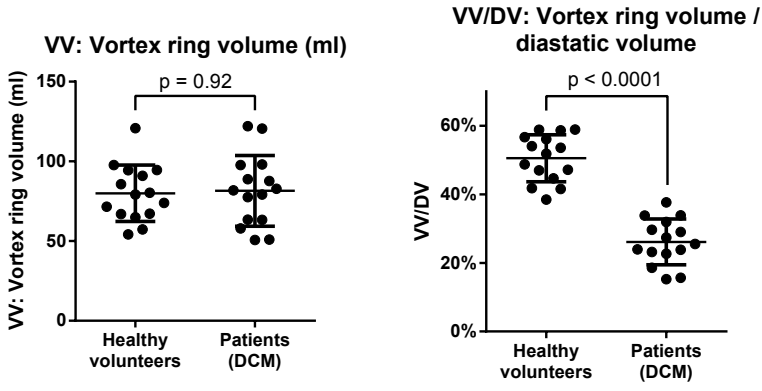

Figure 5.13 – Vortex ring volume (VV, left) and VV in relation to the diastatic volume (DV), VV/DV (right), from Papers IV and V. For VV, no difference was found between patients and volunteers. However, a large difference was found in VV/DV. (Papers IV and V)

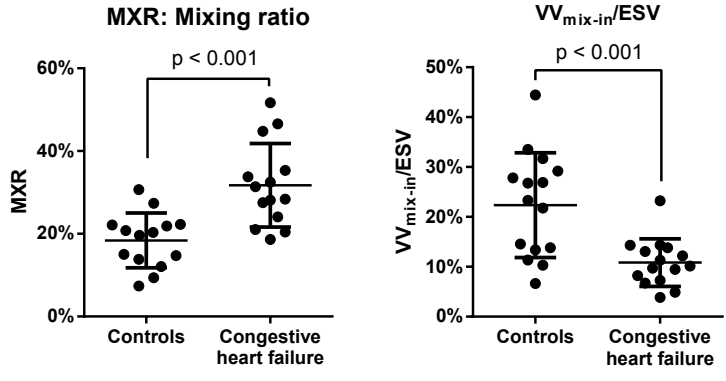

Figure 5.14 – Comparison of mixing ratio (MXR) and $VV_{mix\text{-}in}$/ESV, the fraction of the end-systolic volume mixed into the vortex ring during early rapid filling, between healthy volunteers and patients with congestive heart failure. (Paper V)

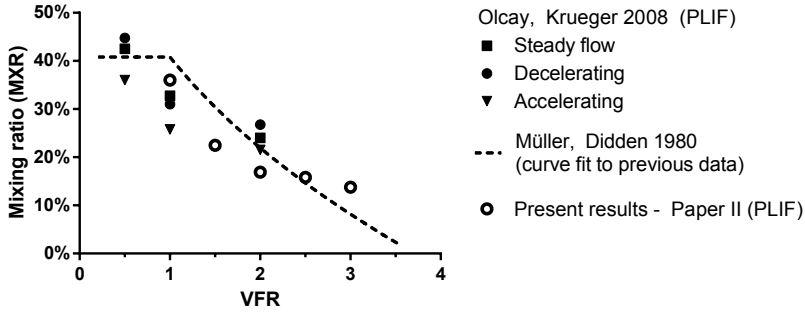

Figure 5.15 – Mixing ratio (MXR) results by PLIF from Paper II in comparison to previous results by Olcay and Krueger[104] and Müller and Didden,[108] who quantified MXR by analyzing previously published data.[106,109,110] In the previous results, MXR decreases with increasing VFR. This finding is confirmed by the present results (Paper II, open circles).

5.3 Visualization

5.3.1 Particle tracing in 4D PC-MR accelerated with SENSE and k-t BLAST

Examples of 4D PC-MR flow visualizations using particle tracing from SENSE and k-t BLAST at 1.5T and 3T scans in one subject (Paper I) are shown in Figures 5.16 and 5.17. Visually, no clear difference can be seen in this subject. The mean quality score at 1.5T was somewhat worse than at 3T (0.8 ± 0.4 vs 0.6 ± 0.2), but the difference was not statistically significant ($p = 0.09$). There was no difference in mean quality score between SENSE and k-t BLAST acquisitions (0.7 ± 0.2 vs 0.7 ± 0.4, $p = 0.85$).

The lack of a difference in visualizations between SENSE and k-t BLAST acqusitions shows that the faster k-t BLAST acquisition may be used when the main goal is to visualize flow. This may be especially important in patients who do not tolerate long scan times. However, k-t BLAST is not accurate enough for quantitative purposes (Section 5.1.1).

5.3.2 Volume Tracking

The new method for visualization of intracardiac blood flow, Volume Tracking (Paper III), was developed and implemented as a plugin for Segment.[133] Ensight 9.2 was used for display of the resulting visualizations.

Figure 5.18 shows particle tracing and Volume Tracking visualizations of diastolic filling of the LV in a healthy volunteer. Particle tracing shows a pattern of swirling flow,

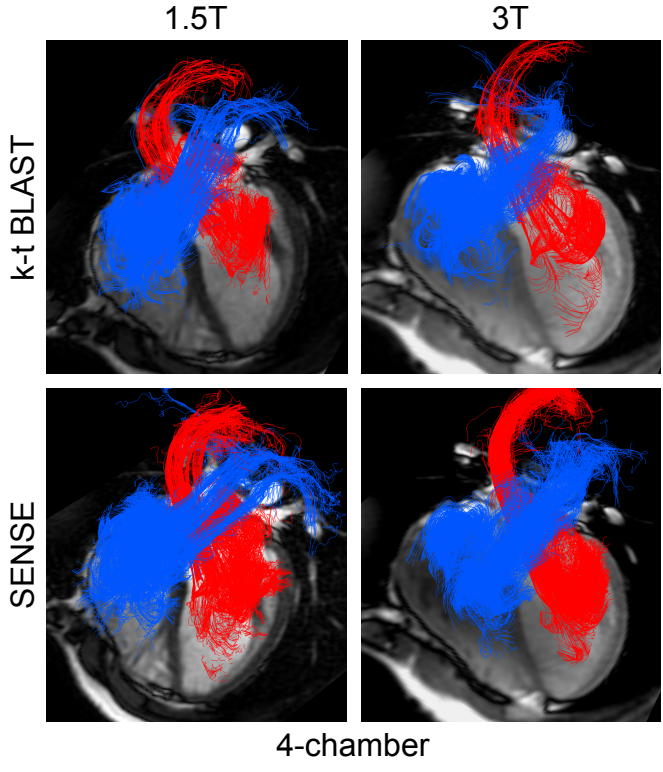

Figure 5.16 – Long-axis 4-chamber view of particle tracing (pathline) visualization of intracardiac blood flow using SENSE and k-t BLAST acceleration at 1.5T and 3T. Red: particles released in the LV and LA, blue: particles released in the RV and RA. Only a small amount of particles exhibit a non-physiological flow, which was interpreted as good image quality. No major differences were seen between 1.5T or 3T, nor between k-t BLAST or SENSE.

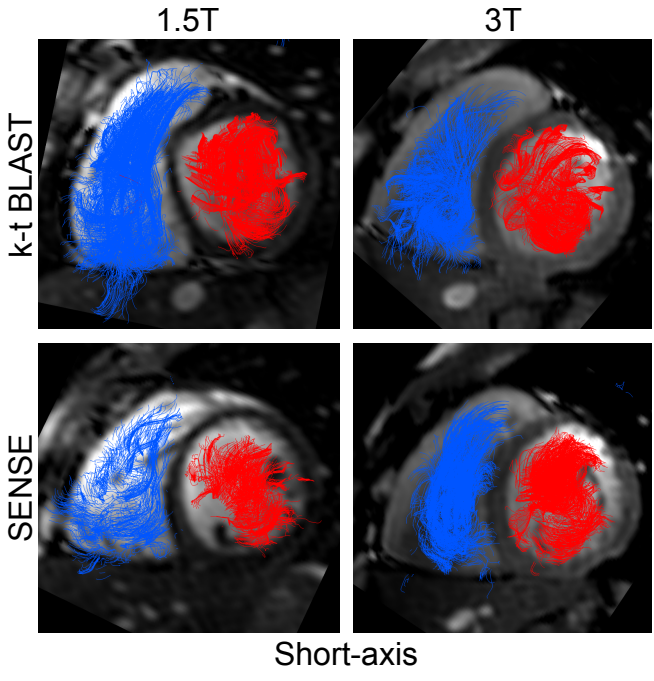

Figure 5.17 – Short-axis view of particle tracing (pathline) visualization of intracardiac blood flow using SENSE and k-t BLAST acceleration at 1.5T and 3T. Red: particles released in the LV and LA, blue: particles released in the RV and RA. Only a small amount of particles exhibit a non-physiological flow, which was interpreted as good image quality. No major differences were seen between 1.5T or 3T, nor between k-t BLAST or SENSE.

while Volume Tracking, in contrast, shows the boundary between the inflowing blood and blood that was already in the ventricle.

Figure 5.19 shows particle tracing and Volume Tracking visualizations of diastolic filling in the LV of a patient with dilated cardiomyopathy. The flow in this patient is distinctly different from the flow in the healthy volunteer in Figure 5.18.

Figure 5.20 shows diastolic inflow in the right ventricle (RV) of a healthy volunteer. Here, the particle trace visualization shows how particles flow from the right atrium (RA) into the RV. Volume Tracking visualization shows how the blood in the RA moves into the RV and disperses into a complex pattern, which is not easy to appreciate in the particle tracing visualization.

The validation of Volume Tracking visualizations against particle tracing resulted in a mean agreement of 90 ± 4 % at mid-diastole, and 88 ± 7 % at end-diastole.

The semi-quantitative inflow scoring had high interobserver agreement (Cohen's kappa $\varkappa = 0.91$). Furthermore, in seven out of eight volunteers and in the patient, the inflowing blood did not reach the apical level by mid-diastole. At end-diastole, blood had reached the apical level in a majority of the healthy subjects (observer 1: 6 of 8, observer 2: 8 of 8). The patient with dilated cardiomyopathy had a different blood flow pattern compared to the healthy volunteers, with blood only present in segments 4,5,6 and 7 in the basal part of the LV, and the inflow did not reach the apical level.

Volume Tracking provides incremental information compared to particle tracing: 1) Volume Tracking shows the surface of the inflowing blood volume, rather than detailed particle dynamics, 2) Volume Tracking emphasizes overall motion more than particle tracing, and 3) Volume Tracking reveals a complex flow pattern in the RV, which is not visible using particle tracing. The fact that the choice of visualization method influences the impression of the flow is in line with previous studies on flow visualization mehods.[79,80] Therefore, Volume Tracking may be used to gain new understanding from 4D PC-MR blood flow measurements.

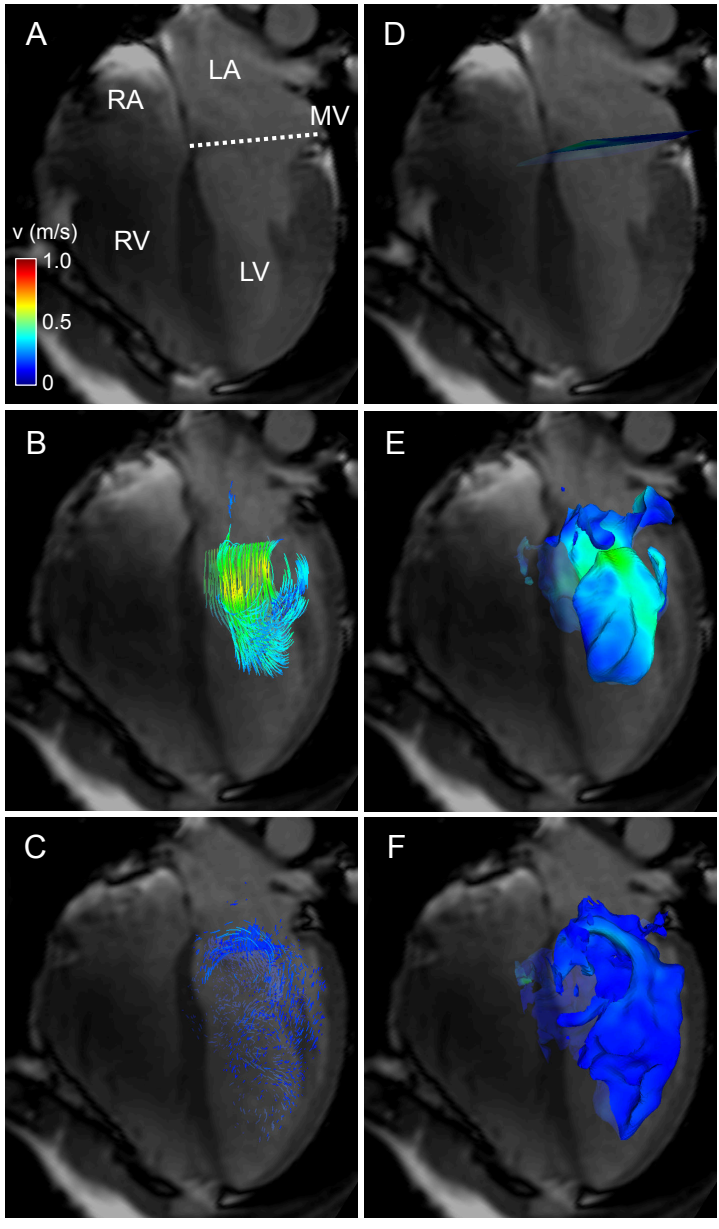

Figure 5.18 – Particle tracing (left, A-C) and Volume Tracking (right, D-F) visualizations of blood flowing into the LV during rapid filling in a healthy volunteer. Panels A and D show the start of diastole, B and E show peak rapid filling, and C and F show late diastole. *MV = mitral valve*.

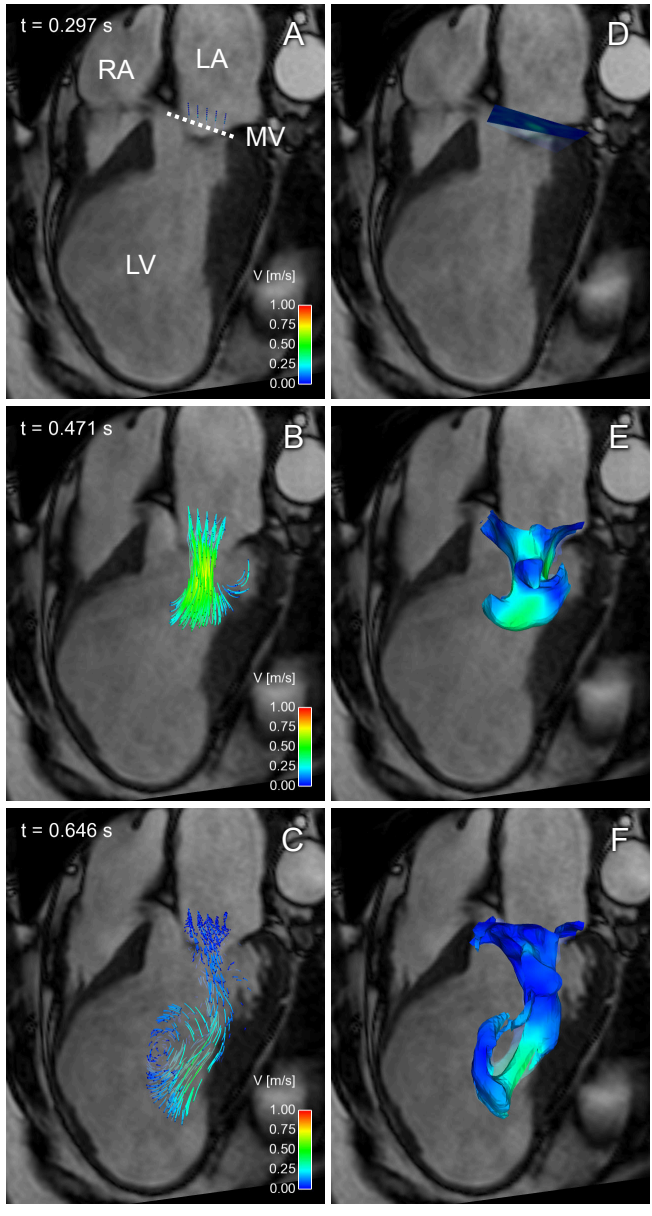

Figure 5.19 – Particle tracing (left, A-C) and Volume Tracking (right, D-F) visualizations of blood flowing into the LV during rapid filling in a patient with dilated cardiomyopathy (DCM). Panels A and D show the start of diastole, B and E show peak rapid filling, and C and F show late diastole. *MV = mitral valve*.

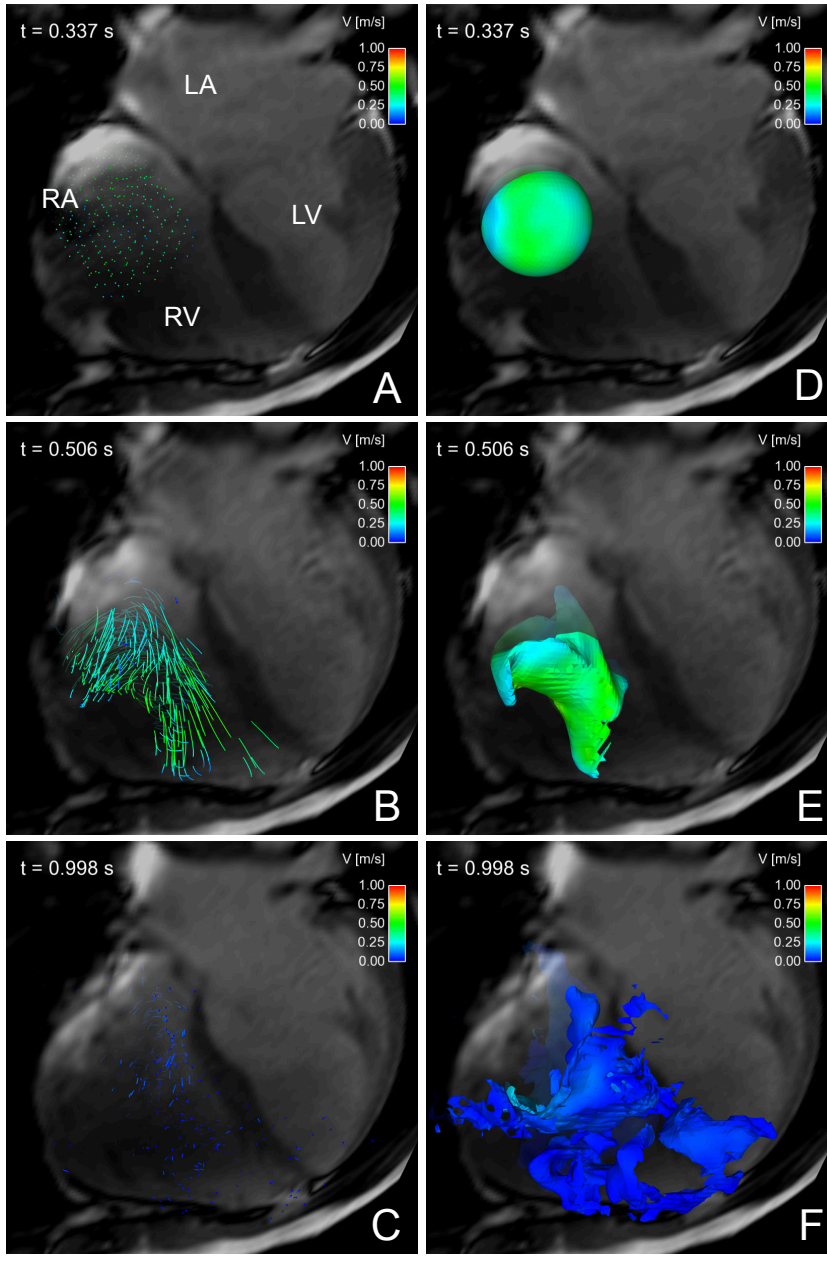

Figure 5.20 – Particle tracing (left, A-C) and Volume Tracking (right, D-F) visualizations of blood flowing into the right ventricle (RV) during diastole. Note how Volume Tracking reveals a complex flow (panel F) not readily apparent using particle tracing (panel C).

5.4 Future work

Validation of quantitative vortex ring parameters

The discrepancy in mixing ratio (MXR) between 4D PC-MR and PLIF (Paper II) shows that for the vortex rings generated in the current phantom setup, 4D PC-MR can not be used to quantify MXR. Further work will concentrate on identifying and mitigating the error sources contributing to this discrepancy, e.g. mismatch of fluid dynamical parameters between the phantom setup and in vivo flow condition, temporal and spatial resolution in the 4D PC-MR sequence, and postprocessing steps such as background correction, threshold selection and manual delineations.

Validation of accelerated 4D PC-MR sequences

Recently, several strategies for acceleration of 4D PC-MR sequences have been proposed, e.g. k-t BLAST and k-t SENSE,[146] spiral readouts,[68] random undersampling[148] and k-t PCA.[149] However, acceleration strategies may introduce artifacts and measurement errors such as temporal and spatial smoothing. The phantom setup in Paper II can be used to quantify these errors in a reliable manner.

Chapter 6

Conclusions

Accuracy and validation

- 4D PC-MR accelerated with SENSE gives accurate stroke volume measurements, and 3T compares favourably with 1.5T. However, acceleration using k-t BLAST shows a too large bias for clinical use. – *Paper I*

- The flow in the developed vortex ring flow phantom is highly stable, making it suitable as a validation experiment for 4D PC-MR. – *Paper II*

- Velocity measurements using 4D PC-MR agree well with particle imaging velocimetry (PIV) in a phantom setup, but peak velocities are underestimated by 8-25% using 4D PC-MR. – *Paper II*

- Vortex ring volume (VV) can be reliably quantified using 4D PC-MR, while the vortex ring mixing ratio (MXR) shows poor agreement with planar laser-induced flourescence (PLIF). However, differences between vortex ring formation in the phantom and in vivo may confound the results, and further experiments are needed to determine if MXR can be quantified using 4D PC-MR in vivo. – *Paper II*

In vivo vortex ring formation

- A new method for using Lagrangian Coherent Structures (LCS) to measure vortex ring volume (VV) in vivo was developed and implemented in software, and a fair interobserver and interstudy variability was found. Furthermore, in vivo vortex rings were less symmetric and more complex than in water tank experiments. – *Paper IV*

- A new method for quantification of vortex ring mixing ratio (MXR) was developed, using Volume Tracking (Paper III) and LCS in intracardiac 4D PC-MR data. Fair interobserver and interstudy agreement was found. – *Paper V*

- Vortex ring volume (VV) does not differ between healthy volunteers and heart failure patients, but VV/DV, the vortex ring volume in relation to the LV volume at diastasis (DV), is significantly lowered in heart failure patients, which may increase the risk for thrombus formation. – *Papers IV and V*

- MXR as measured with 4D PC-MR is higher in patients with heart failure compared to healthy volunteers. Furthermore, a smaller fraction of the end-systolic volume is mixed into the vortex ring during rapid filling in the patients compared to the healthy volunteers, which may signify a higher risk for thrombus formation in the patients. However, these results must be viewed in light of the validation study presented in Paper II. – *Paper V*

Visualization

- The visually perceived quality of intracardiac blood flow visualizations using particle tracing does not differ between 4D PC-MR accelerated using SENSE and k-t BLAST. – *Paper I*

- A new method for visualization of intracardiac blood flow, called Volume Tracking, was developed and its use demonstrated. Volume Tracking provides incremental information compared to particle tracing, e.g. by revealing a complex flow pattern in the right ventricle, not readily apparent using particle tracing. – *Paper III*

Bibliography

1. Hunt SA, Abraham WT, Chin MH, Feldman AM, Francis GS, Ganiats TG, Jessup M, Konstam Ma, Mancini DM, Michl K, Oates Ja, Rahko PS, Silver Ma, Stevenson LW, Yancy CW: **2009 Focused update incorporated into the ACC/AHA 2005 Guidelines for the Diagnosis and Management of Heart Failure in Adults A Report of the American College of Cardiology Foundation/American Heart Association Task Force on Practice Guidelines Developed** . *Journal of the American College of Cardiology* 2009, **53**(15):e1–e90.

2. Go AS, Mozaffarian D, Roger VL, Benjamin EJ, Berry JD, Blaha MJ, Dai S, Ford ES, Fox CS, Franco S, Fullerton HJ, Gillespie C, Hailpern SM, Heit Ja, Howard VJ, Huffman MD, Judd SE, Kissela BM, Kittner SJ, Lackland DT, Lichtman JH, Lisabeth LD, Mackey RH, Magid DJ, Marcus GM, Marelli A, Matchar DB, McGuire DK, Mohler ER, Moy CS, Mussolino ME, Neumar RW, Nichol G, Pandey DK, Paynter NP, Reeves MJ, Sorlie PD, Stein J, Towfighi A, Turan TN, Virani SS, Wong ND, Woo D, Turner MB: *Heart disease and stroke statistics–2014 update: a report from the American Heart Association.*, *Volume 129* 2014.

3. Bui AL, Horwich TB, Fonarow GC: **Epidemiology and risk profile of heart failure.** *Nature reviews. Cardiology* 2011, **8**:30–41.

4. Beppu S, Izumi S, Miyatake K, Nagata S, Park YD, Sakakibara H, Nimura Y: **Abnormal blood pathways in left ventricular cavity in acute myocardial infarction. Experimental observations with special reference to regional wall motion abnormality and hemostasis**. *Circulation* 1988, **78**:157.

5. Reiter G, Reiter U, Kovacs G, Kainz B, Schmidt K, Maier R, Olschewski H, Rienmueller R: **Magnetic resonance-derived 3-dimensional blood flow patterns in the main pulmonary artery as a marker of pulmonary hypertension and a measure of elevated mean pulmonary arterial pressure.** *Circulation. Cardiovascular imaging* 2008, **1**:23–30.

6. Thanigaraj S, Chugh R, Schechtman KB, Lee LV, Wade RL, Pérez JE: **Defining left ventricular segmental and global function by echocardiographic intraventricular contrast flow patterns**. *The American journal of cardiology* 2000, **85**:65–68.

7. Garcia MJ, Smedira NG, Greenberg NL, Main M, Firstenberg MS, Odabashian J, Thomas JD: **Color M-mode Doppler flow propagation velocity is a preload insensitive index of left ventricular relaxation: animal and human validation**. *Journal of the American College of Cardiology* 2000, **35**:201–208.

8. Eriksson J, Dyverfeldt P, Engvall J, Bolger AF, Ebbers T, Carlhäll CJ: **Quantification of presystolic blood flow organization and energetics in the human left ventricle.** *American journal of physiology. Heart and circulatory physiology* 2011, **300**(6):H2135–41.

9. Kilner PJ, Yang GZ, Wilkes AJ, Mohiaddin RH, Firmin DN, Yacoub MH: **Asymmetric redirection of flow through the heart.** *Nature* 2000, **404**(6779):759–61.

10. Braunwald E, Zipes DP, Libby P (Eds): *Heart Disase, a textbook of cardiovascular medicine*. Philadelphia: W B Saunders Co, 6th edition 2001.

11. Vander A, Sherman J, Luciano D: *Human physiology: the mechanisms of body function*. New York: McGraw-Hill, 8th edition 2001.

12. Carlsson M, Cain P, Holmqvist C, Stahlberg F, Lundback S, Arheden H: **Total heart volume variation throughout the cardiac cycle in humans.** *American journal of physiology. Heart and circulatory physiology* 2004, **287**:H243–50.

13. Carlsson M, Ugander M, Mosén H, Buhre T, Arheden H: **Atrioventricular plane displacement is the major contributor to left ventricular pumping in healthy adults, athletes, and patients with dilated cardiomyopathy.** *American journal of physiology. Heart and circulatory physiology* 2007, **292**(3):H1452–9.

14. Carlsson M, Ugander M, Heiberg E, Arheden H: **The quantitative relationship between longitudinal and radial function in left, right, and total heart pumping in humans.** *American journal of physiology. Heart and circulatory physiology* 2007, **293**:H636–44.

15. Steding-Ehrenborg K, Carlsson M, Stephensen S, Arheden H: **Atrial aspiration from pulmonary and caval veins is caused by ventricular contraction and secures 70% of the total stroke volume independent of resting heart rate and heart size.** *Clinical physiology and functional imaging* 2013, **33**(3):233–40.

16. Chung CS, Karamanoglu M, Kovács SJ, Kovacs SJ: **Duration of diastole and its phases as a function of heart rate during supine bicycle exercise.** *American journal of physiology. Heart and circulatory physiology* 2004, **287**(5):2003–2008.

17. Helmes M, Trombitás K, Granzier H: **Titin develops restoring force in rat cardiac myocytes.** *Circulation research* 1996, **79**(3):619–26.

18. Granzier HL, Irving TC: **Passive tension in cardiac muscle: contribution of collagen, titin, microtubules, and intermediate filaments.** *Biophysical journal* 1995, **68**(3):1027–44.

19. Granzier H, Labeit S: **Cardiac titin: an adjustable multi-functional spring**. *The Journal of Physiology* 2002, **541**(2):335–342.

20. Brecher GA: **Experimental Evidence of Ventricular Diastolic Suction**. *Circulation Research* 1956, **4**(5):513–518.

21. Brecher GA: **Critical Review of Recent Work on Ventricular Diastolic Suction**. *Circulation Research* 1958, **6**(5):554–566.

22. Udelson JE, Bacharach SL, Cannon RO, Bonow RO: **Minimum left ventricular pressure during beta-adrenergic stimulation in human subjects. Evidence for elastic recoil and diastolic "suction" in the normal heart.** *Circulation* 1990, **82**(4):1174–82.

23. Bell SP, Nyland L, Tischler MD, McNabb M, Granzier H, LeWinter MM: **Alterations in the Determinants of Diastolic Suction During Pacing Tachycardia**. *Circulation Research* 2000, **87**(3):235–240.

24. Shmuylovich L, Chung CS, Kovács SJ: **Point: Left ventricular volume during diastasis is the physiological in vivo equilibrium volume and is related to diastolic suction.** *Journal of applied physiology* 2010, **109**(2):606–8.

25. Shmuylovich L, Chung CS, Kovács SJ: **Last Word on Point:Counterpoint: Left ventricular volume during diastasis is the physiological in vivo equilibrium volume and is related to diastolic suction**. *Journal of Applied Physiology* 2010, **109**:615.

26. Zhang W, Chung CS, Shmuylovich L, Kovács SJ: **Is left ventricular volume during diastasis the real equilibrium volume, and what is its relationship to diastolic suction?** *Journal of Applied Physiology* 2008, **105**(3):1012–1014.

27. Zhang W, Chung CS, Shmuylovich L, Kovacs SJ: **Last Word on Viewpoint: Is left ventricular volume during diastasis the real equilibrium volume, and what is its relationship to diastolic suction?** *Journal of Applied Physiology* 2008, **105**(3):1019.

28. Ade CJ, Wong BJ: **Commentary on Viewpoint: Is left ventricular volume during diastasis the real equilibrium volume, and what is the relationship to diastolic suction?** *Journal of applied physiology* 2008, **105**(3):1017.

29. Yellin E, Nikolic SD: **Counterpoint: Left ventricular volume during diastasis is not the physiological in vivo equilibrium volume and is not related to diastolic suction.** *Journal of applied physiology* 2010, **109**(2):608–10.

30. Yellin EL, Nikolic SD: **Last word on point: Counterpoint: Left ventricular volume during diastasis is not the physiological in vivo equilibrium volume and is not related to diastolic suction.** *Journal of applied physiology* 2010, **109**(2):616.

31. Tyber JV, Remme EW, Yildiz M, Bermejo J, Can Z, Little WC, Parker KH, Smiseth OA, Sahin A: **Comments on Point:Counterpoint: Left ventricular volume during diastasis is/is not the physiological in vivo equilibrium volume and is/is not related to diastolic suction**. *Journal of Applied Physiology* 2010, **109**:612–614.

32. Jonson B, Wollmer P (Eds): *Klinisk Fysiolgi*. Stockholm: Liber, 3rd edition 2011.

33. Jessup M, Brozena S: **Heart failure.** *The New England journal of medicine* 2003, **348**(20):2007–18.

34. Hanson LG: **Is quantum mechanics necessary for understanding magnetic resonance?** *Concepts in Magnetic Resonance Part A* 2008, **32A**(5):329–340.

35. Kramer CM, Barkhausen J, Flamm SD, Kim RJ, Nagel E: **Standardized cardiovascular magnetic resonance imaging (CMR) protocols, society for cardiovascular magnetic resonance: board of trustees task force on standardized protocols.** *Journal of cardiovascular magnetic resonance* 2008, **10**:35.

36. Hahn EL: **Detection of sea-water motion by nuclear precession**. *Journal of Geophysical Research* 1960, **65**(2):776–777.

37. Nayler GL, Firmin DN, Longmore DB: **Blood flow imaging by cine magnetic resonance.** *Journal of computer assisted tomography* 1986, **10**(5):715–22.

38. Stahlberg F, Mogelvang J, Thomsen C, Nordell B, Stubgaard M, Ericsson A, Sperber G, Greitz D, Larsson H, Henriksen O: **A method for MR quantification of flow velocities in blood and CSF using interleaved gradient-echo pulse sequences.** *Magnetic resonance imaging* 1989, **7**(6):655–67.

39. Pelc NJ, Bernstein MA, Shimakawa A, Glover GH: **Encoding strategies for three-direction phase-contrast MR imaging of flow.** *Journal of magnetic resonance imaging : JMRI* 1991, **1**(4):405–13.

40. Wigström L, Sjövist L, Wranne B, Sjöqvist L: **Temporally resolved 3D phase-contrast imaging**. *Magnetic Resonance in Medicine* 1996, **36**(5):800–803.

41. Markl M, Kilner PJ, Ebbers T: **Comprehensive 4D velocity mapping of the heart and great vessels by cardiovascular magnetic resonance.** *Journal of cardiovascular magnetic resonance : official journal of the Society for Cardiovascular Magnetic Resonance* 2011, **13**:7.

42. Markl M, Frydrychowicz A, Kozerke S, Hope M, Wieben O: **4D flow MRI**. *Journal of Magnetic Resonance Imaging* 2012, **36**(5):1015–1036.

43. Contur TE, Robinson BH: **Analysis of encoding efficiency in MR imaging of velocity magnitude and direction**. *Magnetic Resonance in Medicine* 1992, **25**(2):233–247.

44. Dumoulin CL, Souza SP, Darrow RD, Pelc NJ, Adams WJ, Ash SA: **Simultaneous acquisition of phase-contrast angiograms and stationary-tissue images with Hadamard encoding of flow-induced phase shifts**. *Journal of Magnetic Resonance Imaging* 1991, **1**(4):399–404.

45. Johnson KM, Markl M: **Improved SNR in phase contrast velocimetry with five-point balanced flow encoding.** *Magnetic resonance in medicine* 2010, **63**(2):349–55.

46. Espe EKS, Aronsen JM, Skrbic B, Skulberg VM, Schneider JE, Sejersted OM, Zhang L, Sjaastad I: **Improved MR phase-contrast velocimetry using a novel nine-point balanced motion-encoding scheme with increased robustness to eddy current effects.** *Magnetic resonance in medicine* 2013, **69**:48–61.

47. Nilsson A, Bloch KM, Carlsson M, Heiberg E, Stahlberg F: **Variable velocity encoding in a three-dimensional, three-directional phase contrast sequence: Evaluation in phantom and volunteers.** *Journal of magnetic resonance imaging* 2012, **36**(6):1450–9.

48. Bogren HG, Klipstein RH, Firmin DN, Mohiaddin RH, Underwood SR, Rees RS, Longmore DB: **Quantitation of antegrade and retrograde blood flow in the human aorta by magnetic resonance velocity mapping.** *American heart journal* 1989, **117**(6):1214–22.

49. Kondo C, Caputo GR, Semelka R, Foster E, Shimakawa A, Higgins CB: **Right and left ventricular stroke volume measurements with velocity-encoded cine MR imaging: in vitro and in vivo validation.** *American journal of roentgenology* 1991, **157**:9–16.

50. Van Rossum AC, Sprenger M, Visser FC, Peels KH, Valk J, Roos JP: **An in vivo validation of quantitative blood flow imaging in arteries and veins using magnetic resonance phase-shift techniques.** *European heart journal* 1991, **12**(2):117–26.

51. Rebergen SA, van der Wall EE, Helbing WA, de Roos A, van Voorthuisen AE: **Quantification of pulmonary and systemic blood flow by magnetic resonance velocity mapping in the assessment of atrial-level shunts.** *International journal of cardiac imaging* 1996, **12**(3):143–52.

52. Arheden H, Holmqvist C, Thilen U, Hanséus K, Björkhem G, Pahlm O, Laurin S, Stahlberg F: **Left-to-right cardiac shunts: comparison of measurements obtained with MR velocity mapping and with radionuclide angiography.** *Radiology* 1999, **211**(2):453–8.

53. Carlsson M, Andersson R, Bloch KM, Steding-Ehrenborg K, Mosén H, Stahlberg F, Ekmehag B, Arheden H: **Cardiac output and cardiac index measured with cardiovascular magnetic resonance in healthy subjects, elite athletes and patients with congestive heart failure.** *Journal of cardiovascular magnetic resonance* 2012, **14**:51.

54. Brenner LD, Caputo GR, Mostbeck G, Steiman D, Dulce M, Cheitlin MD, O'Sullivan M, Higgins CB: **Quantification of left to right atrial shunts with velocity-encoded cine nuclear magnetic resonance imaging.** *Journal of the American College of Cardiology* 1992, **20**(5):1246–50.

55. Hundley WG, Li HF, Hillis LD, Meshack BM, Lange RA, Willard JE, Landau C, Peshock RM: **Quantitation of cardiac output with velocity-encoded, phase-difference magnetic resonance imaging**. *The American Journal of Cardiology* 1995, **75**(17):1250–1255.

56. Gatehouse PD, Rolf MP, Graves MJ, Hofman MB, Totman J, Werner B, Quest Ra, Liu Y, von Spiczak J, Dieringer M, Firmin DN, van Rossum A, Lombardi M, Schwitter J, Schulz-Menger J, Kilner PJ: **Flow measurement by cardiovascular magnetic resonance: a multi-centre multi-vendor study of background phase offset errors that can compromise the accuracy of derived regurgitant or shunt flow measurements.** *Journal of cardiovascular magnetic resonance* 2010, **12**:5.

57. Rolf MP, Hofman MBM, Gatehouse PD, Markenroth-Bloch K, Heymans MW, Ebbers T, Graves MJ, Totman JJ, Werner B, van Rossum AC, Kilner PJ, Heethaar RM: **Sequence optimization to reduce velocity offsets in cardiovascular magnetic resonance volume flow quantification–a multi-vendor study.** *Journal of cardiovascular magnetic resonance* 2011, **13**:18.

58. Gatehouse PD, Rolf MP, Markenroth Bloch K, Graves MJ, Kilner PJ, Firmin DN, Hofman MB: **A multi-center inter-manufacturer study of the temporal stability of phase-contrast velocity mapping background offset errors.** *Journal of cardiovascular magnetic resonance* 2012, **14**:72.

59. Bernstein MA, Zhou XJ, Polzin Ja, King KF, Ganin A, Pelc NJ, Glover GH: **Concomitant gradient terms in phase contrast MR: analysis and correction.** *Magnetic resonance in medicine* 1998, **39**(2):300–8.

60. Chernobelsky A, Shubayev O, Comeau CR, Wolff SD: **Baseline correction of phase contrast images improves quantification of blood flow in the great vessels.** *Journal of cardiovascular magnetic resonance* 2007, **9**(4):681–5.

61. Walker PG, Cranney GB, Scheidegger MB, Waseleski G, Pohost GM, Yoganathan AP: **Semiautomated method for noise reduction and background phase error correction in MR phase velocity data**. *Journal of Magnetic Resonance Imaging* 1993, **3**(3):521–530.

62. Lankhaar JW, Hofman MBM, Marcus JT, Zwanenburg JJM, Faes TJC, Vonk-Noordegraaf A: **Correction of phase offset errors in main pulmonary artery flow quantification.** *Journal of magnetic resonance imaging* 2005, **22**:73–9.

63. Brix L, Ringgaard S, Rasmusson A, Sø rensen TS, Kim WY: **Three dimensional three component whole heart cardiovascular magnetic resonance velocity mapping: comparison of flow measurements from 3D and 2D acquisitions.** *Journal of cardiovascular magnetic resonance* 2009, **11**:3.

64. Tariq U, Hsiao A, Alley M, Zhang T, Lustig M, Vasanawala SS: **Venous and arterial flow quantification are equally accurate and precise with parallel imaging compressed sensing 4D phase contrast MRI.** *Journal of magnetic resonance imaging* 2013, **37**(6):1419–26.

65. Hsiao A, Tariq U, Alley MT, Lustig M, Vasanawala SS: **Inlet and outlet valve flow and regurgitant volume may be directly and reliably quantified with accelerated, volumetric phase-contrast MRI.** *Journal of magnetic resonance imaging* 2014.

66. Wigström L, Ebbers T, Fyrenius A, Karlsson M, Engvall J, Wranne B, Bolger AF: **Particle trace visualization of intracardiac flow using time-resolved 3D phase contrast MRI.** *Magnetic resonance in medicine* 1999, **41**(4):793–9.

67. Eriksson J, Carlhäll CJ, Dyverfeldt P, Engvall J, Bolger AF, Ebbers T: **Semi-automatic quantification of 4D left ventricular blood flow**. *Journal of Cardiovascular Magnetic Resonance* 2010, **12**:9.

68. Sigfridsson A, Petersson S, Carlhäll CJ, Ebbers T: **Four-dimensional flow MRI using spiral acquisition.** *Magnetic resonance in medicine* 2012, **68**(4):1065–73.

69. Elkins CJ, Alley MT, Saetran L, Eaton JK: **Three-dimensional magnetic resonance velocimetry measurements of turbulence quantities in complex flow**. *Experiments in Fluids* 2008, **46**(2):285–296.

70. Knobloch V, Binter C, Gülan U, Sigfridsson A, Holzner M, Lüthi B, Kozerke S: **Mapping mean and fluctuating velocities by Bayesian multipoint MR velocity encoding-validation against 3D particle tracking velocimetry.** *Magnetic resonance in medicine* 2014, **71**(4):1405–15.

71. Nilsson A, Bloch KM, Töger J, Heiberg E, Stahlberg F: **Accuracy of four-dimensional phase-contrast velocity mapping for blood flow visualizations: a phantom study.** *Acta radiologica* 2013.

72. Adrian RJ: **Twenty years of particle image velocimetry**. *Experiments in Fluids* 2005, **39**(2):159–169.

73. Raffel M, Willert C, Kompenhans J: *Particle Image Velocimetry: a practical guide*. Berlin: Springer Verlag 2007.

74. Crimaldi JP: **Planar laser induced fluorescence in aqueous flows**. *Experiments in Fluids* 2008, **44**(6):851–863.

75. Simoens S, Ayrault M: **Concentration flux measurements of a scalar quantity in turbulent flows**. *Experiments in Fluids* 1994, **16-16**(3-4):273–281.

76. Law AWk, Wang H: **Measurement of mixing processes with combined digital particle image velocimetry and planar laser induced fluorescence**. *Experimental Thermal and Fluid Science* 2000, **22**(3-4):213–229.

77. Penzkofer A, Leupacher W: **Fluorescence behaviour of highly concentrated rhodamine 6G solutions**. *Journal of Luminescence* 1987, **37**(2):61–72.

78. Napel S, Lee DH, Frayne R, Rutt BK: **Visualizing three-dimensional flow with simulated streamlines and three-dimensional phase-contrast MR imaging.** *Journal of magnetic resonance imaging* 1992, **2**(2):143–53.

79. Laidlaw DH, Kirby RM, Jackson CD, Davidson JS, Miller TS, Da Silva M, Warren WH, Tarr MJ: **Comparing 2D vector field visualization methods: A user study**. *IEEE Transactions on Visualization and Computer Graphics* 2005, :59–70.

80. Forsberg A, Chen J, Laidlaw D: **Comparing 3D Vector Field Visualization Methods: A User Study**. *IEEE Transactions on Visualization and Computer Graphics* 2009, **15**(6):1219–1226.

81. Post FH, Vrolijk B, Hauser H, Laramee RS, Doleisch H: **Feature extraction and visualization of flow fields**. *Eurographics 2002 State-of-the-Art Reports* 2002.

82. Buonocore MH: **Visualizing blood flow patterns using streamlines, arrows, and particle paths**. *Magnetic resonance in medicine* 1998, **40**(2):210–226.

83. Heiberg E, Ebbers T, Wigstrom L, Karlsson M, Wigström L: **Three-dimensional flow characterization using vector pattern matching**. *IEEE Transactions on Visualization and Computer Graphics* 2003, **9**(3):313–319.

84. McLoughlin T, Laramee RS, Peikert R, Post FH, Chen M: **Over two decades of integration-based, geometric flow visualization**. *Eurographics 2009, State of the Art Reports* 2009.

85. Shadden SC, Arzani A: **Lagrangian Postprocessing of Computational Hemodynamics**. *Annals of Biomedical Engineering* 2014.

86. Shadden SC, Taylor Ca: **Characterization of coherent structures in the cardiovascular system.** *Annals of biomedical engineering* 2008, **36**(7):1152–62.

87. Shadden SC, Astorino M, Gerbeau JF, Paris-rocquencourt I, Voluceau DD, Le RBP: **Computational analysis of an aortic valve jet with Lagrangian coherent structures.** *Chaos* 2010, **20**:017512.

88. Krishnan H, Garth C, Guhring J, Gulsun MA, Greiser A, Joy KI: **Analysis of Time-Dependent Flow-Sensitive PC-MRI Data.** *IEEE transactions on visualization and computer graphics* 2011.

89. Lekien F, Coulliette C, Mariano a, Ryan E, Shay L, Haller G, Marsden J: **Pollution release tied to invariant manifolds: A case study for the coast of Florida**. *Physica D: Nonlinear Phenomena* 2005, **210**(1-2):1–20.

90. Haller G, Yuan G: **Lagrangian coherent structures and mixing in two-dimensional turbulence**. *Physica D: Nonlinear Phenomena* 2000, **147**(3-4):352–370.

91. Haller G: **Distinguished material surfaces and coherent structures in three-dimensional fluid flows**. *Physica D* 2001, **149**:248–277.

92. Shadden SC, Lekien F, Marsden JE: **Definition and properties of Lagrangian coherent structures from finite-time Lyapunov exponents in two-dimensional aperiodic flows**. *Physica D: Nonlinear Phenomena* 2005, **212**(3-4):271–304.

93. Olcay AB, Pottebaum TS, Krueger PS: **Sensitivity of Lagrangian coherent structure identification to flow field resolution and random errors.** *Chaos* 2010, **20**:017506.

94. Sadlo F, Peikert R: **Efficient visualization of lagrangian coherent structures by filtered AMR ridge extraction.** *IEEE transactions on visualization and computer graphics* 2007, **13**(6):1456–63.

95. Bellhouse BJ, Bellhouse FH: **Fluid Mechanics of the Mitral Valve**. *Nature* 1969, **224**(5219):615–616.

96. Bellhouse BJ: **Fluid mechanics of a model mitral valve and left ventricle.** *Cardiovascular research* 1972, **6**(2):199–210.

97. Gharib M, Rambod E, Shariff K: **A universal time scale for vortex ring formation**. *Journal of Fluid Mechanics* 1998, **360**:121–140.

98. Gharib M, Rambod E, Kheradvar A, Sahn DJ, Dabiri JO: **Optimal vortex formation as an index of cardiac health.** *Proceedings of the National Academy of Sciences of the United States of America* 2006, **103**(16):6305–8.

99. Poh KK, Lee LC, Shen L, Chong E, Tan YL, Chai P, Yeo TC, Wood MJ: **Left ventricular fluid dynamics in heart failure: echocardiographic measurement and utilities of vortex formation time.** *European heart journal Cardiovascular Imaging* 2012, **13**(5):385–93.

100. Kheradvar A, Assadi R, Falahatpisheh A, Sengupta PP: **Assessment of Transmitral Vortex Formation in Patients with Diastolic Dysfunction.** *Journal of the American Society of Echocardiography* 2012, **25**(2):220–227.

101. Shariff K, Leonard a: **Vortex Rings**. *Annual Review of Fluid Mechanics* 1992, **24**:235–279.

102. Lim TT, Nickels T: **Vortex Rings**. In *Fluid Vortices*. Edited by Green B, Springer 1995:95–153.

103. Shadden SC, Dabiri JO, Marsden JE: **Lagrangian Analysis of fluid transport in empirical vortex ring flows**. *Physics of Fluids* 2006, **18**(4):047105.

104. Olcay AB, Krueger PS: **Measurement of ambient fluid entrainment during laminar vortex ring formation**. *Experiments in Fluids* 2008, **44**(2):235–247.

105. Shadden SC, Katija K, Rosenfeld M, Marsden JE, Dabiri JO: **Transport and stirring induced by vortex formation**. *Journal of Fluid Mechanics* 2007, **593**:315–331.

106. Didden N: **Untersuchung laminarer, instabiler Ringwirbel mittels Laser-Doppler-Anemometrie**. Tech. rep., Max-Planck-Institut für Strömungsforschung, Göttingen 1977.

107. Krueger PS, Dabiri JO, Gharib M: **The formation number of vortex rings formed in uniform background co-flow**. *Journal of Fluid Mechanics* 2006, **556**:147.

108. Müller EA, Didden N: **Zur Erzeugung der Zirkulation bei der Bildung eines Ringwirbels an einer Düsenmündung**. *Strojnícky Casopis* 1980, **31**(3):363.

109. Liess C: **Experimentelle Untersuchung des Lebenslaufes von Ringwirbeln**. Tech. rep., Max-Planck-Institut für Strömungsforschung, Göttingen, Göttningen 1978.

110. Didden N: **On the formation of vortex rings: Rolling-up and production of circulation**. *Zeitschrift für angewandte Mathematik und Physik* 1979, **30**:101–116.

111. Thomson W: **Vortex statics**. *Philosophical Magazine Series 5* 1880, **10**(60):97–109.

112. Brooke Benjamin T: **The alliance of practical and analytical insights into the nonlinear problems of fluid mechanics**. *Lecture Notes in Mathematics* 1976, **503**:8–29.

113. Rosenfeld M, Rambod E, Gharib M: **Circulation and formation number of laminar vortex rings**. *Journal of Fluid Mechanics* 1998, **376**:297–318.

114. Mohseni K, Gharib M: **A model for universal time scale of vortex ring formation**. *Physics of Fluids* 1998, **10**(10):2436.

115. Rosenfeld M, Katija K, Dabiri JO: **Circulation Generation and Vortex Ring Formation by Conic Nozzles**. *Journal of Fluids Engineering* 2009, **131**(9):091204.

116. Domenichini F: **Three-dimensional impulsive vortex formation from slender orifices**. *Journal of Fluid Mechanics* 2011, **666**:506–520.

117. Dabiri JO, Gharib M: **The role of optimal vortex formation in biological fluid transport.** *Proceedings of the Royal Society B: Biological sciences* 2005, **272**(1572):1557–60.

118. Palacios-Morales C, Zenit R: **Vortex ring formation for low Re numbers**. *Acta Mechanica* 2012, **224**(2):383–397.

119. Dabiri JO, Gharib M: **Delay of vortex ring pinchoff by an imposed bulk counterflow**. *Physics of Fluids* 2004, **16**(4):L28.

120. Auerbach D: **Stirring properties of vortex rings**. *Physics of Fluids A* 1991, **3**(5):1351–1355.

121. Dabiri JO, Gharib M: **Fluid entrainment by isolated vortex rings**. *Journal of Fluid Mechanics* 2004, **511**:311–331.

122. Maxworthy T: **The structure and stability of vortex rings**. *J. Fluid Mech* 1972, **51**:15–32.

123. Reul H, Talukder N, Müller E: **Fluid mechanics of the natural mitral valve**. *Journal of Biomechanics* 1981, **14**(5):361–372.

124. Van Dantzig JM, Delemarre BJ, Bot H, Koster RW, Visser Ca: **Doppler left ventricular flow pattern versus conventional predictors of left ventricular thrombus after acute myocardial infarction.** *Journal of the American College of Cardiology* 1995, **25**(6):1341–6.

125. Belohlavek M, Jiamsripong P, Calleja AM, McMahon EM, Maarouf CL, Kokjohn TA, Chaffin TL, Vedders LJ, Garami Z, Beach TG, Sabbagh MN, Roher AE: **Patients with Alzheimer disease have altered transmitral flow: echocardiographic analysis of the vortex formation time.** *Journal of ultrasound in medicine* 2009, **28**(11):1493–500.

126. Jiamsripong P, Calleja AM, Alharthi MS, Dzsinich M, McMahon EM, Heys JJ, Milano M, Sengupta PP, Khandheria BK, Belohlavek M: **Impact of acute moderate elevation in left ventricular afterload on diastolic transmitral flow efficiency: analysis by vortex formation time.** *Journal of the American Society of Echocardiography* 2009, **22**(4):427–31.

127. Ghosh E, Shmuylovich L, Kovács SJ: **Vortex formation time-to-left ventricular early rapid filling relation: model-based prediction with echocardiographic validation.** *Journal of applied physiology* 2010, **109**(6):1812–9.

128. Stewart KC, Charonko JC, Niebel CL, Little WC, Vlachos PP: **Left ventricular vortex formation is unaffected by diastolic impairment.** *American journal of physiology. Heart and circulatory physiology* 2012, **303**(10):H1255–62.

129. Stewart KC, Kumar R, Charonko JJ, Ohara T, Vlachos PP, Little WC: **Evaluation of LV diastolic function from color M-mode echocardiography.** *Journal of the American College of Cardiology: Cardiovascular Imaging* 2011, **4**:37–46.

130. Dyverfeldt P, Kvitting JPE, Sigfridsson A, Engvall J, Bolger AF, Ebbers T: **Assessment of fluctuating velocities in disturbed cardiovascular blood flow: in vivo feasibility of generalized phase-contrast MRI.** *Journal of magnetic resonance imaging* 2008, **28**(3):655–63.

131. Tsao J, Boesiger P, Pruessmann KP: **k-t BLAST and k-t SENSE: dynamic MRI with high frame rate exploiting spatiotemporal correlations.** *Magnetic resonance in medicine* 2003, **50**(5):1031–42.

132. Baltes C, Kozerke S, Hansen MS, Pruessmann KP, Tsao J, Boesiger P: **Accelerating cine phase-contrast flow measurements using k-t BLAST and k-t SENSE.** *Magnetic resonance in medicine* 2005, **54**(6):1430–8.

133. Heiberg E, Sjögren J, Ugander M, Carlsson M, Engblom H, Arheden Hk: **Design and validation of Segment–freely available software for cardiovascular image analysis.** *BMC medical imaging* 2010, **10**:1.

134. Surawicz B, Childers R, Deal BJ, Gettes LS, Bailey JJ, Gorgels A, Hancock EW, Josephson M, Kligfield P, Kors Ja, Macfarlane P, Mason JW, Mirvis DM, Okin P, Pahlm O, Rautaharju PM, van Herpen G, Wagner GS, Wellens H: **AHA/ACCF/HRS recommendations for the standardization and interpretation of the electrocardiogram: part III: intraventricular conduction disturbances: a scientific statement from the American Heart Association Electrocardiography and Arrhythmias Committee,**. *Journal of the American College of Cardiology* 2009, **53**(11):976–81.

135. Altman DG, Bland JM: **Measurement in Medicine: The Analysis of Method Comparison Studies**. *The Statistician* 1983, **32**(3):307.

136. Cerqueira MD, Weissman NJ, Dilsizian V, Jacobs AK, Kaul S, Laskey WK, Pennell DJ, Rumberger JA, Ryan T, Verani MS: **Standardized myocardial segmentation and nomenclature for tomographic imaging of the heart: a statement for healthcare professionals from the Cardiac Imaging Committee of the Council on Clinical Cardiology of the American Heart Association**. *Circulation* 2002, **105**(4):539–542.

137. **PS 3.3 C.7.6.1 General Image Module**. In *DICOM Standard*, 2014a edition, Arlington, VA, USA: NEMA 2014.

138. LeVeque RJ: **High-Resolution Conservative Algorithms for Advection in Incompressible Flow**. *SIAM Journal on Numerical Analysis* 1996, **33**(2):627–665.

139. Langseth JO, LeVeque RJ: **A Wave Propagation Method for Three-Dimensional Hyperbolic Conservation Laws**. *Journal of Computational Physics* 2000, **165**:126–166.

140. LeVeque RJ: **CLAWPACK Homepage**[http://clawpack.github.io/index.html].

141. Markl M, Chan FP, Alley MT, Wedding KL, Draney MT, Elkins CJ, Parker DW, Wicker R, Taylor CA, Herfkens RJ, Pelc NJ: **Time-resolved three-dimensional phase-contrast MRI.** *Journal of magnetic resonance imaging* 2003, **17**(4):499–506.

142. Markl M, Draney MT, Hope MD, Levin JM, Chan FP, Alley MT, Pelc NJ, Herfkens RJ: **Time-resolved 3-dimensional velocity mapping in the thoracic aorta: visualization of 3-directional blood flow patterns in healthy volunteers and patients.** *Journal of computer assisted tomography* 2004, **28**(4):459–68.

143. Stalder aF, Russe MF, Frydrychowicz A, Bock J, Hennig J, Markl M: **Quantitative 2D and 3D phase contrast MRI: optimized analysis of blood flow and vessel wall parameters.** *Magnetic resonance in medicine* 2008, **60**(5):1218–31.

144. Westenberg JJM, Roes SD, Ajmone Marsan N, Binnendijk NMJ, Doornbos J, Bax JJ, Reiber JHC, de Roos A, van der Geest RJ: **Mitral valve and tricuspid valve blood flow: accurate quantification with 3D velocity-encoded MR imaging with retrospective valve tracking.** *Radiology* 2008, **249**(3):792–800.

145. van der Hulst AE, Westenberg JJM, Kroft LJM, Bax JJ, Blom NA, de Roos A, Roest AAW: **Tetralogy of fallot: 3D velocity-encoded MR imaging for evaluation of right ventricular valve flow and diastolic function in patients after correction.** *Radiology* 2010, **256**(3):724–34.

146. Marshall I: **Feasibility of k-t BLAST technique for measuring "seven-dimensional" fluid flow.** *Journal of magnetic resonance imaging* 2006, **23**(2):189–96.

147. Stadlbauer A, van der Riet W, Globits S, Crelier G, Salomonowitz E: **Accelerated phase-contrast MR imaging: comparison of k-t BLAST with SENSE and Doppler ultrasound for velocity and flow measurements in the aorta.** *Journal of magnetic resonance imaging* 2009, **29**(4):817–24.

148. Liu J, Dyverfeldt P, Acevedo-Bolton G, Hope M, Saloner D: **Highly Accelerated Aortic 4D Flow MR Imaging with Variable-Density Random Undersampling.** *Magnetic resonance imaging* 2014.

149. Giese D, Wong J, Greil GF, Buehrer M, Schaeffter T, Kozerke S: **Towards highly accelerated Cartesian time-resolved 3D flow cardiovascular magnetic resonance in the clinical setting.** *Journal of cardiovascular magnetic resonance* 2014, **16**:42.

150. Harloff A, Zech T, Wegent F, Strecker C, Weiller C, Markl M: **Comparison of blood flow velocity quantification by 4D flow MR imaging with ultrasound at the carotid bifurcation.** *American journal of neuroradiology* 2013, **34**(7):1407–13.

151. Ho S: **Anatomy of the mitral valve**. *Heart* 2002, **88**(suppl 4):iv5–iv10.

152. Sharma ND: **Left Ventricular Thrombus and Subsequent Thromboembolism in Patients With Severe Systolic Dysfunction**. *Chest* 2000, **117**(2):314–320.

Acknowledgments

To my main supervisor *Einar Heiberg* – thank you for your unconditional support and boldly letting me go where no man has gone before. Further thanks to my co-supervisors *Håkan Arheden* for group leadership, coaching and wonderfully challenging discussions, *Gustaf Söderlind* for teaching me computer problem-solving and the intricacies of academia, and to *Marcus Carlsson* for showing me and the world that anything is possible.

Rare it is to be given the opportunity to pursue a Ph.D. Rarer still to have unwavering support during the whole journey. Vanishingly rare it must be to have the opportunity to work in a group like the *Cardiac MR Group* at the Department of Clinical Physiology, Lund University. Thank you for excellent science, for showing me the path of development as a leader and human being, and for infinite patience in letting me make my own mistakes. Special thanks to *Mikael Kanski* for friendship and close collaboration and *Katarina Steding-Ehrenborg* for friendship and letting me look up to you.

Thank you *Sándor J. Kovács* at Washington University, St. Louis, USA, for your endless energy and passion for teaching me and the world how the heart really pumps. Thanks also to *Johan Revstedt* at the Department of Energy Sciences at Lund University, for generous access to laboratories, equipment and wisdom in fluid mechanics. To *Rasmus Borgqvist* at the Department of Arrhythmias in Lund – thanks for help with patient data and putting up with my echocardiographic whims. Thank you *Tomas Hajdu* at the Department of Medical Technology at Skåne University Hospital, Lund, Sweden for skillful design and construction of the vortex ring phantom setup, and *Lisa Eneroth* for hard work on laser experiments.

Thanks to *Freddy Ståhlberg* and *Anders Nilsson* at the Department of Medical Radiation Physics, Lund University and *Karin Markenroth-Bloch* at Philips Medical Systems for excellent guidance and feedback on my work.

It has been a joy to work at the *Department of Clinical Physiology and Nuclear Medicine* at Lund University Hospital. Thanks to everyone for a great atmosphere, especially *Annica Svensson* for coffee and hugs. Another big thank-you to all my colleagues at the *Department of Numerical Analysis* at Lund University for the opportunity to teach and to learn.

Tack till alla mina vänner, speciellt *Erik Alerstam* och *Markus Nilsson* för att ni vandrade vägen mot disputation före mig och visade mig vägen framåt de gånger jag gick vilse. All min kärlek och tacksamhet till mina föräldrar *Britta Töger* och *Tore Töger* – tack för allt. Samma kärlek går till min farmor *Majvi Töger* och min mormor *Ethel Svensson*. Till *Erik*, *Anna-Karin* och *Maja Töger* – I will always be your soldier.

ॐ

Funding

The work in this thesis was made possible by generous funding from the Swedish Research Council (Vetenskapsrådet, VR 621-2005-3129, 621-2008-2949, 2008-2461, K2009-65X-14599-07-3, 2012-4944), the Swedish Heart-Lung Foundation (Hjärt-Lung-fonden), National Visualization Program and Knowledge Foundation (KK-stiftelsen) grant 2008-0080, the Medical Faculty at Lund University, Sweden, and the Region of Scania (Region Skåne).

Travel grants for presenting and discussing my research at international conferences have been generously provided by the Swedish Society for Clinical Physiology and Nuclear Medicine (SSCPNM), Svensk Förening för Klinisk Fysiologi (SFKF), Bernt Järmarks stiftelse för vetenskaplig forskning, Thorild Dahlgrens fond and the Swedish Heart-Lung Foundation (Hjärt-Lung-fonden).

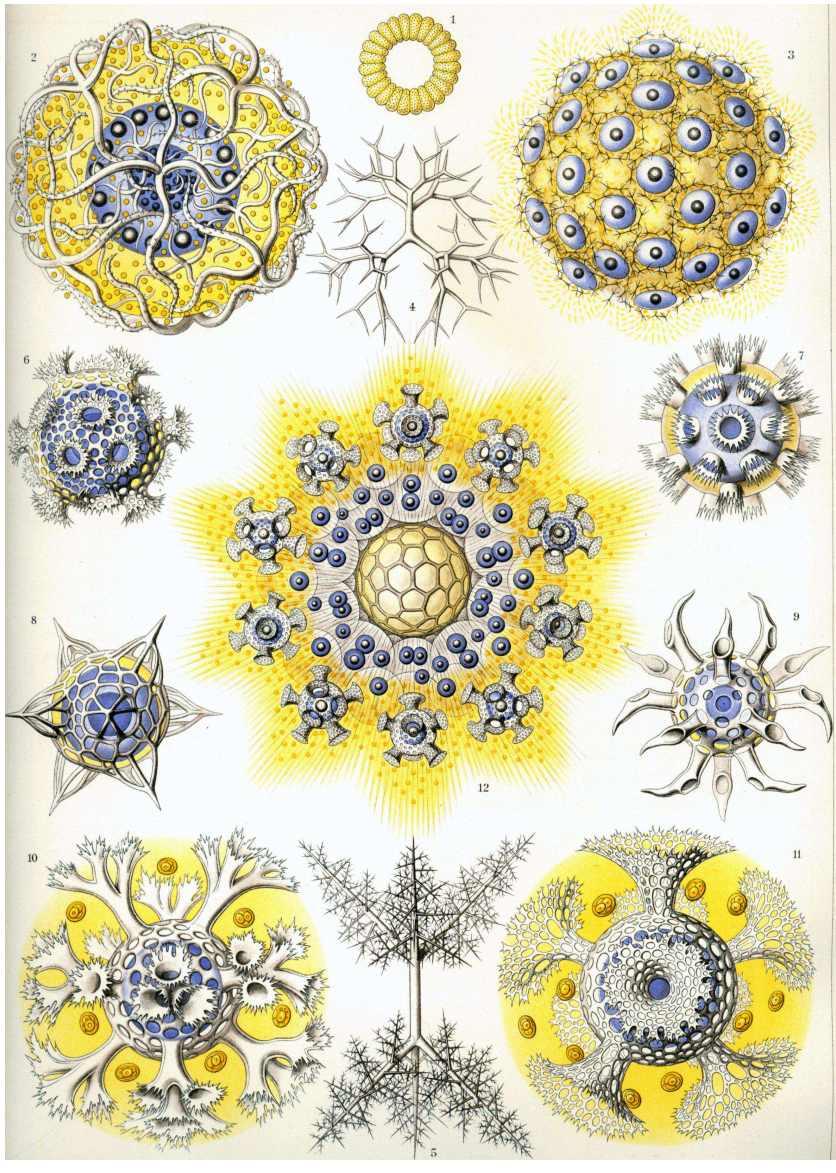

Image #51 from Ernst Haeckel's *Kunstformen der Natur* (The Art Forms of Nature). Used with permission (work is in public domain). See next page for details.

Ernst Haeckel (1834-1919) was a German biologist, naturalist, philosopher, physician, professor and artist. *Kunstformen der Natur* (The Art Forms of Nature) was released in 1904, consisting of 100 selected prints by Haeckel.

Source: http://commons.wikimedia.org/wiki/File:Haeckel_Polycyttaria.jpg. Used with permission (work is in public domain).

1 Collosphaera primordialis
2 Thalassoxanthium medusinum
3 Sphaerozoum ovidimare
4 Thalassoxantium cervicorne
5 Sphaerozoum spinosissimum
6 Cornospaera diadema
7 Trypanosphaera trepanata
8 Acrospaera inflata
9 Mazospaera lagotis
10 Caminosphaera dendrophora
11 Chronosphaera calycina
12 Solenosphaera familiaris

I nevertheless was hooked on the power that I had tasted.
It is a particular joy that any programmer will know well,
to see the machine do your bidding,
no matter how simple a task that may be.

It works, and it works because you understand how to make it work.
And it cannot do anything but work.

Michael Bromley – Confessions of an Intermediate Programmer (2014)
http://www.michaelbromley.co.uk/blog/65/confessions-of-an-intermediate-programmer

Papers I-V